Department of Physics
University of Jyväskylä
Research Report No. 8/2012

Resonance laser ionization developments for IGISOL-4

by
Mikael Reponen

Academic Dissertation
for the Degree of
Doctor of Philosophy

To be presented, by permission of the
Faculty of Mathematics and Natural Sciences
of the University of Jyväskylä,
for public examination in Auditorium FYS 1 of the
University of Jyväskylä on September 14th, 2012
at 12 o'clock noon

Jyväskylä, Finland
September 2012

Preface

The work presented in this thesis has been carried out during the years from 2007 to 2012 at the Department of Physics of the University of Jyväskylä and more precisely at the Accelerator Laboratory. In addition to the work reported in the thesis, these years have included a huge variety of experiments at IGISOL and a few memorable measurements at the University of Mainz. I am ever grateful to have had the chance to work with all the brilliant people on these during these years.

I want first especially like to thank my supervisors, Professor Juha Äystö and Dr. Iain D. Moore, firstly for giving me the opportunity to work with the IGISOL group and secondly for all the guidance and advice. Without Juha giving me a letter of recommendation for my CERN summer school application in 2006, I would probably be in some other field at the moment. My thanks also go to the other IGISOL senior persons, Prof. Ari Jokinen and Dr. Heikki Penttilä, for all the support. I wish also express my gratitude for the FURIOS members, Mr. Volker Sonnenschein, Mr. Ilkka Pohjalainen and especially again Iain for all the ideas, comments, support, encouragement and hangovers I have received over the years. I am particularly grateful to Dr. Thomas Kessler for the through introduction into Titanium:sapphire lasers and for the help along the way.

The laser ion source would be useless without the IGISOL the people who operate it, hence I would like to thank: Dr. Antti Saastamoinen, Dr. Tommi Eronen, Dr. Juho Rissanen, Dr. Viki-Veikko Elomaa, Dr. Pasi Karvonen, Dr. Veli Kolhinen, Dr. Sami Rinta-Antila, Mr. Dmitry Gorelov and Mr. Jani Hakala from the bottom of my heart. In addition to local people I would like to thank Mr. Sebastian Rothe, for the help with the lasers and experiments at IGISOL, and the rest of the LARISSA group at the University of Mainz. A special thanks goes to the Manchester collinear laser spectroscopy people, Dr. Paul Campbell, Dr. Bradley Cheal and Dr. Frances Charlwood, whom with it has been has pleasure to work.

My last two years at JYFL have been interesting as they has involved less physics and more labour. The construction of the new IGISOL-4 has been an educating experience. The bulk weight of the construction has been on the shoulders of the mechanical and electrical workshops and for that I am grateful. Especially the

mechanical workshop has been very patient with me for bringing in all sorts of odd drawings. Altogether the department of physics has been an excellent place to study and to work and I owe that to the staff here.

I want to thank my family for the support during my studies at Jyväskylä and all my friends for all the parties and good times. Finally, I deeply thank Aino Rautio for all the support and love throughout the years.

Jyväskylä, September 2012
Mikael Reponen

Author

Mikael Reponen
Department of Physics
University of Jyväskylä
Finland

Supervisors

Prof. Dr. Juha Äystö
Director
Helsinki Institute of Physics
Finland

Dr. Iain D. Moore
Department of Physics
University of Jyväskylä
Finland

Reviewers

Prof. Dr. Mark Huyse
Instituut voor Kern- en Stralingsfysica
Departement Natuurkunde en Sterrenkunde
Katholieke Universiteit Leuven
Belgium

Dr. Yuan Liu
Holifield Radioactive Ion Beam Facility
Oak Ridge National Laboratory
United States of America

Opponent

D. Sci. Michiharu Wada
Nishina Center for Accelerator-Based Science
RIKEN
Japan

Abstract

Reponen, Mikael
Resonance laser ionization developments for IGISOL 4
Jyväskylä: University of Jyväskylä, 2012, xx + 182 pp.
Department of Physics, University of Jyväskylä, Research Report 8/2012
ISBN 978-951-39-4784-2 (printed)
ISBN 978-951-39-4785-9 (electronic)
ISSN 0075-465X

The work presented in this thesis concentrates on the development of the FURIOS laser ion source towards efficient and selective production of low energy radioactive ion beams. This includes design and development of the ion guide and hot cavity catcher systems for laser ion source use, and the development of in-source and in-jet laser spectroscopy techniques. The work has been carried out at the IGISOL facility in the Accelerator laboratory of the University of Jyväskylä.

The FURIOS facility was upgraded and developed during the move to the IGISOL-4 facility. The laser transport was greatly improved in order to allow a large fraction of the initial laser intensity to be transported into the gas cell at the IGISOL-4 frontend. The careful design of the IGISOL frontend and the FURIOS facility enable the laser ion source to be utilized efficiently for the production of radioactive ion beams at IGISOL-4.

Additionally, in order to overcome the deficiencies of the standard IGISOL ion guide design under on-line conditions, an ion guide based on an original design by the LISOL group in Leuven has been adapted the IGISOL. The shadow gas cell allows efficient resonance laser ionization in a gas cell under on-line conditions. The transport efficiency of the ion guide was determined using α recoil source. Additionally, the principal operation of the ion guide was demonstrated under pseudo-on-line conditions utilizing resonance laser ionization.

An inductively heated hot cavity catcher laser ion source was developed based on existing electron bombardment heated thermal ionizer design in collaboration with the JYFL ECR group. The motivation behind the development of a new type of

recoil catcher at IGISOL is the production of rare isotope of silver, $N{=}Z$ ^{94}Ag. The evacuation time for the silver atoms from the catcher was measured to be less than 10 ms at a relatively low temperature of 1200 °C. Though the hot cavity catcher ion source principle was demonstrated, the commissioning experiment showed the need to further develop the catcher in order to improve the beam quality and ionization efficiency.

Lastly, in gas-jet spectroscopy in the form of the LIST approach was studied. Different ion guide nozzles were compared in order to find a nozzle that would produce long collimated gas jets for the use of the LIST approach. A de Laval type nozzle was found out to be the most promising, being able to produce a well collimated jet spanning a distance of 14 cm. The jet temperature was measured to be very low, which when combined with the low pressure, makes a very attractive environment for laser spectroscopy.

Acknowledgements

The thesis would not have been possible without the financial support of numerous external sources. This support has made it possible to participate in measurements abroad and to present research at international conferences and workshops. The author expresses gratitude for the support received from the rector of the University of Jyväskylä, the Department of Physics of the University of Jyväskylä, the Vilho, Yrjö and Kalle Väisälä foundation and the Waldemar Von Frenckell foundation. The Graduate School in Particle and Nuclear Physics (GRASPANP) is acknowledged for financing the access to international graduate schools and conferences. Additionally, I would like to acknowledge Mr. Toivo Matilainen for manufacturing a de Laval nozzle used in this thesis.

This work has been supported by the Academy of Finland under the Finnish Centre of Excellence Programme 2006-2011 (Project No. 231503, Nuclear and Accelerator Based Physics Programme at JYFL) and 2012-2017 (Project No. 251353, Nuclear and Accelerator Based Physics Programme at JYFL).

Contents

List of Tables

List of Figures

Acronyms

ABU Atomic Beam Unit.

ALTO Accélérateur Linéaire auprès du Tandem d'Orsay.

ANL Argonne National Laboratory.

BBO Beta Barium Borate.

CAD Computer-Aided Design.

CERN Organisation européenne pour la recherche nucléaire.

CISS Catcher-Ion-Source System.

CKM Cabibbo-Kobayashi-Maskawa Matrix.

CPT Canadian Penning Trap.

CRIS Collinear Resonant Ionization Spectroscopy.

CTBTO Comprehensive Nuclear-Test-Ban Treaty Organization.

CVL Copper Vapour Laser.

CW Continuous Wave.

DC Direct Current.

ECR Electron Cyclotron Resonance.

ECRIS Electron Cyclotron Resonance Ion Source.

EMT Electron Multiplier Tube.

FEBIAD Forced Electron Beam Induced Arc Discharge.

FHG Fourth Harmonic Generation.

FURIOS Fast Universal Resonant laser Ion Source.

FWHM Full Width Half Maximum.

GANIL Le Grand Accélérateur National d'Ions Lourds.

GISELE GANIL Ion Source using Electron Laser Excitation.

GLS Gnu Scientific library.

GPL GNU General Public License.

GSI Gesellschaft für Schwerionenforschung.

HIGISOL Heavy Ion IGISOL.

HRIBF Holifield Radioactive Ion Beam Facility.

I.P. Ionization Potential.

IGISOL Ion Guide Isotope Separator On-Line.

INS Institute for Nuclear Study.

IPN Institut de Physique Nucléaire d'Orsay.

IR Infrared.

IRIS Investigation of Radioactive Isotopes on Synchrocyclotron.

ISAC Isotope Separator and Accelerator.

ISOL Isotope Separation On-line.

ISOLDE Isotope Separator on Line.

JYFL Jyväskylän Yliopiston Fysiikan Laitos.

KDP Potassium Dihydrogen Phosphate.

LARISSA LAser Resonance Ionization Spectroscopy for Selective Applications.

LASER Light Amplification by Stimulated Emission of Radiation.

LBNL Lawrence Berkeley National Laboratory.

LBO Lithium Triborate.

LEBIT The Low Energy Beam and Ion Trap.

LeRIBS Low Energy Radioactive Ion Beam Spectroscopy Station.

LISOL Leuven Isotope Separator On-Line.

LIST Laser Ion Source Trap.

LMA Levenberg-Marquardt algorithm.

MRP Mass Resolving Power.

MSU Michigan State University.

Nd:YAG Neodymium-doped Yttrium Aluminium Garnet.

NIR Near Infrared.

NIST National Institute of Standards and Technology.

NSCL National Superconducting Cyclotron Laboratory.

PALIS PArasitic RI-beam by Laser Ionization Source.

PNPI Petersburg Nuclear Physics Institute.

RF Radio Frequency.

RFQ Radio Frequency Quadrupole.

RIKEN Rikagaku Kenkyūjo.

RILIS Resonance Ionization Laser Ion Source.

RIS Resonant Ionization Spectroscopy.

S^3 Super Separator Spectrometer.

SH Second Harmonic.

SHG Second Harmonic Generation.

SHIPTRAP Separator for Heavy Ion reaction Products.

SPES Selective Production of Exotic Species.

SPIG Sextupole Ion Guide.

SPIRAL2 "Système de Production d'Ions Radioactifs en Ligne" - generation 2.

TEM Transverse Electro-Magnetic.

THG Third Harmonic Generation.

Ti:sapphire Titanium Sapphire.

TITAN TRIUMF's Ion Trap for Atomic and Nuclear science.

TRILIS TRIUMF Resonant Ionization Laser Ion Source.

TRIUMF TRI-University Meson Facility.

TTL Transistor-Transistor Logic.

UV Ultraviolet.

VIS Visible.

1. Introduction

Nuclear physics has advanced considerably since the discovery of the nucleus by Rutherford in 1911 with most of the stable and a large number of radioactive isotopes having been discovered and studied. The current nuclear landscape, presented in Fig. 1.1, consists of over 3000 known isotopes [1], most of which are radioactive. Modern nuclear physics techniques probe the properties of exotic isotopes far away from stability, rare isomers, and the very heavy elements among which stable or nearly stable elements might still exist. Exotic nuclei are mainly produced in nuclear reactions in which a high energy beam from a particle accelerator interacts with a target. In these reactions a large number of different nuclei are produced, most of them contributing to so-called contamination. In order to detect the rarest of the nuclei, the isotopes must be separated from each other. Two main techniques exist for producing and separating radioactive isotopes, the in-flight and the Isotope Separation On-line (ISOL) method [2]. As the name implies, in-flight separators select the isotopes of interest as they are propagating through vacuum using a combination of magnets and electric fields. The ISOL technique on the other hand first stops the reaction products, re-ionizes them and uses a mass separator to produce a beam containing the isotope of interest.

One of the means of selectively enhancing the isotope of interest is via resonant laser ionization [3], whereby an atom is excited step-wise and ionized using a combination of two or more lasers. This method is highly element selective hence, when combined with a mass separator, can be used to produce pure isotopic beams free from isobaric background. The method has been used for years at the Isotope Separator on Line (ISOLDE) where the Resonance Ionization Laser Ion Source (RILIS) is used to produce radioactive beams for the majority of experiments. Today, numerous laser ion sources are operational both at off-line and on-line laboratories [4]. While these ion sources typically utilize either high repetition rate solid state Titanium Sapphire (Ti:sapphire) or medium/high repetition rate dye lasers, combinations of these exist. This thesis discusses the implementation of a Ti:sapphire -based laser ion source at the IGISOL facility.

Since the initial proposal [5,6], laser ion sources at radioactive ion beam facilities have been typically coupled with hot cavities as the hot target approach was the standard

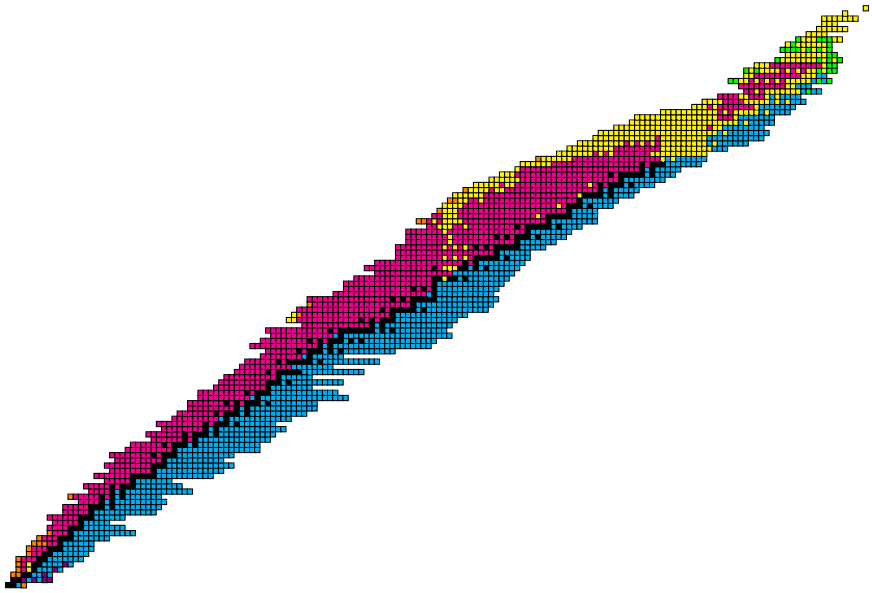

Figure 1.1. Segré chart showing the nuclear landscape containing the stable isotopes (black) and the radioactive isotopes. Colour coding as follows: β^- and β^+ radioactivity is marked in cyan and magenta, respectively, α-activity is in yellow, spontaneous fission is marked in green and proton and neutron radioactivity in orange and violet.

way of releasing reaction products from the thick target. Existing and upcoming laser facilities at ISOLDE RILIS [7–9], TRI-University Meson Facility (TRIUMF) TRIUMF Resonant Ionization Laser Ion Source (TRILIS) [10], Le Grand Accélérateur National d'Ions Lourds (GANIL) GANIL Ion Source using Electron Laser Excitation (GISELE) [4, 11], Investigation of Radioactive Isotopes on Synchrocyclotron (IRIS) RILIS [12], Holifield Radioactive Ion Beam Facility (HRIBF) RILIS [13], Accélérateur Linéaire auprès du Tandem d'Orsay (ALTO) [14] at the Institut de Physique Nucléaire d'Orsay (IPN) and Selective Production of Exotic Species (SPES) [15] couple a laser ion source with a hot cavity.

The RILIS ion source at Organisation européenne pour la recherche nucléaire (CERN) ISOLDE facility is the seminal and longest running laser ion source station among the on-line facilities [7]. The radioactive isotopes are produced in nuclear reactions driven by a 1 GeV proton beam from the CERN PS-Booster synchrotron accelerator impinging on a thick uranium-carbide target [16]. Following diffusion and transport

from the target, the laser ion source facility is used to ionize the selected isotope. RILIS was initially a high repetition rate dye -laser based facility but has been recently fitted with a complementary Ti:sapphire -based solid state laser set-up [8]. In addition, the old Copper Vapour Laser (CVL) pump lasers have been replaced with modern Neodymium-doped Yttrium Aluminium Garnet (Nd:YAG) lasers [17]. The facility is nowadays used to produce 50 % of the beams at ISOLDE and can resonantly ionize 31 elements of the periodic table [9] with ionization efficiencies ranging from 0.1-30 % [18].

Another ISOL facility that utilizes resonance laser ionization for on-line isotope production is the TRIUMF Isotope Separator and Accelerator (ISAC) facility [19]. High intensity exotic beams are produced in similar manner as at ISOLDE. A 500 MeV proton beam from the H^- cyclotron drives nuclear reactions in a thick hot target. The evaporated reaction products are ionized using various means including an Electron Cyclotron Resonance Ion Source (ECRIS) or a Forced Electron Beam Induced Arc Discharge (FEBIAD). A more selective way of ionization is to use the TRILIS laser ion source [10]. The TRILIS is a Ti:sapphire -based laser system pumped by an Nd:YAG laser operating at 10 kHz with additional harmonic generation to extend the wavelength range. Besides acting as a production source, the TRILIS facility has been used, for example, to perform resonance laser ionization on silver, actinium, radium and astatine.

GISELE at GANIL is a prototype laser ion source for the upcoming "Système de Production d'Ions Radioactifs en Ligne" - generation 2 (SPIRAL2) facility [11]. SPIRAL2 will utilize neutron-induced fission, rather than direct primary beam induced fission, in a uranium-carbide target for the production of radioactive ions. In the new facility, the target station may operate up to 4 months without a break during which time manual intervention is impossible. This calls for very reliable ion sources and therefore a low maintenance and reliable Ti:sapphire -based laser ion source is among those chosen.

The Ti:sapphire lasers described above have been developed by the LAser Resonance Ionization Spectroscopy for Selective Applications (LARISSA) group at the University of Mainz. The group has pioneered the applications of Ti:sapphire lasers used in laser ion sources and a similar system has been adopted for the FURIOS facility at IGISOL. In addition, HRIBF [20] at Oak Ridge has acquired three commercial Ti:Sapphire lasers for the RILIS which has recently been commissioned on-line and provided pure $^{83-86}$Ga beams to the Low Energy Radioactive Ion Beam Spectroscopy Station (LeRIBS) [13].

The IRIS facility at Gatchina [12] utilizes the ISOL method and a 1 GeV proton beam from the Petersburg Nuclear Physics Institute (PNPI) synchrocyclotron to produce radioactive isotopes. The laser system incorporates CVL pumped dye lasers operating at 11 kHz and offers a fundamental wavelength range of 530 nm to 850 nm which can be expanded with harmonic generation.

During the early 1990's the resonant laser ionization method was extended to gas cells and later to IGISOL based on-line facilities. Resonant ionization in a gas cell was first demonstrated [21] and further pioneered at the Leuven Isotope Separator On-Line (LISOL) facility [22] at Louvain-la-Neuve in Belgium. Besides being much less chemically selective than ISOL systems, the ion guide offers a more attractive environment for in-source laser resonance spectroscopy. The method has since been applied to the IGISOL facility at Jyväskylä in the form of the FURIOS laser ion source. Such an ionization mechanism will also play a major role in the upcoming fragmentation facilities including S^3 at GANIL and the PArasitic RI-beam by Laser Ionization Source (PALIS) facility at Rikagaku Kenkyūjo (RIKEN) [23].

This thesis is divided into six chapters. Chapters two and three introduce the basic theory of laser physics, laser ionization and the IGISOL-3 facility with the main experimental tools and facilities. The basic principles for both the high precision Penning trap mass spectrometer and the collinear laser spectroscopy station are presented. Lastly, the new IGISOL-4 facility is briefly highlighted.

Chapter four describes the FURIOS facility and the applications, namely, in-gas cell laser ionization and spectroscopy. The recent achievements on resonant laser ionization spectroscopy in a shadow gas cell are presented. During the course of the studies, the FURIOS facility was moved to the IGISOL-4 location and hence the chapter also discusses the upgrades to the FURIOS set-up as well as the general considerations that went into the construction of the new laser ion source laboratory at IGISOL-4.

The development of the Laser Ion Source Trap (LIST) method is discussed in Chapter five, particularly the shaping of gas jets. The visualisation of the jets as well as shaping using both pressure optimization and nozzle design is presented.

The final chapter presents the development of a hot cavity laser ion source for the production of $N{=}Z$ ^{94}Ag. The motivation of using a hot cavity catcher rather than an ion guide for this particular nucleus is presented along with the culmination of the development process, an inductively-heated hot cavity catcher laser ion source. This new type of catcher is presented in detail with results from a recent commissioning experiment.

The thesis covers the applications of resonant laser ionization at IGISOL using hot cavity and gas cells. The work is based on the following enclosed articles, three of which have been published and one which is in preparation:

I: M. Reponen, I.D. Moore, T. Kessler, I. Pohjalainen, S. Rothe and V. Sonnenschein
Laser developments and resonance ionization spectroscopy at IGISOL
Eur. Phys. J. A (2012) 48: 45

II: M. Reponen, I.D. Moore, I. Pohjalainen, T. Kessler, P. Karvonen, J. Kurpeta, B. Marsh, S. Piszczek, V. Sonnenschein, J.Äystö
Gas jet studies towards an optimization of the IGISOL LIST method
Nucl. Instr. in Phys. Res. A 635 1 (2011) 24-24

III: M. Reponen, T. Kessler, I.D. Moore, S. Rothe and J. Äystö
A Hot Cavity Laser Ion Source at IGISOL
Eur. Phys. J. A 42 3 (2009) 509-515

IV: M. Reponen, I. D. Moore, I. Pohjalainen, S. Rothe, M. Savonen, V. Sonnenschein, and J. Äystö
Inductively heated hot cavity catcher, Rev. Sci. Instr, In preparation (2012)

The author has been heavily involved in the articles **I-IV** and has contributed to the writing process as well as to the experimental work. The author's contribution to Article **I** was the experimental measurements and data analysis on the power broadening of silver, the determination of the isotope shift in nickel using in source spectroscopy, in-jet spectroscopy of nickel and LIST development.

In Article **II** the author designed the measurement set-up and the ion guide nozzles, including the de Laval nozzle. The author was also the primary photographer of the jets and performed the Pitot probing of the supersonic jet and the subsequent data-analysis.

The authors' contribution to the Article **III** was the characterization of the hot cavity catcher and the development of the resonance ionization scheme for silver. The author also participated in testing the hot cavity catcher laser ion source at IGISOL-3 and in the following data analysis. The author made the mechanical designs for the inductively heated hot cavity catcher in Article **IV** as well as the initial performance tests. The author was also the principal contributor in the proof of principle experiment, in the following data analysis and in the ion-optical simulations of the catcher.

2. Theory

2.1. Laser

Light Amplification by Stimulated Emission of Radiation, commonly known as a laser, is a versatile tool for research due to a number of attractive characteristics. A laser beam can be described as having properties such as monochromaticity, coherence, directionality and brightness, each of which sets it apart from conventional light sources. In addition to numerous technical applications, lasers have been used to study subjects ranging from material properties or shapes of atomic nuclei to gravity waves predicted by general relativity.

2.1.1. Fundamental physics of lasers

A laser is a device in which, under suitable suitable conditions, a light wave is amplified as it passes through active material. If the light is confined in a resonator and the active material is pumped to a suitable excited state, the light starts to oscillate and stimulates transitions, being amplified during each pass through the active material. Lasing does not occur without very special set-ups and though the ground work for the quantum theory of radiation was laid out by Einstein in 1917 [24], a working laser was only realized in 1960 in the form of a ruby laser by Maiman [25].

Lasing has since been demonstrated in metallic vapour [26], for example in copper vapour, in liquids using certain types of dye [27], and in solid state lasers using either dielectric or semiconductor materials [28]. Furthermore, lasing has also been achieved in chemical lasers [29] where chemical reactions provide the photons for lasing and in free electron lasers by stimulated emission of bremsstrahlung of relativistic electrons travelling in a periodic magnetic field [30]. The following theory considers the dielectric solid state lasers such as titanium sapphire ($Ti:Al_2O_3$) or Nd:YAG, from the point of view of resonant laser ionization and it is based on references [26], [31] and [32].

Absorption, emission and stimulated emission

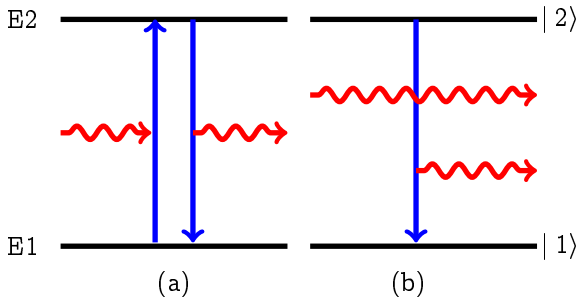

Figure 2.1. Absorption and spontaneous emission (a), and stimulated emission (b). The energy difference between the levels and the energy of the absorbed or emitted photon is $E_1 - E_2 = h\nu$.

Lasers and the basic concepts of light-atom interaction are based on absorption, spontaneous and stimulated emission, presented in figure 2.1. These are so-called radiative transitions whereby the transition is induced by an electromagnetic wave. The transitions can also take place in non-radiative fashion for example by molecular collisions. In absorption, a photon with an energy $h\nu$ transfers an atomic electron from state $\mid 1\rangle$ to state $\mid 2\rangle$ with finite probability if the energy difference between the levels matches the photon energy. Each excited state has a finite lifetime after which the state decays by emitting a photon in a random direction, again with energy $h\nu$.

If an atom is in state $\mid 2\rangle$, an incident photon with energy $h\nu$ can induce a transition $\mid 2\rangle \rightarrow \mid 1\rangle$. In this process, called stimulated emission, the incident and emitted photon travel in the same direction with the same phase and energy.

The probability of a transition can be expressed using Einstein's coefficients. These are derived for induced absorption, induced emission and spontaneous emission [32] using Einstein's thermodynamic treatment. The probability per second, P_{spe}, that a photon is spontaneously emitted from state $\mid 2\rangle$ is:

$$\frac{dP_{spe}}{dt} = A_{21}, \tag{2.1}$$

where A_{21} is Einstein's coefficient of spontaneous emission. It depends only on the transition properties, not on the external field. On the other hand, the stimulated emission probability per second, P_{ste}, is linked to the spectral energy density $\rho(\nu)$

of an external field:

$$\frac{dP_{ste}}{dt} = B_{21}\rho(\nu), \tag{2.2}$$

where B_{21} is Einstein's coefficient for stimulated emission. Similarly, the absorption probability per second, P_{abs}, is described by

$$\frac{dP_{abs}}{dt} = B_{12}\rho(\nu). \tag{2.3}$$

Here B_{12} is Einstein's coefficient for absorption. The coefficients are linked via the Boltzmann distribution:

$$N_i = N\frac{g_i}{Z}e^{-E_i/kT} \tag{2.4}$$

and Planck's law of radiation

$$\rho(\nu)d\nu = \frac{8\pi\nu^2}{c^3}\frac{h\nu}{e^{h\nu/kT}-1}d\nu, \tag{2.5}$$

where ν is the radiation frequency, N is the total number of atoms or molecules, $g_i = 2J_i + 1$ is the number of degenerate sublevels, E_i is the energy of the ith level, Z is the partition function (not to be confused with the proton number), T is the temperature and k is the Boltzmann constant. Using the Boltzmann distribution (Eq. 2.4) to solve the population density ratio between states $\mid 1\rangle$ and $\mid 2\rangle$ gives

$$\frac{N_2}{N_1} = \frac{g_2}{g_1}e^{-h\nu/kT}, \tag{2.6}$$

where $h\nu = E_2 - E_1$.

A simple laser

If two states $\mid 1\rangle$ and $\mid 2\rangle$ have the same statistical weights g_1 and g_2, the induced emission and absorption have the same probability hence effectively making a two level laser impossible. For the successful operation of a laser a population inversion must exist between states $\mid 1\rangle$ and $\mid 2\rangle$. Therefore $N_2 > g_2N_1/g_1$ and thus the active medium should no longer act as an absorber but allow stimulated emission to dominate over spontaneous emission (see Eq. 2.6), acting as an amplifier. In a suitable resonator configuration this leads to an increase in the photon flux F, such

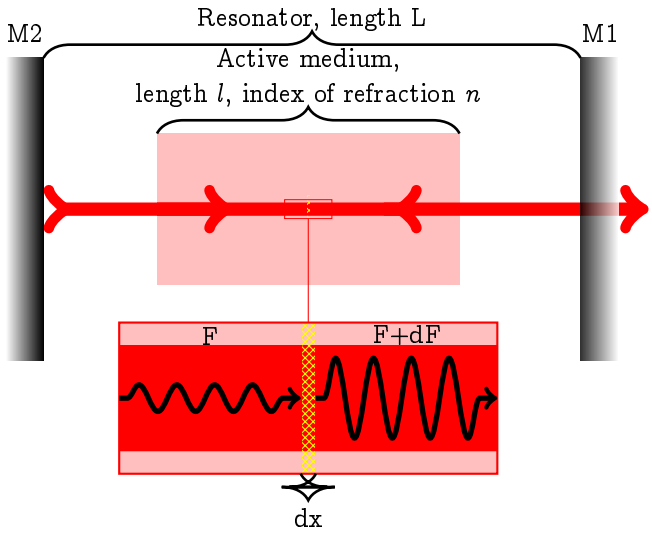

Figure 2.2. The basic idea of a laser. Mirrors M1 and M2 form a resonator and the photon flux F is amplified by an amount dF during distance dx in the active material. The mirror M2 is ~100% reflective while M1 is partially reflective to allow a fraction of the laser light to exit the resonator.

that $dF/dx > 0$ where dx is an infinitesimal distance travelled by the light beam in the active medium (see Fig. 2.2).

In order to calculate the flux change within a resonator the transition rates (Eqs. 2.1 - 2.3) need to be written as transition probabilities [31]:

$$\left.\frac{dN_2}{dt}\right|_{spe} = -AN_2, \tag{2.7a}$$

$$\left.\frac{dN_2}{dt}\right|_{ste} = -\sigma_{21}FN_2, \tag{2.7b}$$

$$\left.\frac{dN_1}{dt}\right|_{abs} = -\sigma_{12}FN_1, \tag{2.7c}$$

where σ_i is the cross section for either the stimulated emission (ste) or for the absorption (abs). When a photon flux F travels through the active medium it changes by an amount dF, depending on the difference between the rates of absorption and emission, during a distance dx . For a beam with area S the change in the photon number after distance dx is SdF. On the other hand as both stimulated emission and absorption take place within a volume Sdx and the difference between these processes must correspond to SdF, the flux change can be written in the form

$$SdF = (\sigma_{21}N_2 - \sigma_{12}N_1)\, Sdx. \tag{2.8}$$

Assuming the levels $\mid 1\rangle$ and $\mid 2\rangle$ to be g_1- and g_2 -fold degenerate, respectively, the absorption and stimulated emission rates are related by

$$g_2\sigma_{21} = g_1\sigma_{12}, \tag{2.9}$$

which allows the flux change to be written as

$$\frac{dF}{dx} = \sigma_{21}F \underbrace{\left\{N_2 - \frac{g_2N_1}{g_1}\right\}}_{\text{Population Inversion}}. \tag{2.10}$$

For a simple two mirror laser resonator presented in Fig. 2.2 the laser beam intensity $I' \propto F'$ after one round trip in the cavity can be written with the help of Eq. 2.10 [31] as

$$\begin{aligned} I' = I \underbrace{\left(e^{\sigma\left(N_2 - \frac{g_2N_1}{g_1}\right)l}\right)}_{Gain} \underbrace{(1-L_i)}_{Loss} \underbrace{(1-a_1-T_1)}_{Mirror1} \times \\ \underbrace{\left(e^{\sigma\left(N_2 - \frac{g_2N_1}{g_1}\right)l}\right)}_{Gain} \underbrace{(1-L_i)}_{Loss} \underbrace{(1-a_2-T_2)}_{Mirror2}, \end{aligned} \tag{2.11}$$

where $e^{\sigma\left(N_2 - \frac{g_2N_1}{g_1}\right)l}$ is the flux gained in the active medium of length l, L_i is the internal loss per pass in the resonator, T_i is the transmission of a mirror and a_i is a loss occurring in a mirror. At the threshold of laser operation the intensity I' is equal to the initial intensity I hence

$$(1-a_1-T_1)(1-a_2-T_2)(1-L_i)^2 e^{2\sigma\left(N_2 - \frac{g_2N_1}{g_1}\right)l} = 1. \tag{2.12}$$

By defining a threshold population inversion as $N_c = \left\{ N_2 - \frac{g_2 N_1}{g_1} \right\}$ and solving Eq. 2.12 for N_c gives

$$N_c = -\frac{\ln((1-a_1-T_1)(1-a_2-T_2)) + 2\ln(1-L_i)}{2\sigma l}. \tag{2.13}$$

By assuming small mirror losses $a_1 = a_2 = a$ and $(1-a-T_i) \cong (1-a)(1-T_i)$, and by further defining the logarithmic internal loss of the cavity as γ_i, the logarithmic mirror losses γ_1 and γ_2 and the single pass-loss of the resonator cavity as γ:

$$\gamma_1 = -\ln(1-T_1) \tag{2.14}$$

$$\gamma_2 = -\ln(1-T_2) \tag{2.15}$$

$$\gamma_i = -(\ln(1-a) + \ln(1-L_i)) \tag{2.16}$$

$$\gamma = \gamma_i + \frac{\gamma_1 + \gamma_2}{2}, \tag{2.17}$$

Eq: 2.13 can be expressed as

$$N_c = \frac{\gamma}{\sigma l}. \tag{2.18}$$

This equation states that the critical population inversion, hence the threshold for the laser operation, is directly proportional to the cavity losses γ and inversely proportional to the length of the active medium l and the absorption coefficient σ. For example, from Eq. 2.18 it is clear that the longer the active medium, the lower the critical population inversion and thus pump rate required to initiate laser action.

2.1.2. Laser pumping

As stated earlier, a two level laser cannot be made to work due to stimulated emission and absorption compensating each other. Hence a laser requires an excitation scheme involving more than two levels so that a population inversion can happen between two states in the scheme. For example, a Ruby laser is a three-level laser with a narrow emission band [33], an Nd:YAG [34] laser is a four level narrow band laser whereas a Ti:sapphire [35] laser is a broadband four level laser.

The transitions in both the three and four level scheme follow the same principle, namely excitation to a high-lying state $\mid 1_{pump}\rangle$ that decays fast to a long-living

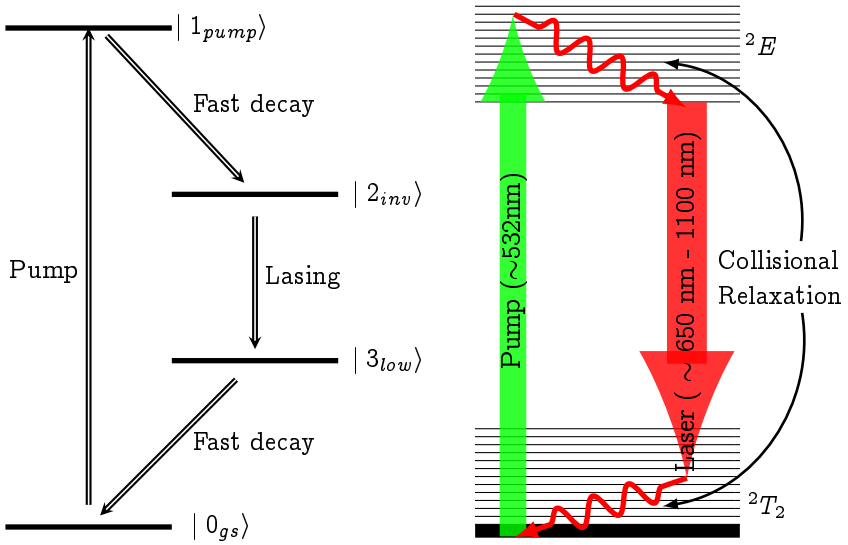

(a) Schematic energy level structure of a four level laser

(b) Ti:sapphire energy level structure

Figure 2.3. (a.) A basic four level laser energy scheme and (b.) a representation of titanium sapphire energy levels relevant for lasing [33]. The pump laser excites electrons from the lowest level in the $^2T_2$ state to the vibrational levels ^2E which quickly decay by collisions to the lowest vibrational level in that state. Lasing takes place between this level and some of the levels in the $^2T_2$ state which further decay quickly to the ground level.

state $|\,2_{inv}\rangle$. This allows the population inversion to build up between the $|\,2_{inv}\rangle$ state and a state $|\,3_{low}\rangle$ to which it decays 2.3. In three level lasers this state is the ground state while in a four level laser it is a short-lived state or collection of states that decay quickly to the ground state.

The pump transition can be made in many ways depending on the energy and absorption band of the active material. The pumping processes can be categorized into four classes; optical pumping, electrical pumping, chemical pumping and gas dynamics pumping. Optical pumping and, more precisely, laser pumping is discussed in the following as it is the most relevant process for this thesis.

The Nd:YAG laser is one of the most common lasers used in industry and research. It is an optically (flashlight or diode) pumped laser used in high power Continuous

Wave (CW) or in high energy pulsed laser applications. In research the Nd:YAG laser is widely used for pumping tunable lasers.

Threshold pump power is an important property on an laser resonator. It tells how much energy needs to be put into the laser resonator in order to initiate the laser action. Lasers with higher efficiency typically have a lower threshold pump power. Assuming a Gaussian pump beam distribution, the threshold diode pump power for longitudinally pumped laser can be written as

$$P_{th} = \frac{\gamma}{\eta_p} \frac{h\nu_p}{\tau} \frac{\pi \left(\omega_0^2 + \omega_p^2\right)}{2\sigma_e}, \tag{2.19}$$

where η_p is the total pump efficiency, τ is the average lifetime of the upper laser level ν_p is the pump laser frequency, ω_p is the pump spot diameter, ω_0 is the beam waist of the TEM_{00} lasing mode and σ_e is the effective stimulated emission cross-section. Similarly, threshold diode power for a transversely pumped laser becomes:

$$P_{th} = \frac{\gamma}{\eta_p} \frac{h\nu_p}{\tau} \frac{\pi r^2}{\sigma_e \left(1 - e^{1-\left(2r^2/\omega_0^2\right)}\right)}, \tag{2.20}$$

where r is the laser rod radius.

As an example, Eq. 2.20 can be applied to the Nd:YAG laser used at FURIOS as a pump laser. The laser (Lee Laser LDP-200MQG) is pumped transversally with laser diodes and it can be operated either in CW or pulsed mode. The laser resonator, in CW mode, consists only of the Nd:YAG crystal between two planar mirrors.

While most of the laser parameters needed to calculate the threshold pump power are available, the logarithmic internal loss L_i used in Eq. 2.16 remains unknown. In order to extract this value the output power from the laser should be measured with several output couplers with different transmission factors as in the method of Findlay and Clay [36]. Therefore, an internal loss of L_i =5 % was used to calculate γ based on Ref. [31].

First, the single pass loss of the resonator cavity γ is calculated using Eq. 2.17. The output coupler of the Lee laser has a reflectivity of 80 %, hence $\gamma_1 = -\ln(0.8)$. Assuming the high reflector to have a reflectivity of 100 %, γ_2 becomes $\sim$0. By further neglecting the mirror absorption losses a and using the 5 % value for internal losses L_i, the single pass loss becomes

$$\gamma = -\ln(0.95) - \frac{\ln(0.8)}{2} \approx 0.163. \tag{2.21}$$

Using the typical diode pump efficiency, $\eta_p = 30$ % [33], a diode wavelength of 808 nm, an Nd:YAG upper level lifetime $\tau = 230$ μs, emission coefficient $\sigma_e = 2.8 \cdot 10^{-19}$ cm^2 [31] and a Nd:YAG rod radius of 2 mm, the pump power threshold can be calculated. By further assuming that the the pump spot beam waist ω_0 is considerably smaller than the Nd:YAG crystal radius r, the $\left(1 - e^{1-\left(2r^2/\omega_0^2\right)}\right)$ term in Eq. 2.20 becomes 1, yielding

$$P_{th} \approx \frac{0.163}{0.3} \frac{6.626 \cdot 10^{-34} \text{ Js} \frac{3 \cdot 10^8 \text{ m/s}}{808 \text{ nm}}}{230 \ \mu\text{s}} \frac{\pi \cdot (2 \text{ mm})^2}{2.8 \cdot 10^{-19} \text{ cm}^2} = 260 \text{ W}. \tag{2.22}$$

The calculated value for the diode electrical power of about 260 W, is close to the experimental value of 220 W extrapolated using factory data for CW operation. However, this should be treated with caution as it was extracted by multiplying the given diode current values with an extrapolated diode array voltage.

2.1.3. Laser characteristics

In order to investigate more specific lasing behaviour this section discusses a four level CW laser using rate equations, followed by a brief look at a pulsed laser. The system covered here is highly idealised with approximations that allow a very general demonstration of laser behaviour. It is assumed that the population in the lower laser state $\mid 3_{low}\rangle$ and the pump state $\mid 1_{pump}\rangle$ is negligible (see Fig. 2.3a). Furthermore, the laser is assumed to be oscillating in a single mode with uniform pump and mode energy distributions without dependence on the location in the active medium. These approximations allow the derivation of so-called space-independent rate equations for a four-level laser [31]. For a more accurate analysis of lasers, pass-by-pass methods such as that of Rigrod [37] should be used.

The differential equation describing the population N_2 in the upper laser state $\mid 2_{inv}\rangle$ can be expressed as

$$\frac{\mathrm{d}N_2}{\mathrm{d}t} = R_p - B\phi N_2 - \frac{N_2}{\tau_{N_2}}, \tag{2.23}$$

where R_p is the pump rate, $B\phi N_2$ accounts for the stimulated emission and $\frac{N_2}{\tau_{N_2}}$ for the spontaneous emission. Here, the term for stimulated emission, $B\phi N_2$, is written using Einstein's coefficient rather than with the photon flux as in Eq. 2.7. As the population in the upper laser level changes, so does the number of photons in the laser cavity. Whereas the population in the upper laser state is decreased by the spontaneous and stimulated emission, the number of photons ϕ in the cavity is

increased by the stimulated emission $B\phi N_2$ multiplied by the volume of the mode V_a in the active medium, and is decreased by the photon lifetime τ_c in the cavity:

$$\frac{d\phi}{dt} = V_a B\phi N_2 - \frac{\phi}{\tau_c}. \tag{2.24}$$

The interesting term in these two rate equations is the coefficient for stimulated emission B. It can be derived by starting from a simple resonator with length L, active medium length l and refractive index n as seen in Fig. 2.2. Using Eq. 2.11, applying the approximations used forource Eq. 2.17, assuming equal statistical weights $g_1 = g_2$ and assuming N_1 to be negligible, and substituting for the expressions given in Eqs. 2.17, the change in intensity $\Delta I = I' - I$ can be calculated:

$$\begin{aligned}\Delta I &= \left(\left(1-T_1\right)\left(1-T_2\right)\left(1-a\right)^2\left(1-L_i\right)^2 e^{2\sigma N_2 l} - 1\right) I \\ &= \left(e^{2(\sigma N_2 l - \gamma)} - 1\right) I,\end{aligned} \tag{2.25}$$

which can be further simplified, by assuming $\sigma N_2 l - \gamma << 1$, and expanding the exponential to first order to give

$$\Delta I = 2\left(\sigma N_2 l - \gamma\right) I. \tag{2.26}$$

The absolute amount by which the intensity changes per round trip is less important than the rate of this change. Taking the optical length (L_e) of the resonator (see Fig. 2.2) $L_e = L + (n-1)l$, the duration of one round trip becomes

$$\Delta t = \frac{2L_e}{c}. \tag{2.27}$$

As a round trip typically takes some nanoseconds and assuming that ΔI is small, the ratio $\frac{\Delta I}{\Delta t}$ can be approximated as $\frac{dI}{dt}$ [31].Dividing Eq. 2.26 by Δt gives

$$\frac{\Delta I}{\Delta t} = \frac{\mathrm{d}I}{\mathrm{d}t} = \left(\frac{\sigma l c N_2}{L_e} - \frac{\gamma c}{L_e}\right) I, \tag{2.28}$$

which, after comparing with Eq. 2.24, yields

$$B = \frac{\sigma l c}{V_a L_e} \tag{2.29}$$

$$\text{and } \tau_c = \frac{L_e}{\gamma c}, \tag{2.30}$$

because $\phi \propto I$. Eqs. 2.23 and 2.24 now give the space-independent rate equations that describe the dynamic behaviour of a four level CW laser. The equations can also be used to calculate an important laser parameter, the output power from the laser through mirror M1 (Fig. 2.2). The $\frac{1}{\tau_c}$ term in Eq. 2.24 describes the rate at which photons exit the cavity. By inserting γ from Eq. 2.17 into Eq. 2.30, the loss mechanisms can be separated as

$$\frac{1}{\tau_c} = \frac{\gamma_i c}{L_e} + \frac{\gamma_1 c}{2L_e} + \frac{\gamma_2 c}{2L_e}. \tag{2.31}$$

Inserting this back into Eq. 2.24 gives

$$\frac{\mathrm{d}\phi}{\mathrm{d}t} = V_a B \phi N_2 - \phi\left(\frac{\gamma_i c}{L_e} + \frac{\gamma_1 c}{2L_e} + \frac{\gamma_2 c}{2L_e}\right), \tag{2.32}$$

where the term $\frac{\gamma_1 c}{2L_e}\phi$ describes the rate at which the photons exit the resonator through mirror M1. Multiplying this by the photon energy $h\nu$ gives the output power:

$$P_{cw_O} = \frac{\gamma_1 c}{2L_e} h\nu \phi. \tag{2.33}$$

Using the values given in the end of the previous section for the FURIOS Nd:YAG pump laser, Eq. 2.33 can be used to calculate the number of photons in the cavity for a given output power when the laser is operating at 1064 nm. First, the optical length for the resonator is calculated using the total mechanical length L=0.64 m, the Nd:YAG crystal length, l=0.118m and the Nd:YAG index of refraction n=1.833, giving

$$L_e = 0.64 \text{ m} + (1.833 - 1)0.118 \text{ m} = 0.74 \text{ m}. \tag{2.34}$$

Now solving Eq. 2.33 for ϕ using an 80 % output coupler and an output power of 200 W (CW), the number of photons in the cavity becomes:

$$\phi = \frac{2P_{cw_O}L_e}{\gamma_1 h\nu c} = \frac{2 \cdot 200 \text{ W} \cdot 0.74 \text{ m}}{-\ln(0.8) \cdot (3 \cdot 10^8 \text{ m/s})^2 \cdot 6.626 \cdot 10^{-34} \text{ Js}/1064 \text{ nm}} \tag{2.35}$$

$$= 2.4 \cdot 10^{13} \text{ photons.} \tag{2.36}$$

Though the number of photons in a cavity of a CW laser is large, it is still orders of magnitude less than the number of photons in a pulsed laser resonator.

2.1.4. Q-switching

CW operation is preferable in applications where a steady laser power and narrow linewidth are required. Other applications, such as resonant laser ionization, require large photon densities unavailable from typical CW lasers. Increasing the power of a CW laser to match the needed photon density would require increasing the pump power eventually leading to an excessive heat load. The reason why CW lasers cannot reach high photon densities is that for any given pump power the population inversion eventually reaches steady state I_{sat} [26]. The time t_s to reach the steady state is equivalent to one cavity round trip (Eq. 2.27) multiplied by m round trips in the resonator needed to achieve I_{sat}. For example, in Ti:sapphire lasers or in an Nd:YAG laser, the lifetime of the upper laser state is 3.2 μs and 230 μs, respectively [26]. This is much longer than the typical $t_s < 1\mu$s, hence the steady state is achieved well before the upper laser population is saturated.

Q-switching is a technique whereby the quality factor (Q-factor) of the resonator is varied so that the population in the upper laser level is first allowed to increase and then to deplete abruptly. The switching is achieved by placing optical elements into the laser resonator which prevent the beam propagation in a controllable manner. Q-switches can be passive saturable absorbers, typically a dye solution with low saturation intensity, or active switches operated either mechanically, acousto-optically or electrically. The main focus in this section is in electro-optical shutters such as Pockels cells and acousto-optic Q-switches that are used in high repetition rate lasers.

The Pockels cells are based on the Pockels effect in which the refractive indices in a suitable crystal, such as Beta Barium Borate (BBO), are changed by applying a high voltage [31]. The applied voltage induces birefringence in the crystal which in turn separates the polarization of the incoming wave into x and y components with a phase difference $\Delta\varphi = k\Delta nL'$. Here, $k = \frac{2\pi}{\lambda}$, Δn is the value of birefringence and L' is the length of the crystal. With the use of polarization filters or a suitable resonator

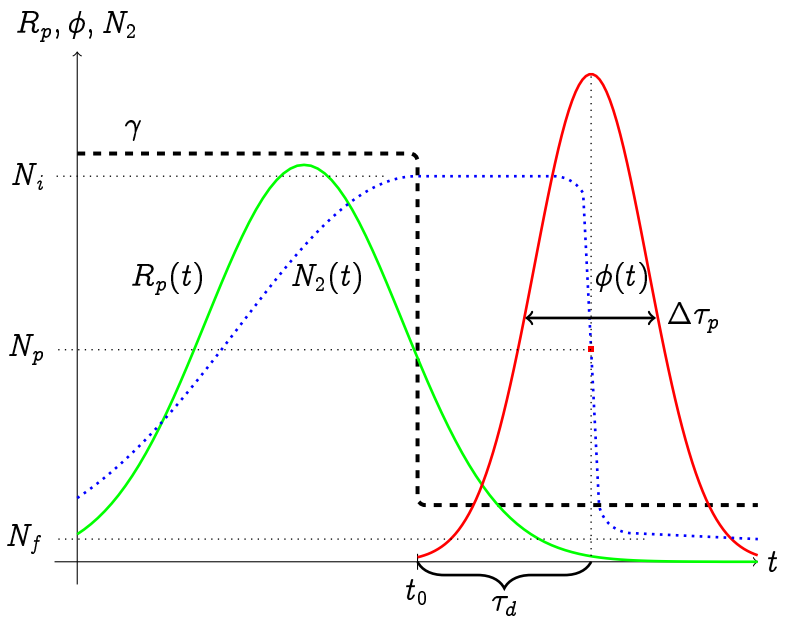

Figure 2.4. Time evolution of the cavity Q-factor (cavity loss γ), pump rate ($R_p(t)$), upper laser state population $N_2(t)$ and photon number in cavity the ($\phi(t)$) of a pulsed laser pumped Q-switched laser [32, 38]. The general behaviour applies also to CW pumped lasers. τ_d is the time delay between Q-switching (t_0) and the photon pulse, $\Delta\tau_p$ is the output pulse width and $N_{i,p,f}$ are the initial, photon peak, and final upper laser level population. Here the Q-switched laser pulse is of Gaussian shape, however in practice the pulse shape is not symmetrical.

configuration only a wave with a specific polarization is allowed to propagate in the resonator. With a suitable voltage, the wave polarization is rotated 90° after two passes through the Pockels cell hence effectively blocking it from propagating around the resonator.

The acousto-optic Q-switches are typically used in Nd:YAG lasers. They operate by inducing losses in the cavity by deflecting the incident beam off from the resonator [33]. The deflection occurs due to the photo elastic effect inducing an effective "grating" in crystals such as quartz.

The qualitative time evolution of the pump rate, upper laser level population and

cavity photon number is presented in Fig. 2.4. From the figure it can be seen that the pump pulse R_p comes in at time $t > 0$ and the population N_2 in the upper laser level begins to rise as a result. N_2 reaches its maximum value at t_0 at which time the Q-switch is turned off hence decreasing the cavity losses dramatically. This leads to an increase in the photons in the resonator and to an eventual photon peak at τ_d after which the population N_2 begins to decrease rapidly. The photon peak width $\Delta\tau_p$ is typically some tens of nanoseconds. As the population N_2 persists for a considerable time after the pump pulse R_p the Q-switching can be used to control the delay between the pump pulse and the laser output, a technique utilized for synchronizing multiple Ti:sapphire lasers pumped by a single pulsed Nd:YAG laser.

The theory for fast active Q-switching for a four level laser pumped with a pulsed laser, begins from the rate equations 2.23 and 2.24 [31]. When $t < t_0$, the cavity losses γ are high and the laser operates below the threshold meaning that no oscillation occurs but the N_2 population inversion increases. If the Q-switching is applied when N_2 has saturated to the maximum value N_i at which point ϕ=0, $\frac{dN_2}{dt} = 0$ and Eq. 2.23 can be written as

$$N_i = \tau_{N2} R_p(t_0), \tag{2.37}$$

where $R_p(t_0)$ is the pump rate at the Q-switch point. Assuming that

$$R_p(t_0) \propto \int R_p dt \propto E_p,$$

the population inversion and pump energy at the lasing threshold becomes: $N_{ith} = N_c = \frac{\gamma}{\sigma l}$ and E_{ith} which can be compared to the values at the Q-switch point as follows:

$$\frac{N_i}{N_{ith}} = \frac{E_p}{E_{ith}}. \tag{2.38}$$

The value $X_{th} = \frac{E_p}{E_{ith}}$ states how much the threshold is exceeded at the time of Q-switching. An assumption that X_{th} and N_{ith} are known allows the calculation of the time evolution of the laser properties from $t > t_0$ onwards. Starting from initial conditions $N(t_o) = N_i$ and $\phi(t_0) = \phi_i \sim$1, and assuming that the population inversion changes so fast that the pump rate R_p and spontaneous emission $\frac{N_2}{\tau_{N2}}$ do not contribute in significant amounts, Eqs. 2.23 and 2.24 can be written as

$$\frac{dN_2}{dt} = -B\phi N_2 \tag{2.39}$$

$$\frac{d\phi}{dt} = V_a B\phi N_2 - \frac{\phi}{\tau_c}. \tag{2.40}$$

The photon number in the resonator peaks when $\frac{d\phi}{dt} = 0$ with a corresponding population inversion N_p,

$$\begin{aligned} 0 &= V_a B N_p - \frac{1}{\tau_c} \\ \Rightarrow N_p &= \frac{1}{V_a B \tau_c} = \frac{\gamma}{\sigma l} = N_c, \end{aligned} \tag{2.41}$$

when using Eq.'s 2.29 and 2.30. Inserting Eq. 2.41 into Eq. 2.38 gives the ratio between the initial population inversion and the population inversion at the photon peak

$$\frac{N_i}{N_p} = X_{th}. \tag{2.42}$$

The peak output power P_p, the output pulse width $\Delta\tau_p$ and the pulse delay τ_d can now be calculated starting from Eq. 2.33 and using the photon count peak value ϕ_p to give

$$P_p = \frac{\gamma_1 c}{2L_e} h\nu\phi_p. \tag{2.43}$$

The number of photons in the peak depends on the time evolution of the population inversion $\frac{\mathrm{d}N_2}{\mathrm{d}t}$. Taking a ratio of the rate equations and Eq. 2.40 gives

$$\begin{aligned} \frac{\mathrm{d}\phi}{\mathrm{d}t} \Big/ \frac{\mathrm{d}N_2}{\mathrm{d}t} = \frac{\mathrm{d}\phi}{\mathrm{d}N_2} &= \frac{V_a B N_2 \phi - \phi/\tau_c}{-B N_2 \phi} \\ &= -V_a + \frac{V_a}{V_a B \tau_c N_2} = -V_a \left\{ 1 - \frac{N_p}{N_2} \right\}, \end{aligned} \tag{2.44}$$

with the help of Eq. 2.41. Integrating

$$\int_{\phi_i}^{\phi_p} \mathrm{d}\phi = \int_{N_i}^{N_p} -V_a \left\{ 1 - \frac{N_p}{N_2} \right\} \mathrm{d}N_2$$
$$\Rightarrow \phi_p - \phi_i = -V_a N_p \left(\frac{N_i}{N_p} - \ln\left(\frac{N_i}{N_p} \right) - 1 \right), \tag{2.45}$$

and inserting the resulting ϕ_p into Eq. 2.43 with the assumption $\phi_i \ll \phi_p$ gives, with the help of Eq. 2.41, the output power as

$$\begin{aligned} P_p &= -\frac{\gamma_1 c}{2L_e} h\nu V_a N_p \left(\frac{N_i}{N_p} - \ln\left(\frac{N_i}{N_p} \right) - 1 \right) \\ &= V_a \frac{\gamma_1 c}{2L_e} \frac{\gamma h\nu}{\sigma l} \left(\frac{N_i}{N_p} - \ln\left(\frac{N_i}{N_p} \right) - 1 \right) \\ &= \frac{\gamma_1}{2} \frac{A_b}{\sigma} \frac{h\nu}{\tau_c} \left(\frac{N_i}{N_p} - \ln\left(\frac{N_i}{N_p} \right) - 1 \right) \end{aligned} \tag{2.46}$$

where $A_b = \frac{V_a}{l}$ is the laser rod cross-section. Though the high repetition rate laser output can be characterized by the average output power, the pulse energy is more important for applications as it reveals how efficiently the laser can be used to drive atomic transitions.

The total number of photons present during the pulse is needed to calculate the pulse energy. Integrating the photon rate equation of Eq. 2.40 over time with limits $\phi(T_0) = \phi(\infty) \cong 0$ gives

$$\int_{\phi(0)}^{\phi(\infty)} d\phi \cong 0 = \int_0^\infty \left(V_a B N_2 - \frac{1}{\tau_c} \right) \phi dt$$
$$\Rightarrow \int_0^\infty \phi dt = V_a \tau_c \int_0^\infty B\phi N_2 dt. \tag{2.47}$$

The $\int_0^\infty B\phi N_2 dt$ -term can be readily acquired from the population inversion rate (Eq. 2.40) by integrating

$$\int_{N_i}^{N_f} \mathrm{d}N = N_f - N_i = -\int_0^{\infty} BN_2\phi \mathrm{d}t$$
$$\rightarrow \int_0^{\infty} B\phi N_2 dt = N_i - N_f, \tag{2.48}$$

which, by inserting into Eq. 2.47, gives

$$\int_0^{\infty} \phi \mathrm{d}t = V_a \tau_c (N_i - N_f). \tag{2.49}$$

Finally, the peak energy E is calculated as the time integral of the peak power [31] (Eq. 2.43)

$$\begin{aligned} E = \int_0^{\infty} P(t)\mathrm{d}t &= \frac{\gamma_1 c}{2L_e} h\nu \int_0^{\infty} \phi \mathrm{d}t = \\ &= \frac{\gamma_1 c}{2L_e} h\nu V_a \tau_c (N_i - N_f) \\ &= \frac{\gamma_1 V_a h\nu}{2\gamma} (N_i - N_f), \end{aligned} \tag{2.50}$$

where $(N_i - N_f)V_a$ represents the number of photons produced by the population inversion out of which $\frac{\gamma_1}{2\gamma}$ are available as output energy. Eq. 2.50 can be further refined by recalculating the integral in Eq. 2.45 with integration limits $\phi(0) \rightarrow \phi(\infty)$ and $N_i \rightarrow N_f$,

$$\begin{aligned} \int_{\phi(0)}^{\phi(\infty)} = 0 &= V_a \left(N_i - N_p \ln\left(\frac{N_i}{N_f}\right) - N_f \right) \\ \Rightarrow N_i - N_f &= N_p \ln\left(\frac{N_i}{N_f}\right). \end{aligned} \tag{2.51}$$

By defining an energy utilization factor $\eta_E = \frac{N_i - N_f}{N_i}$, Eq. 2.51 can be rewritten as

$$\eta_E \frac{N_i}{N_p} = -\ln(1 - \eta_E). \tag{2.52}$$

Inserting Eq. 2.51 into Eq. 2.50 and using Eq. 2.41 gives a simple equation for the energy per pulse

$$E = \frac{\gamma_1 V_a h\nu}{2\gamma}(N_i - N_f) = \frac{\gamma_1 V_a h\nu}{2\gamma} N_p \ln\left(\frac{N_i}{N_f}\right) \tag{2.53}$$

$$= -\frac{\gamma_1 V_a h\nu}{2\gamma} N_p \ln(1-\eta_E) = \frac{\gamma_1 V_a h\nu}{N_i}\eta_e \tag{2.54}$$

$$= \frac{\gamma_1}{2}\frac{N_i}{N_p}\frac{A_b}{\sigma}\eta_E h\nu. \tag{2.55}$$

With Eq. 2.55 the pulse width $\Delta\tau_p$ and pulse delay τ_d can be approximated by assuming that the pulse width equals the pulse energy (Eq. 2.55) divided by the pulse power (Eq. 2.46)

$$\Delta\tau_p = \frac{E}{P_p} = \tau_c \frac{\frac{N_i}{N_p}\eta_E}{\frac{N_i}{N_p} - \ln\frac{N_i}{N_p} - 1}. \tag{2.56}$$

Finally, the delay time is estimated by taking an arbitrary fraction of the number of photons at the peak, for example $\phi_p f = \phi/10$ [31]. This allows an approximation $N(t) \cong N_i$ and the integration of $\frac{d\phi}{dt}$ in Eq. 2.40 as

$$\int_{\phi_i}^{\phi_{pf}} \frac{d\phi}{\phi} = \int_0^{t_d} \left(V_a B N_i - \frac{1}{\tau_c}\right) dt$$

$$\Rightarrow \ln\frac{\phi_{pf}}{\phi_i} = \left(\underbrace{\frac{N_i}{N_p}}_{X_{th}} - 1\right)\frac{t_d}{\tau_c}$$

$$\Rightarrow \phi_{pf} = \phi_i e^{(X_{th}-1)\frac{t_d}{\tau_c}}, \tag{2.57}$$

from which τ_d can be calculated by setting $\phi_i = 1$ and $\phi_{pf} = \frac{\phi_p}{10}$:

$$\tau_d = \frac{\tau_c}{X_{th} - 1} \ln\frac{\phi_p}{10}. \tag{2.58}$$

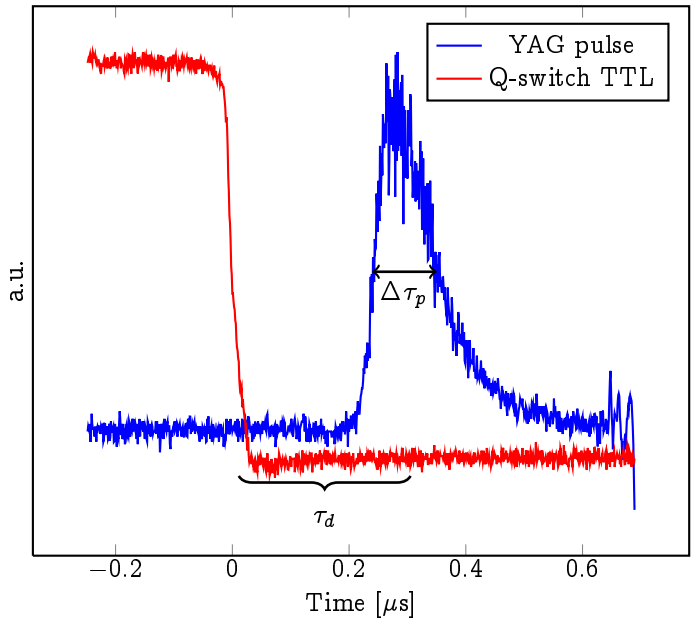

Figure 2.5. Oscilloscope traces for FURIOS Q-switched Nd:YAG laser (blue) and the TTL pulse driving the Q-switch (red).

Figure 2.5 presents oscilloscope traces for the FURIOS Q-switched Nd:YAG laser. The measured time delay between the Nd:YAG pulse and the Q-switching was estimated to be τ_d ~280 ns while the Nd:YAG width was τ_p ~60 ns. The Nd:YAG pulse width was extracted by fitting an asymmetric double sigmoidal function to the oscilloscope data using Origin [39] and taking the Full Width Half Maximum (FWHM) parameter, $w1$, as the pulse width.

These parameters can also be calculated using the equations derived in this section. Using the values for the effective resonator length $L_e = 0.74$ m and the single pass loss of the resonator $\gamma = 0.163$ calculated earlier, the Nd:YAG pulse width can be calculated starting from Eq. 2.30 which gives the photon lifetime:

$$\tau_c = \frac{0.74 \text{ m}}{3 \cdot 10^8 \text{ m/s} \times 0.163} = 1.51 \cdot 10^{-8} \text{ s}. \tag{2.59}$$

Next, the ratio X_{th} defined in Eq 2.42 is also valid for the ratio of the threshold pump power and of the incident pump power. As the Nd:YAG threshold power was

previously estimated to be about 220 W and as the measurement in Fig. 2.5 was performed with a diode electrical pump power of about 910 W, X_{th} becomes ~4.14. If the pump power noticeably exceeds the threshold power as in this particular case, the energy utilization factor can be assumed to be close to unity, for example $\eta_E = 0.95$. Equation 2.56 gives the Nd:YAG pulse width as:

$$\Delta\tau_p = 1.51 \cdot 10^{-8}\ \text{s} \frac{4.14 \times 0.95}{4.14 - \ln 4.14 - 1} \approx 35\ \text{ns}. \tag{2.60}$$

The pulse delay can be calculated once the peak number of photons in the pulse ϕ_p is known. Using the Nd:YAG crystal dimensions $l = 11.8$ cm and $r = 0.2$ cm, Eq. 2.41 yields the population inversion at the the peak as:

$$N_p = \frac{0.163}{2.8 \cdot 10^{-19}\ \text{cm}^2 \times 11.8\ \text{cm}} = 4.93 \cdot 10^{16}\ \text{cm}^{-3} \tag{2.61}$$

Using Eq. 2.45 with assumption $\phi_i \ll \phi_p$, the peak photon number becomes

$$\begin{aligned} \phi_p &= 11.8\ \text{cm} \times \pi \times (0.2\ \text{cm})^2 \times 4.93 \cdot 10^{16}\ \text{cm}^{-3} (4.14 - \ln 4.14 - 1) \\ &\approx 1.3 \cdot 10^{17}\ \text{photons}. \end{aligned} \tag{2.62}$$

Finally, the pulse delay is calculated with Eq. 2.58:

$$\tau_d = \frac{1.51 \cdot 10^{-8}\ \text{s}}{4.14 - 1} \ln\left(\frac{1.3 \cdot 10^{17}}{10}\right) \approx 180\ \text{ns}. \tag{2.63}$$

Additionally, the energy per pulse E for the Nd:YAG operating at 1064 nm can be easily calculated and compared to the experimental value of E_{exp}=13 mJ by using Eq. 2.55:

$$\begin{aligned} E_{calc} =& \frac{-ln(0.8)}{2} \times 4.14 \times \frac{\pi(0.2\ \text{cm})^2}{2.8 \cdot 10^{-19}\ \text{cm}^2} \\ & \times 0.95 \times 6.626 \cdot 10^{-34}\ \text{Js} \times \frac{3 \cdot 10^8\ \text{m/s}}{1064\ \text{nm}} \\ \approx& 36\ \text{mJ}. \end{aligned} \tag{2.64}$$

Although small discrepancies are seen between the experimentally measured data and the estimates from the theory, in general the agreement is within a factor of $\sim$ 2.

2.1.5. Wavelength selection

In order to perform laser spectroscopy, the wavelength at which the laser operates, needs to be varied. With lasers such as Dye or Ti:sapphire, the laser gain band is very broad and by default a cavity resonates at many modes resulting in a broad output linewidth. With certain optical elements the number of modes oscillating in the resonator can be reduced. This section takes a brief look into mode-selecting elements relevant for the thesis, namely birefringent filters and Fabry-Perot etalons.

The frequency separation $\Delta\nu$ of longitudinal modes in a 50 cm long laser resonator such as the approximate length of the FURIOS Ti:sapphire resonators is

$$\Delta\nu = \frac{c}{2L} = \frac{3 \cdot 10^8 \text{ m/s}}{2 \cdot 0.5 \text{ m}} = 300 \text{ MHz}, \tag{2.65}$$

hence, for example, the number of modes in a Ti:sapphire laser with a mirror set of bandwidth 25 000 GHz is $\sim$83000. As the separation of the modes is smaller than the gain profile of the laser, oscillation occurs on several modes. Figure 2.6 illustrates the mode selection using elements in the cavity.

The first element that is used to limit the laser linewidth and thus the number of modes in the resonator is a birefringent filter or a *Lyot*-filter. The basic principle is based on the modification of the polarization of the incident beam. In general a birefringent element such as a Potassium Dihydrogen Phosphate (KDP) crystal placed within the cavity changes the initial linearly polarized beam to elliptically polarized. This beam can be blocked from oscillating by adding either dedicated polarisers or relying on a suitable resonator configuration such as keeping the birefringent crystal at Brewster's angle to the incoming beam. However, in a special case the beam remains linearly polarized after passing through the crystal.

A linearly polarized plane wave (see Fig. 2.7a)

$$\vec{E} = \vec{A}\cos(\omega t - kx), \tag{2.66}$$

at $\alpha = 45^o$ with respect to the optical axis (z-axis) with $\vec{A} = (0, \mid A \mid \sin\alpha, \mid A \mid \cos\alpha)$ enters a crystal with length L_b. It is split into the ordinary E_y and extraordinary

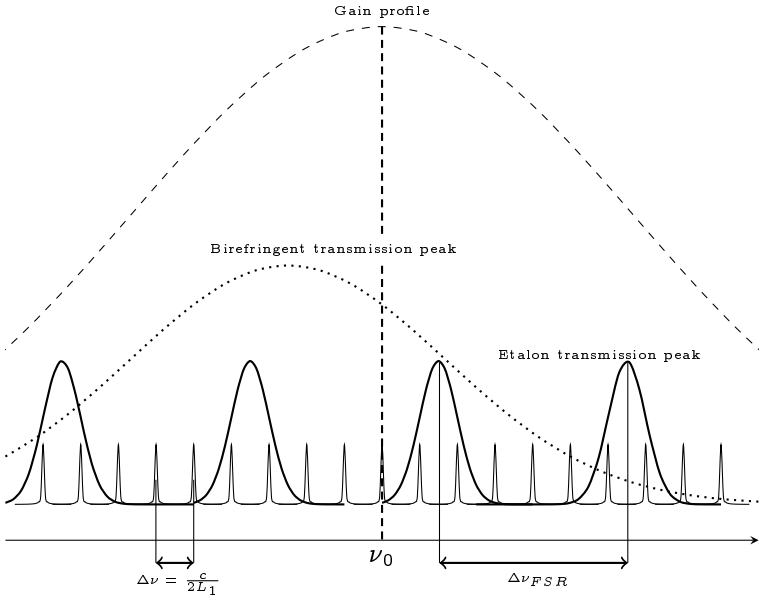

Figure 2.6. Mode selection using birefringent filter and etalon

beam E_z with wave numbers $k_o = n_o k$ and $k_e = n_e k$, and phase velocities $v_o = \frac{c}{n_o}$ and $v_e = \frac{c}{n_e}$. After the crystal, the waves

$$E_y(L_b) = A_y \cos(\omega t - k_o L_b) \tag{2.67a}$$

$$E_z(L_b) = A_z \cos(\omega t - k_y L_b), \tag{2.67b}$$

have a phase difference of

$$\phi = k \underbrace{(n_o - n_e)}_{\Delta n} L = \frac{2\pi}{\lambda} \Delta n L_b. \tag{2.68}$$

If ϕ is an integral number of 2π, e.g. $\phi = 2m\pi$, the beam keeps it's original polarization. Furthermore, the free spectral range $\Delta\nu_{BF}$, meaning the separation of two adjacent transmission peaks of the birefringent filter is now obtained by assuming that Δn does not change much over two transmission peaks. As two transmission peaks differ by $\Delta m = 1$, $\Delta\nu_{BF}$ can be calculated using Eq. 2.68

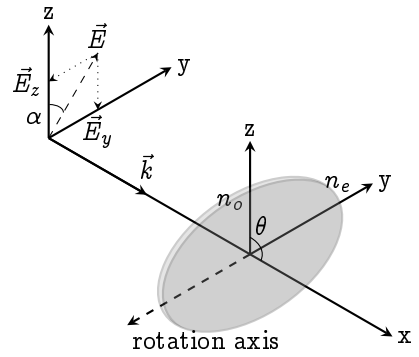

(a) A birefringent crystal with length L_b is placed at $x = 0$ with the optical axis pointing in the z-direction [32]. The wave vector $\vec{k}$ is at an angle θ with respect to the optical axis, while the electrical field vector $\vec{E}$ is at an angle α with respect to the optical axis.

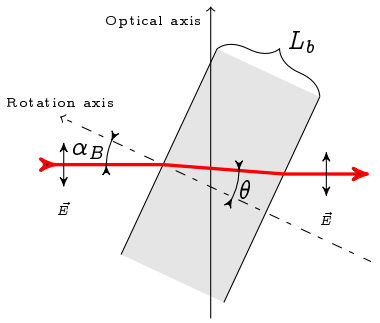

(b) A basic birefringent filter arrangement for wavelength selection. The crystal has been placed at the Brewster angle α_B with respect to the incident beam [32]. A beam with a suitable wavelength keeps its polarization while passing through the plate and is hence able to oscillate within the resonator. By changing the angle θ the transmission can be shifted.

Figure 2.7. Illustrations of the principle operation of a birefringent filter.

$$\begin{aligned} \frac{\Delta n L_B}{\lambda_1} - \frac{\Delta n L_B}{\lambda_2} &= 1 \\ \Rightarrow \lambda_2 - \lambda_1 &= \Delta n L_B \\ \Rightarrow \Delta\nu_{BF} &= \frac{c}{\Delta n L_B}. \end{aligned} \tag{2.69}$$

The index of refraction for the extraordinary wave n_e depends on the angle θ between the optical axis and the wave vector $\vec{k}$ which can be changed by rotating the crystal around the rotation axis in Fig. 2.7a, (for the basic idea, see Fig. 2.8). This changes Δn according to the equation [32],

$$\frac{1}{n_e^2\theta} = \frac{\cos^2\theta}{n_o^2} + \frac{\sin^2\theta}{n_e^2(\theta = \frac{\pi}{2})}. \tag{2.70}$$

As the birefringent filter typically selects modes that span the order of nm the laser

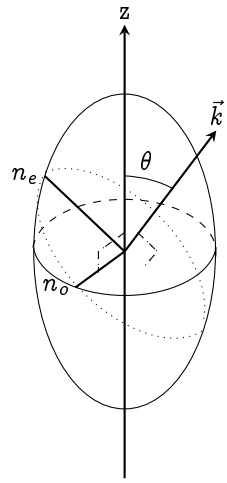

Figure 2.8. An index ellipsoid presenting the principle of varying n_e by rotating the angle between the incoming wave and the optical axis (z-axis) of the crystal. As n_e lies on a ellipse plane perpendicular to the propagation direction of the EM wave $\vec{k}$, changing θ modifies the ellipse and hence n_e.

still oscillates with multiple longitudinal modes. Therefore, in order to achieve single mode selection, a Fabry-Perot etalon is used in combination with a birefringent filter.

An etalon in its simplest form is a thin glass plate with very smooth, parallel surfaces with an anti-reflection coating for a specific wavelength range. As the light enters the etalon it undergoes multiple reflections each of which introduces a phase shift (see Fig. 2.9). When the different phases interfere constructively the wave is transmitted through the etalon with transmission peaks at frequency ν_n [31]

$$\nu_n = \frac{mc}{2n_r L_1 cos\theta'}, \tag{2.71}$$

where m is an integer, θ' is the refraction angle within the etalon, n_r is the index of refraction and L_1 is the thickness of the etalon. For the tuning of the transmission peak, the etalon needs to be tilted only slightly, meaning $\theta' \sim 0$, due to the fact that the cavity length L is much longer than the etalon thickness L_1.

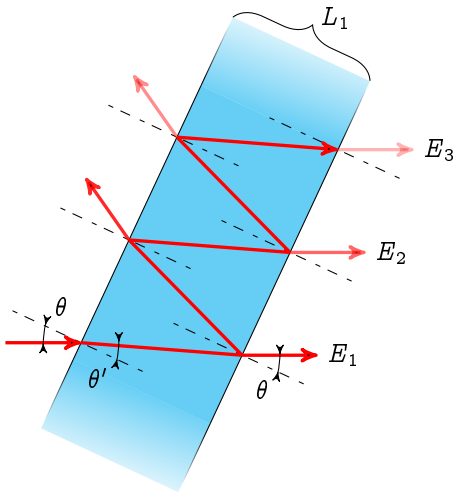

Figure 2.9. For an etalon at angle θ with respect to the incoming light beam, the light undergoes multiple reflections within the etalon. At each reflection a phase shift ϕ is introduced to the wave. After two successive reflections the phase shift is 2ϕ, i.e. a phase shift of two successive transmission peaks E_i and E_{i+1}, $i = 1, 2...$

2.1.6. Harmonic generation

The Ti:sapphire laser gain band ranges from 660 nm to 1000 nm which is in the Near Infrared (NIR) and Infrared (IR) region of the electromagnetic spectrum. For atoms, the first electronic transitions from the ground state are typically in the Ultraviolet (UV) region of the spectrum hence out of reach of the fundamental Ti:sapphire output. Harmonic generation, first demonstrated by Franken *et.al* [40], is a technique in which a suitable non-linear crystal such as BBO multiplies the frequency of the laser beam by an integer amount. Typically in solid state lasers this means Second Harmonic Generation (SHG), Third Harmonic Generation (THG) or Fourth Harmonic Generation (FHG), which extends the laser wavelength to 200-500 nm region.

When non-linear, non-centrosymmetric crystals are exposed to high electric fields the loosely bound outer electrons of atoms or molecules experience non-linear deformations [31]. The result, a dielectric polarization $\vec{P}$, of this interaction can be

described as a power series [32]:

$$\vec{P} = \epsilon_o \left(\tilde{\chi}^{(1)} \vec{E}^1 + \tilde{\chi}^{(2)} \vec{E}^2 + \tilde{\chi}^{(3)} \vec{E}^3 + ... \right), \tag{2.72}$$

where $\tilde{\chi}^{(k)}$ is the susceptibility tensor with rank $k+1$ and order k. This leads to, in SHG, the generation of a new frequency $\nu = 2\nu_1$ where ν_1 is the frequency of the incident wave entering the crystal. For an electromagnetic wave

$$\vec{E} = \vec{E_1} \cos(\omega_1 t - k_1 z) + \vec{E_2} \cos(\omega_2 t - k_2 z), \tag{2.73}$$

at a fixed location $z = 0$, the second order polarization $P^{(2)}$can be written as

$$\begin{aligned} P^{(2)} =& \epsilon_0 \tilde{\chi}^{(2)} \vec{E}^2 (z=0) \\ =& \epsilon_0 \tilde{\chi}^{(2)} \left(\frac{1}{2} (\vec{E}_1^2 + \vec{E}_2^2 + \frac{1}{2} \vec{E}_1^2 \cos(2\omega_1 t) \right. \\ & \left. + \frac{1}{2} \vec{E}_2^2 \cos(2\omega_2 t) + \vec{E}_1 \vec{E}_2 \left(\cos(\omega_1 + \omega_2)t + \cos(\omega_1 - \omega_2)t\right) \right), \end{aligned} \tag{2.74}$$

from which the second harmonic components $\frac{1}{2}\vec{E}_2^2 \cos(2\omega_2 t)$ and $\frac{1}{2}\vec{E}_1^2 \cos(2\omega_1 t)$ can be readily identified.

The intensity of the Second Harmonic (SH) frequency becomes significant only if a condition called phase matching is fulfilled:

$$\vec{k}(\nu) = \vec{k}(\nu_1) + \vec{k}(\nu_2), \tag{2.75}$$

where $\vec{k}$ is the wave propagation direction (see Fig. 2.8). If the beams propagate in the same direction, the condition can be formulated as

$$n\nu = 2n_1\nu_1, \tag{2.76}$$

hence $n = n_1$. In non-linear crystals this condition is fulfilled as they have two indices of refraction n_o and n_e. In SHG, the incident wave is polarized perpendicular to the optical axis and it depends only on n_o. The SHG wave, only depending on n_e, is polarized in a plane defined by the optical axis and the propagation direction of the incident beam $\vec{k}$ as seen in Fig. 2.8. Assuming a type-I crystal where the incident beam is an ordinary beam and the second harmonic beam is extraordinary, the phase

matching condition becomes $n_e(\nu,\theta) = n_o(\nu_1)$ which can be used to rewrite Eq. 2.70 to give a phase matching angle [31] (see Fig. 2.10):

$$\sin^2\theta = \frac{\left(\frac{n_o(\nu_1)}{n_o(\nu)}\right)^2 - 1}{\left(\frac{n_o(\nu)}{n_e(\nu)}\right)^2 - 1}, \tag{2.77}$$

where $\nu = 2\nu_1$.

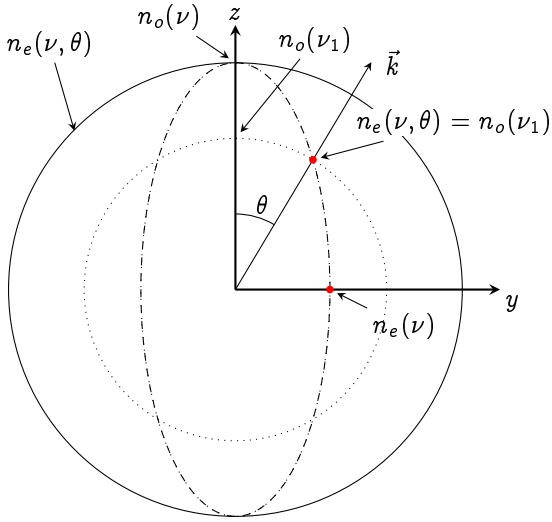

Figure 2.10. A y-z plane from Fig. 2.8 for a type-I negative uniaxial crystal, such as BBO, showing n_e and n_o for the incident wave ν_1 and the SHG wave ν. The angle θ is the angle which satisfies the phase matching condition.

For a BBO crystal with length L, the intensity of the second harmonic wave I_{SH} with angular frequency ω is:

$$I_{SH} = I(\omega)^2 \frac{2\omega^2 \mid \chi^{(2)}_{eff} \mid^2 L^2}{n^2 c^3 \epsilon_0} \frac{\sin^2(\Delta kL)}{(\Delta kL)^2}, \tag{2.78}$$

where it is assumed that the intensity of the incident beam $I(\omega)$ remains $\sim$ constant as it traverses the crystal. Here ϵ_0 is the electric permittivity. Equation 2.78 shows that the intensity of the SH beam is extremely sensitive to incident wave intensity due to $I_{SH} \propto I(\omega)^2$. Additionally, the last term in Eq. 2.78, namely $\frac{\sin^2(\Delta kL)}{(\Delta kL)^2}$, imposes a limit on the SH crystal length. If the length L exceeds the so-called

coherence length $L_c = \frac{\pi}{2\Delta k}$, the SHG and the fundamental wave begin to interfere destructively. This occurs because the waves at that point have a phase difference ϕ greater than $\frac{\pi}{2}$.

2.2. Resonance laser ionization

Ionization of neutral atoms plays a major role in the production of radioactive isotopes. High-temperature thick target and thin target catcher systems used in on-line facilities such as ISOLDE and Gesellschaft für Schwerionenforschung (GSI) [41] typically require a dedicated ionization mechanism for ionizing the reaction products. On the other hand, gas catcher -ion guide systems such as the IGISOL generally rely on the reaction products being thermalized in a buffer gas while retaining an ionic charge state. Ionization can take place, for example, via surface ionization or electron impact ionization [42]. Devices such as the FEBIAD, thermal ionizer and Electron Cyclotron Resonance (ECR) -ion sources utilize these techniques for achieving as high ionization efficiency as possible. Complementary ionization mechanisms are required for different cases depending on the element of interest and the needed beam purity. For example, while ECR ion sources can efficiently ionize even the lightest elements the ionization process lacks selectivity whereas FEBIAD or thermal ion sources can reach high ionization efficiency and selectivity for heavier elements. The selectivity in the FEBIAD ion source is achieved by utilizing different chemical properties of elements and materials. Pure noble gas beams can be produced by reducing the temperature of the ion source transfer section hence causing non-gaseous elements to be adsorbed into the walls. This principle has been further refined into a pulsed release ion source [43] whereby a variable temperature spot is introduced into the ion source. By rapidly cycling the spot temperature all reaction products are first adsorbed onto the spot and subsequently released with release time profiles depending on the chemical properties of different elements. The selectivity of the these ion source system can be further improved using methods such as decay release [44] or molecular sideband creation [42].

This thesis concentrates on another ionization mechanism, namely resonance laser ionization. It is a technique whereby an atom is ionized by promoting a valence electron over the ionization potential via a number of transitions through atomic states. The method can be combined with solid state and gaseous catchers and enables efficient and highly selective ionization of many of the elements in the periodic table. Resonance laser ionization has also led to the proposal and development of an ion source technique with the highest selectivity, namely the Laser Ion Source Trap

(LIST). This new approach has been successfully demonstrated for both hot cavity and ion guide methods and is currently under intense development. The different ion sources and their characteristics are compared in table 2.1.

Table 2.1. Comparison of different ionization mechanisms and ionization environments used in on-line facilities. The cited ionization efficiencies are only approximate due to high element dependence in some cases.

Ion source:	Ionization efficiency	Selectivity	I.P.	Charge state
Electron impact ionization	~60% [45]	None*	>7 eV	$>1^{+}$ †
Surface ionization	~100% [42]	High**	<7 eV	$1^{+}/1^{-}$
Ion guide	~0.1-10%	None	-	$1^{+}/2^{+}$
Laser ionization:				
Hot cavity	~0.1-30 % [18]	Very high	4-9 eV††	1^{+} ◇
LIST	«1% [46]	Extremely high	4-9 eV††	1^{+} ◇
Gas cell	~1-10% [47]	Very high	4-9 eV††	1^{+} ◇
Gas jet	«1%	Extremely high	4-9 eV††	1^{+} ◇

* The selectivity of the ionization process in FEBIAD ion sources can be greatly increased with methods discussed in the text.

** High selectivity if the isotopes created in the target have very different ionization potentials.

† High charge states are available for example with ECR -ion sources.

†† Typical ionization potentials reached in on-line facilities using current laser techniques.

◇ 2^{+} charge state reachable for some elements utilizing ion-resonance ionization albeit not yet demonstrated on-line.

As the atomic states of each element have unique excitation energy, the resonance laser ionization technique can be used to provide element selective ionization which can be extended, using suitable lasers, to isotopic or even isomeric selectivity. In a typical ionization scheme this means two resonant transitions from the ground state before the atom is ionized either by a non-resonant transition into the continuum, a resonant transition into an auto-ionizing state or by a transition to a Rydberg state close to the ionization potential from which the ionization takes place either via collisions or electric fields. Figure 2.11 shows different resonant ionization schemes.

In addition, a suitable transition can be made using resonant two-photon absorption in which two photons, alone without sufficient energy, hit the resonance via a virtual state. Resonance laser ionization is most efficiently performed using tunable pulsed lasers whose operating principles have been discussed in the preceding sections. Furthermore, the ionization process can be extended to optical spectroscopy in a form of Resonant Ionization Spectroscopy (RIS).

As an example, the ionization scheme involving Rydberg states in Fig. 2.11 proceeds as follows: An atom in the ground state absorbs a photon λ_1 that lifts the valence electron to state $\mid 1\rangle$. A second photon arriving within the lifetime of state $\mid 1\rangle$ excites the atom further to Rydberg levels, described by the Rydberg equation [32]

$$T_n = E_{I.P.} - \frac{R}{2(n-\delta(n,l))}, \tag{2.79}$$

where $E_{I.P.}$ is the ionization potential, R is the Rydberg constant, n is the principal quantum number and $\delta(n,l)$ is a quantum defect, l being the angular momentum of the Rydberg electron. If the Rydberg level $\mid Ry\rangle$ to which the electron was transferred is close enough to the ionization potential a suitably large electric field can remove the electron from the atom. An external field $\vec{E}_{ext} = -E^{(0)}_{ext}\vec{x}$ introduces an effective ionization potential

$$E^{(eff)}_{I.P.} = E_{I.P.} - \sqrt{\frac{Z_{eff}e^3E^{(0)}_{ext}}{\pi\epsilon_0}}, \tag{2.80}$$

where $Z_{eff}e$ is the nuclear charge screened by the electron cloud and ϵ_0 is the permittivity of free space. If the energy of the level $E(\mid Ry\rangle)$ is higher than $E^{(eff)}_{I.P.}$, the atom ionizes.

In the production of exotic isotopes the efficiency and sensitivity is of utmost importance as the production rate could be as low as a few atoms per second. The rate of detected ions $S_i[s^{-1}]$ resulting from ionization from state $\mid 2\ \rangle$ is described by [32]:

$$S_i = \underbrace{N_{g.s.}n_L\sigma_{g.s\to 2}\Delta V}_{n_a}\frac{P_{2I}}{P_{2I}+R_2}\delta\eta, \tag{2.81}$$

where $N_{g.s.}[\mathrm{cm}^{-3}]$ is the density of ground state atoms, $n_L[\mathrm{cm}^{-2}\mathrm{s}^{-1}]$ is the flux of laser photons through the interaction volume, $\sigma_{g.s\to 2}[\mathrm{cm}^2]$ is the effective cross-

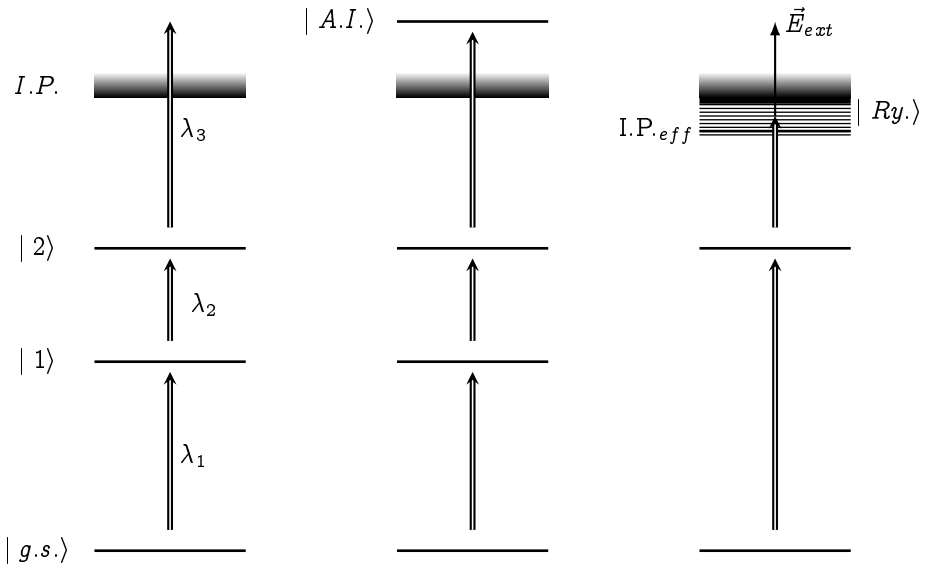

Figure 2.11. Examples of different ionization paths. Starting from the left, non-resonant ionization, autoionization and collisional or field ionization via Rydberg states. $\lambda_{1,2,3}$ are the wavelengths needed to drive the transitions.

section of transferring an electron from the ground state to state $|\,2\rangle$, $\Delta V[\mathrm{cm}^3]$ is the interaction volume, P_{2I} is the ionization probability, R_2 is the relaxation probability of state $|\,2\rangle$, δ is the collection efficiency and η is the detection efficiency. n_a is the total number of photons absorbed.

Assuming an ideal system with lossless ion collection and the condition $P_{2I} \gg R_2$, Eq. 2.81 becomes $S_i \cong n_a$. While the condition of ideal ion collection efficiency is difficult to realize, the condition $P_{2I} \gg R_2$ is easily achieved using pulsed lasers. The ionization probability $P_{2I} = \sigma_{2I} n_{L_2}$ where σ_{2I} is the ionization cross-section and n_{L_2} the photon flux of the laser driving the ionization. Inserting this back into Eq. 2.81 with conditions $\sigma_{2I} n_{L_2} \gg R_2$ and $\eta = \delta = 1$ gives the maximum achievable ion rate

$$S_i^{(max)} \cong N_{g.s.} \sigma_{g.s \to 2} n_{L_1} \Delta V = n_a. \tag{2.82}$$

To show the benefit of using a pulsed laser for non-resonant ionization into the continuum from state $|\,2\rangle$, two lasers will be compared, a 15 W CVL operating at

10 kHz repetition rate with a 20 ns pulse width and a 20 W CW laser operating at 500 nm. The corresponding photon rates are $R_{CVL} \sim 4 \cdot 10^{23}$ s^{-1} (per pulse) and $R_{CW} \sim 5 \cdot 10^{19}$ s^{-1}. Assuming a typical non-resonant ionization cross section $\sigma_{2I} = 1 \cdot 10^{-17}$ cm^2 and a radiative decay rate $R_2 \sim 1 \cdot 10^8$ s^{-1}, the required photon rate to satisfy the condition $\sigma_{2I} n_{L_2} > R_2$ becomes $n_{L_2} = 1 \cdot 10^{25}$ cm^{-2} s^{-1}. These photon intensities can be achieved by focusing the laser beams to a small area. For the CVL this area becomes a manageable 0.04 cm^2, but the CW laser beam would need to focused down to an area of $\sim 10 \cdot 10^{-6}$ cm^2. Such a focus is impractical and would generate other ionization losses due to the tiny interaction volume. Fortunately in many cases the bottleneck caused by the non-resonant ionization can be alleviated with a resonant step into an autoionizing state or a Rydeberg state close to the Ionization Potential (I.P.), gaining approximately two order of magnitude in the cross section.

In addition to the saturation conditions, efficient laser ionization requires that the laser characteristics match the properties of the ion source. For example, the velocity and hence the residence time of atoms in a hot cavity is a few 100 μs hence the repetition rate of a pulsed laser needs to be high enough in order to interrogate every possible atom. Typically the pulsed lasers used in hot cavity laser ion sources operate at ∼10 kHz. On the other hand, laser ionization performed in a gas cell can be performed using medium-repetition rate (∼200 Hz) lasers as the atoms move much more slowly. Additionally, the high pulse energy of the medium-repetition rate lasers allows the atomic transitions to be saturated more easily than with high repetition rate lasers. Recently, high- and medium-repetition rate laser based ion source systems were compared at LISOL [48] in a gas cell. The test indicated that while the lasers perform similarly in the gas cell, the high repetition rate is required for efficient ionization in the gas jet.

Due to the pulsed nature of the lasers used in on-line facilities, the typical fundamental linewidth ranges from 1 to 3 GHz. When coupled with pressure and Doppler broadening introduced by the environment of the ion source, the resulting linewidth renders the laser in many cases insensitive to the hyperfine structure. While recent developments have demonstrated that the linewidth of a 10 kHz Ti:sapphire laser may be reduced to 20 MHz [49], in-source spectroscopy still suffers from the line broadening taking place within the source. This broadening reduces the sensitivity of the method compared to other laser spectroscopic techniques such as high-resolution collinear laser spectroscopy. This latter method, performed at Jyväskylä, can reach linewidths corresponding to the natural linewidth of a transition [50]. Recent developments towards gas jet spectroscopy, including the gas jet shaping presented

in Chapter 5 of this thesis, aim to drastically reduce the environmental effects and hence enable high resolution RIS close to the radioisotope production site. However, while RIS may be less sensitive to nuclear effects than collinear laser spectroscopy, the main advantage of the method lies in its efficiency which allows spectroscopy on isotopes produced only at a rate of a few per second. Indeed, these two techniques should be viewed as being complementary to each other. The low resolution RIS method can be used to efficiently locate (unresolved) hyperfine structure of heavy elements, allowing a follow-up experiment to be made with high-resolution collinear laser spectroscopy. Such work has been demonstrated on copper isotopes at ISOLDE [51,52]. Furthermore, one may aim to indeed combine these two techniques and such efforts are currently being pursued utilizing Collinear Resonant Ionization Spectroscopy (CRIS), which has been introduced with the aim of coupling the high-resolution of collinear laser spectroscopy with the efficiency of RIS [53–55].

3. IGISOL

The IGISOL (Ion Guide Isotope Separator On-Line) facility is world renowned for producing low-energy ion beams for nuclear ground state studies [56,57]. The facility is located at the Accelerator Laboratory of the University of Jyväskylä, connected to the Department of Physics (JYFL). Before the ion guide method was developed, the standard way of extracting and transporting reaction products from a target was to use gas jets [58–60]. Based on that work the IGISOL method was commissioned at Jyväskylä in the early 1980's [61]. Though IGISOLis a versatile system the basic principles are relatively simple. In normal operation, the primary beam induces nuclear reactions in a thin target. The resulting reaction products recoil from the target and stop in a helium buffer gas volume [57] as presented in Fig. 3.1. The high first ionization potential of helium, ∼24.6 eV [62], results in a large fraction of the highly charged recoil ions thermalizing to a 2^+ charge state. In practise, due to impurities in the helium, the products are reset subsequently to a 1^+ charge state. The buffer gas pressure is typically 300 mbar and this is constantly evacuated through a ∼1 mm exit hole. Ions are transported in the gas flow to a sextupole radio frequency ion guide, the Sextupole Ion Guide (SPIG) [63].

Upon confinement in the SPIG the ions drift through with the help of a small electric field gradient before being accelerated first to about 10 keV and subsequently to the full 30 keV energy. This low energy beam is mass separated with a 55° dipole magnet and delivered to experiments. Due to efficient differential pumping the typical ion guide pressure of 300 mbar translates to a target chamber pressure of 10^{-2} mbar, then to 10^{-5} mbar in the extraction chamber before reaching a baseline pressure of a few 10^{-6} mbar in the main beam line. This drastic pressure drop of many orders of magnitude over a short distance results in a good beam quality during acceleration due to minimal ion- residual gas collisions.

For precision measurements a better beam quality is needed than normally available after mass separation. The raw IGISOL beam energy spread may be up to 100 eV, albeit much less with the SPIG, before being injected into a Radio Frequency Quadrupole (RFQ) [64] cooler buncher, a linear Paul trap filled with 1 mbar of helium buffer gas. The ions entering the RFQ are accumulated using electrical potentials while being cooled by collisions with the buffer gas. The ions are then

released either as a cooled continuous beam or in bunches with superior emittance (3π-mm-mrad at 40 keV [65]) and energy spread ($\sim$ 1eV) compared to the initial mass separated beam.

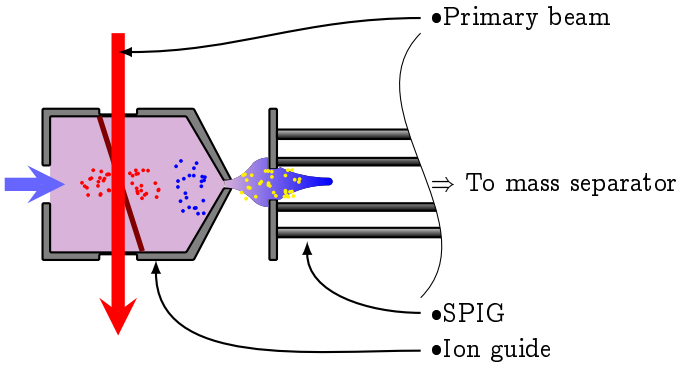

Figure 3.1. Illustration of the basic IGISOL principle. An ion guide is filled with a buffer gas at 300 mbar. A primary cyclotron beam (red) induces fission reactions in a tilted uranium target. The fission products recoil isotropically from the target and thermalize to a +1 charge state (blue dots). The gas flow takes the ions out of the cell through an exit hole into a sextupole ion guide (yellow dots).

Since the development of the IGISOL method in the early 1980's the principle has been used in many laboratories for example in Japan (Institute for Nuclear Study (INS) [66], Tohoku [67]), Poland (Warsaw Heavy-Ion laboratory [68]) and Belgium (Louvain-la-Neuve) [69, 70]. The method is compatible with different types of nuclear reactions such as fission and fusion-evaporation involving either heavy or light ions. The main advantages over the standard thick target ISOL method is that products can be released efficiently with sub-millisecond delay time [71, 72] and without chemical selectivity, meaning that even the most refractory of elements can be extracted.

3.1. Experimental tools

The IGISOL facility employs various permanent measurement devices, in addition to temporary set-ups specific only for a certain experiment. The primary tools are a Penning trap precision mass spectrometer and a collinear laser spectroscopy station both of which are introduced in the following section.

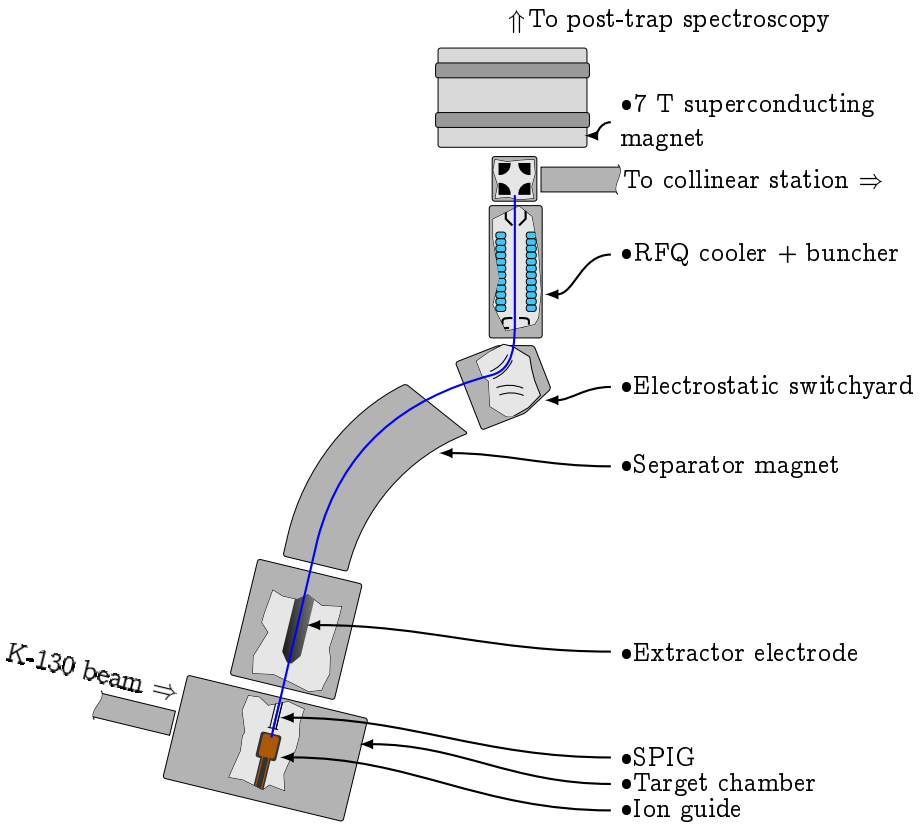

Figure 3.2. IGISOL-3 layout showing the front-end and the experimental area

Figure 3.2 shows the layout of the front-end and the Penning trap set-up of the discontinued IGISOL 3 facility. A complete description of the IGISOL-3 layout can be found in Ref. [73].

3.1.1. Penning trap

A Penning trap is an electromagnetic device used to confine charged particles in stable and predictable trajectories [74]. These trajectories, some of which are mass dependent, can be excited using suitable radio frequency fields [75]. The mass dependency of the motion of a particle within the trap allows a very precise determination

of the ion's mass [76]. The mass resolving power of a Penning trap can exceed $1 \cdot 10^7$ and hence enables not only the precision measurement of mass but also the separation and discovery of nuclear isomeric states [77, 78].

After the first demonstration of a mass measurement of radioactive isotopes with a Penning trap at ISOLDE [79, 80], the technique has been taken into use in many on-line facilities around the world including GSI (Separator for Heavy Ion reaction Products (SHIPTRAP)) [81], TRIUMF (TRIUMF's Ion Trap for Atomic and Nuclear science (TITAN)) [82], Argonne National Laboratory (ANL) (Canadian Penning Trap (CPT)) [83], Michigan State University (MSU) National Superconducting Cyclotron Laboratory (NSCL) (The Low Energy Beam and Ion Trap (LEBIT)) [84] and IGISOL [85, 86]. For a complete overview of Penning trap operating principles and facilities the reader is referred to Ref. [87] and the references therein.

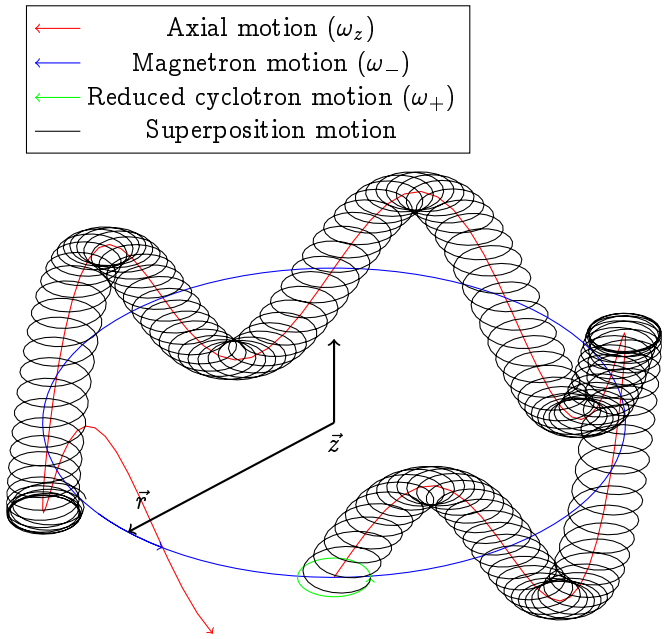

Figure 3.3. Eigenmotions of an ion in a Penning trap.

The Penning trap confines ions in a superposition of a quadrupole electric field $\vec{E}$ and a highly homogeneous magnetic field $\vec{B}$ [74]. A strong magnetic field confines the ions radially along the magnetic field axis and the axial confinement is achieved

with the electrical field. All the forces acting upon the ion with a charge q can be described with the Lorentz force

$$\vec{F} = q\left(\vec{r} \times \vec{B} + \vec{E}\right). \tag{3.1}$$

Solving the equation of motion for an ion in a Penning trap results in three frequencies, a harmonically oscillating axial frequency ω_z, a mass-dependent reduced cyclotron frequency ω_+ and a mass-independent magnetron frequency ω_-. The individual motions with the resulting superposition motion are presented in Fig. 3.3. In an ideal trap the two latter frequencies sum to a mass-dependent cyclotron frequency:

$$\omega_c = \omega_+ + \omega_- = \frac{qB}{m}, \tag{3.2}$$

where q is the charge, m is the mass of the ion and B is the magnetic field strength. The ion motions can be excited using dipole RF fields oscillating at the eigenfrequency and can be converted from one motion to another with quadrupole RF fields [88].

The JYFLTRAP Penning trap mass spectrometer is a dual trap system located within a 7 T superconducting magnet [85]. The two traps, namely purification and precision trap, are formed with cylindrical electrodes and are separated with a narrow diaphragm. The purification trap captures the ion bunches from the RFQ in dilute helium gas which cools the ions. The magnetron motion of the ions is excited with dipole RF fields to increase the radius so that it is larger than the diameter of the diaphragm. After this a mass selective quadrupole excitation is applied at the reduced cyclotron frequency to center the isotope of interest onto the trap axis [89]. Due to the differences in the orbits only the ions of interest can transfer to the precision trap [90].

In the precision trap the pure ion sample is excited to a larger magnetron radius followed by a quadrupole excitation to convert this motion to reduced cyclotron motion. This method increases the radial velocity of the ions which translates to a reduction in the time of flight to a multichannel plate detector when the ions are released from the trap. By determining the excitation frequency which leads to the shortest time of flight [91], it becomes possible to determine the mass of the ion. Comparing the frequency of the isotope of interest to the frequency of a reference isotope with mass m_{ref}

$$m = \frac{\nu_{ref}}{\nu}\left(m_{ref} - m_e\right) + m_e, \tag{3.3}$$

yields the isotope mass m. Here m_e is the electron mass.

JYFLTRAP has been used to measure a wide range of masses with high precision. The complete list of JYFLTRAP mass measurements to date is presented in Ref. [86]. These results have been used, for example, to study the evolution of the N=50 shell gap energy in the neutron rich region [92]. This particular measurement provided evidence for a reduction in the shell gap far from stability. Another good example of the versatility of the trap system is the study of Q values for super allowed β decays. Such measurements are used to test the unitarity [93] of the Cabibbo-Kobayashi-Maskawa Matrix (CKM) matrix [94] by deducing a very precise value for the V_{ud} matrix element [95, 96]. In addition to fundamental physics the trap can be used to produce ultra-pure samples of an isotope/isomer for selected applications. For example, the Comprehensive Nuclear-Test-Ban Treaty Organization (CTBTO) has measurement stations around the globe that measure the ratio of an isomer ^{133m}Xe to the ground state ^{133}Xe. As the ratio of these depends on the source in which they were produced, they can be used to detect nuclear device detonations. The measurement stations need to be calibrated and standardized with a pure sample of ^{133m}Xe which, at the moment, can only be produced using Penning traps [97].

3.1.2. Collinear laser spectroscopy station

Collinear laser spectroscopy is a well established method of probing atoms and ions in order to extract nuclear ground state properties across the nuclear landscape [98]. The method achieves high precision due to the use of narrow linewidth CW lasers combined with a highly reduced Doppler broadening of a transition of interest on an accelerated ensemble of atoms or ions. Such high resolution is sufficient to allow a measurement of the hyperfine structure of a transition of a given isotope. From the hyperfine spectrum, it is possible to extract nuclear spin, magnetic dipole and electric quadrupole moments. Additionally, via a measurement of the frequency shift from one isotope to another, the change in root mean square charge radii can be deduced. The fundamentals and current status of collinear laser spectroscopic measurements among other laser spectroscopic tools used to study short-lived isotopes is presented in a topical review by B. Cheal and K. Flanagan [55].

Collinear laser spectroscopy on ions was first independently demonstrated in 1976 by Wing *et al.* [99] and Kaufman *et al.* [100], and was soon after demonstrated by Anton *et al.* [101] for fast atomic beams. In the technique an ion or atom beam is overlapped with a co- or counter-propagating laser beam operating at a locked frequency. The ion beam is typically accelerated to some tens of keV energies which reduces the

initial longitudinal energy spread to the natural linewidth of the transition. Rather than tuning the laser frequency, the ion or atom is Doppler shifted over the atomic resonance by tuning the total acceleration voltage V. The frequency seen by the ion or atom is related to the acceleration voltage as

$$\nu = \nu_L \left(1 + \alpha - \sqrt{(2\alpha + \alpha^2)}\right), \tag{3.4}$$

where ν is the laser frequency seen by the ion(atom), ν_L is the locked laser frequency and $\alpha = \frac{eV}{mc^2}$ where m is the ion's mass and q is the charge [55]. The method of Doppler tuning the ion or atom beam velocity removes uncertainties associated with tuning the laser frequency. When on resonance, the fluorescence is detected with photomultiplier tubes.

Collinear laser spectroscopy stations are currently used in many nuclear physics laboratories around the world. The technique can be combined with standard isotope production methods such as the ISOL method at ISOLDE [98, 102] or TRIUMF [103,104], and the IGISOL method [105,106]. The collinear laser spectroscopy station at IGISOL was set up in the mid 90's as a collaboration between the University of Jyväskylä, the University of Manchester and the University of Birmingham. The first measurement of radioactive ions was performed in 1997 on barium [106,107], followed by the first collinear laser spectroscopy measurement on a refractory element in 1998 [108,109]. With the introduction of the RFQ cooler buncher [65] the sensitivity of the method gained a huge boost [110]. The improvement led to a greatly reduced energy spread and the possibility to gate the photomultiplier tubes in order to only accept photons corresponding to the arriving ion bunches. All this paved the way for a first collinear measurement of cooled fission fragments at IGISOL [111].

Collinear laser spectroscopy has been used at IGISOL to study the onset of deformation around N=60 [112–115] and ground state properties over the N=28 shell closure [116]. The current status and recent achievements at IGISOL are documented in an article by F. Charlwood *et al.* [117]. Currently, the laser station is being rebuilt at the new IGISOL-4 facility and will be commissioned in 2012.

Optical ion manipulation

In a typical measurement, collinear laser spectroscopy is performed from the atomic or ionic ground state to an excited state. However, in some cases this transition is either too weak, unfavourable for extracting nuclear parameters or beyond the wavelength capabilities of a CW laser. For example, the nuclear spin cannot be

determined unambiguously if the transition takes place between states with spins $J = 0 \rightarrow J' = 1$ or $J = 1/2 \rightarrow J' = 1/2$ due to insufficient hyperfine peaks available. In the latter case the determination of the quadrupole moment is also impossible [55, 118].

These problems can be solved if the spectroscopy can be performed from another state with suitable spin and transition strength. In principle this means the use of metastable states which may be populated only weakly in the ion guide and hence be otherwise unavailable by default. Using high power pulsed lasers, such as Ti:sapphire lasers, even weak transitions can be driven efficiently and as the purpose is not to do spectroscopy but only to drive a transition the broad linewidth is not an issue as much as it is an advantage. While in the RFQ cooler buncher, the ion energy spread matches the broad, few GHz, linewidth of a pulsed Ti:sapphire laser hence increasing pumping efficiency. By choosing a suitable transition which subsequently transfers the population to a metastable state with a large probability (see Fig, 3.4a), the ground state population can be sometimes be completely depleted, as seen in Fig. 3.4b [114].

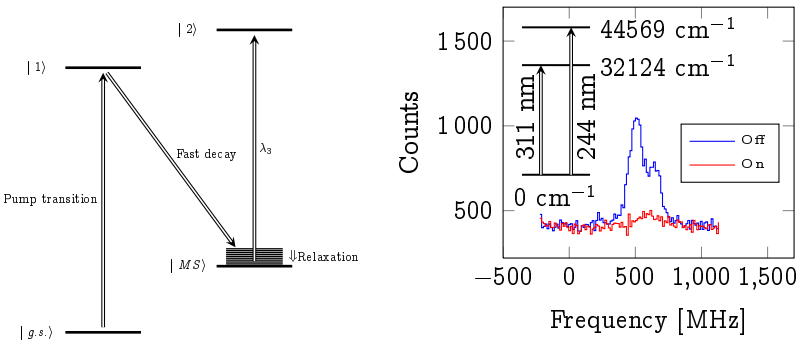

(a) The basic idea of optical pumping. The transition $|\, g.s.\rangle \rightarrow |\, 1\rangle$ is driven by a pulsed Ti:sapphire laser. State $|\, 1\rangle$ decays to a metastable state $|\, MS\rangle$ from which collinear laser spectroscopy is performed on a transition to state $|\, 2\rangle$.

(b) An example of optical pumping in Y^+. The plot shows how the ground state is completely depleted by the 224 nm pump laser. The frequency is relative to a 311 nm collinear laser transition.

Figure 3.4. The idea for optical pumping and an example of the effect of optical pumping on the ground state population of Y^+ ions. Data by courtesy of B. Cheal.

3.1.3. IGISOL-4

The IGISOL facility is undergoing the fourth major upgrade since the conception of the ion guide method almost 30 years ago, with the move to a new experimental area next to a recently acquired MCC-30/15 light ion cyclotron. The machine can deliver 18-30 MeV protons and 9-15 MeV deuterons at beam currents up to 200 μA and 62 μA, respectively. The utilization of the heavier beams from the existing K-130 cyclotron will also be possible at the new facility.

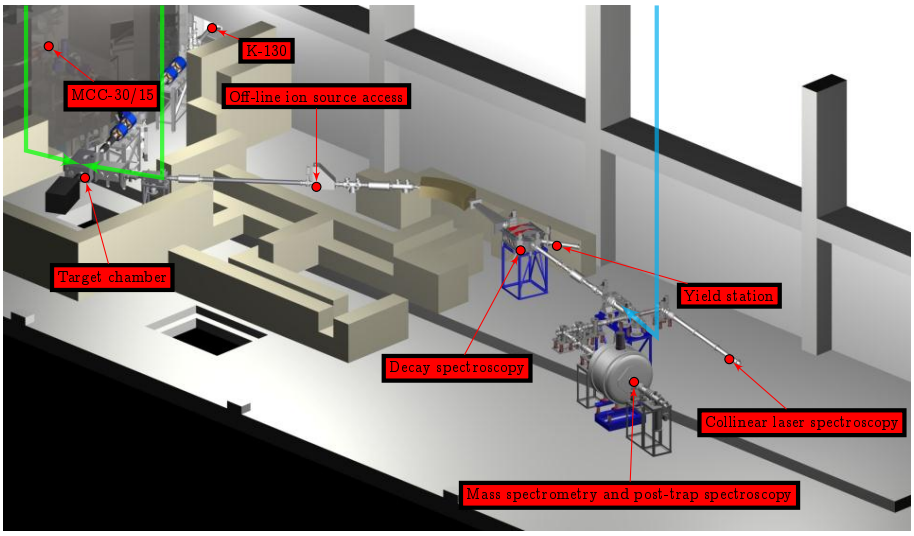

Figure 3.5. IGISOL-4 layout presenting the front-end and the experimental hall. The laser access to the target chamber is marked in blue and laser access for optical manipulation in cyan.

The new experimental hall presented in Fig. 3.5 enables several improvements to the general facility including more effective beam transportation, better access to the target area with lasers, installation of off-line test ion sources, and more sophisticated and permanent measurement and beam diagnostic set-ups.

Intense light ion beams make possible the use of both fusion and fission reactions providing access to light proton-rich nuclei and an extended range of neutron-rich nuclei. A new neutron converter target is being designed in order to take full advantage of the high intensity beam from the light ion cyclotron. This will allow the production and systematic study of ever more exotic nuclei produced in neutron-

induced fission reactions using the existing trap and laser facilities. The construction of IGISOL-4 is nearing completion and the first on-line beam tests have already been performed. Continuation of the experimental program at IGISOL is expected to take place towards the end of 2012.

4. FURIOS laser ion source at IGISOL

The following chapter presents FURIOS, the Fast Universal Resonant laser IOn Source, a new gas cell designed for in-source laser spectroscopy, initial results obtained under pseudo-on-line conditions and a data analysis software developed towards future high resolution in-source spectroscopy.

The FURIOS laser set-up, the Ti:sapphire laser basic operation and technical details of wavelength selection and harmonic generation are discussed. Recent results on the effect of the Ti:sapphire crystal temperature on the fundamental and intracavity generated second harmonic output power are presented. Concerning the new IGISOL 4 facility, the design of the new FURIOS facility and the laser transport are discussed. In addition, the issues concerning short laser ion pulse detection and wavelength monitoring are presented.

Following the description of the FURIOS -facility, a new type of ion guide, namely the "shadow gas cell", originally designed by the Leuven laser ion source group, [119] is introduced. The aim for the ion guide is to allow efficient in-source laser ionization under on-line conditions. The results obtained with this gas cell include transport efficiency determination using an alpha recoil source and ion source commissioning under off- and pseudo-on-line conditions using stable nickel. Finally, a new software for the analysis of hyperfine structure is presented. A non-linear regression of a Voigt profile on collinear laser spectroscopy data on niobium and a errors-in-variables linear fit on nickel isotope shift data are presented as a demonstration of the current status of the analysis software.

4.1. Introduction

In a typical IGISOL experiment where the reaction products are primarily thermalized in a 1^+ charge state, the element of interest might form only a small fraction of the total ensemble of ions. When the ions enter the IGISOL separator magnet, the magnet selects all ions with a given charge to mass ratio $\frac{q}{m}$ therefore isobaric contamination may still be present in the mass separated beam. Such contamination could prevent the detection of the isotope of interest, for example, with gamma ray detec-

tion by introducing a high background that masks the gamma rays associated with the exotic isotope. Furthermore, the RFQ has a limit in the number of ions it can capture hence the contaminant species may well overwhelm the storage capability of the device, thus reducing the transmission. Additionally, isobaric contaminants in the ion beam delivered to the collinear laser spectroscopy station introduce fluorescence background (in the form of ion beam -related laser scatter). Impurities in the cooled and bunched beams delivered to JYFLTRAP may also contribute to limitations in the capacity of the trap to fully purify beams.

If the majority of the reaction products were to be neutralized in the ion guide the isobaric contaminant problem could be addressed at the source. Resonant laser ionization is a mechanism which provides element selectivity in the ionization process. By coupling laser ionization with the mass selectivity of the separator magnet, isotopically pure beams can be delivered to the experiments.

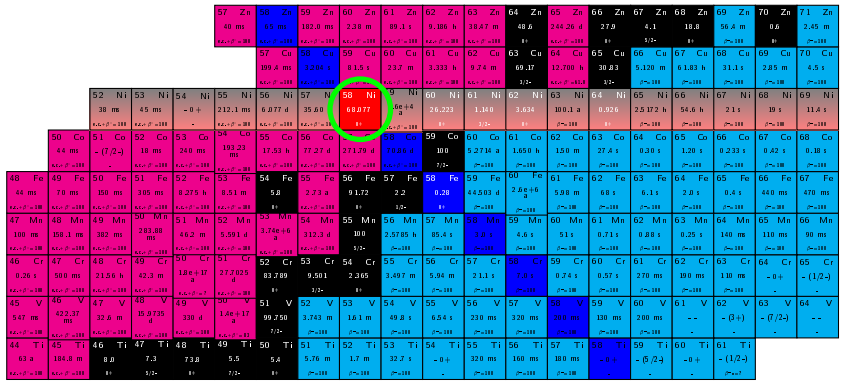

Figure 4.1. A selected region of the Segré chart showing how the isotopic selectivity is achieved with the combined use of lasers and a separator magnet. The lasers provide element selectivity (Ni) and the separator magnet selects according to mass (dark blue) leading to a selection of a single isotope (red). Other colours according to Fig. 1.1.

As stated in Chapter one, laser ion sources have become a vital part of the operation of many of the major on-line facilities. In 2004 a collaborative project was started with the LARISSA -group at the University of Mainz aimed towards the construction of a laser ion source [120] at the IGISOL facility. The facility became operational soon after with the first off-line ions of Tc [121], Bi [122] and Y [123] and it has since been developed towards resonance laser ionization in a gas cell under on-line conditions [124]. The latter work used the laser ion source to develop an understanding of the

competing processes acting in the gas cell. Thus far, the laser ion source has not been used for its principal purpose - to selectively produce low energy radioactive ion beams - due to high losses in laser intensity during the complex transport to the gas cell of IGISOL-3. The new IGISOL-4 facility has involved detailed planning for the laser ion source in the initial stages, and the author has been principally involved in all the details related to the design of the new laser ion source to be commissioned in 2012.

Resonance laser ionization is a selective process that can reach efficiencies of 10-30 % [18]. In addition, resonance ionization spectroscopy (RIS) has developed into a formidable tool for the study of exotic, short-lived radioisotopes. Recent results such as the determination of the magnetic moments of ^{57,59}Cu [125], the investigation of intermediate and auto-ionizing states in heavy elements [126] and the measurement of the hyperfine structure of ^{229}Th [127] are excellent examples of the power of the RIS method.

This chapter presents additional developments of the FURIOS laser ion source to those discussed in Article **I**, published in Eur. Phys. J. A 43 (2012) [128]. Three major laser-related developments are presented in the article: intra-cavity second harmonic generation, narrow-linewidth injection-locked Ti:sapphire laser and grating-based Ti:sapphire laser. The intra-cavity harmonic generation has led to a huge increase in the second harmonic output power as well as to greatly improved beam divergence. The injection-locking technique has been successfully tested at the University of Mainz and has shown to be able to reduce the laser linewidth to $\sim$20 MHz. In the near future, a new injection-locked Ti:sapphire set-up will be constructed which will allow efficient high-resolution in source spectroscopy to be performed at JYFL. Finally, a new grating-based Ti:sapphire laser has been developed, whereby the high reflector of a typical Ti:sapphire resonator has been replaced with a gold coated grating. The lasing wavelength is selected by rotating the grating with respect to the cavity mode which allows, in principle, the whole Ti:sapphire gain band to be scanned. This laser is invaluable for the development of new ionization schemes which is demonstrated in the article with samarium.

The second part of the article discusses in-source and in-jet resonance ionization spectroscopy using pulsed lasers. As the name implies, in-source resonance ionization spectroscopy is performed within the gas volume of an ion guide whereas in-jet spectroscopy is performed in the supersonic jet emitted from the ion guide. Though both of the methods are susceptible to the environment they are performed in, these effects are greatly reduced in the jet. The effect of environmental broadening mechanisms, different laser bandwidths and variations in laser intensity on the width

of the measured spectral line have been studied using bismuth, silver and nickel, in the gas cell and expanding gas jet. Power broadening due to laser intensity was studied on the first excitation at 328.1624 nm of atomic silver. These studies revealed a ∼3 GHz increase in the linewidth at high laser intensities compared to a baseline. In-source spectroscopy of bismuth revealed a pressure induced broadening of ∼10 MHz/mbar while in-jet spectroscopy of nickel showed a slight decrease of the linewidth compared to a corresponding in-source measurement. Finally, the application of a de Laval nozzle led to remarkably collimated gas jets which overcome a current limitation in the gas cell-based LIST method.

4.2. FURIOS laser system

The FURIOS laser system consists of multiple high repetition rate pulsed lasers. These include two Nd:YAG lasers (Lee Laser LDP-200MQG) operating at 10 kHz with optimal output powers of 80 W and 40 W respectively. The 80 W Nd:YAG is used to pump four Ti:sapphire lasers that form the backbone of FURIOS. The general layout of the main optical table at the IGISOL-3 facility is presented in Fig. 4.2. The second Nd:YAG is reserved as a backup laser and for the development of an injection-locked Ti:sapphire laser [49]. A CVL laser with a typical output power of 30 W is used mainly for non-resonant ionization, however it can be used to pump a dye laser if needed. In general, the laser system is capable of covering wavelengths ranging from 205 nm to 1000 nm and thus is able to produce ionization schemes for many elements in the periodic table. Figure A.1 (in the appendix) shows the elements that have ionization schemes suitable for Ti:sapphire lasers.

The Ti:sapphire lasers used at FURIOS are based on the original design by the LARISSA group at the University of Mainz [129] . The laser cavity is arranged in a Z-shape (see Fig. 4.3) that allows the Ti:sapphire crystal to be pumped from one or two directions depending on the need [121]. The pump beam is focused into either the front or backside of the crystal and concave, R= 75 mm, high reflective mirrors are placed either of the crystal with 2 cm and 5 cm separation respectively. The resonator is completed with a high reflector (R>99.9 %) and an output coupler (R ∼80 %). The wavelength selection is achieved with a birefringent filter and a thin etalon resulting in a typical output linewidth of about 3 GHz [128, 130]. In a typical experiment the output of one or two of the lasers needs to be delayed using Pockels cells in order to time synchronize the output pulses to within a few ns.

The resonator can be reconfigured for intra-cavity doubling by replacing the output

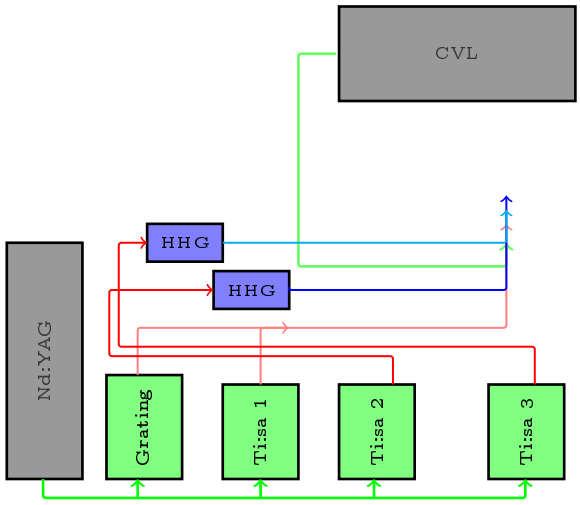

Figure 4.2. The layout of the optical table for the FURIOS laser ion source during IGISOL-3.

coupler with a high reflector to form a closed resonator for the fundamental wavelength. By adding a BBO crystal within the cavity along with a suitable dichroic mirror, a significant fraction of the fundamental frequency can be converted to second harmonic SH output. An SH output of about 3.7 W has been reached using this intra-cavity approach. Figure 4.3 shows the schematic representation of the Ti:sapphire resonator in the intra-cavity configuration. Figure 4.4 presents recent data on the performance of two of the lasers, one in standard mode (upper half) and one in intra-cavity mode (lower half). The left column gives the output power as a function of input pump power and the right column as a function of the Ti:sapphire crystal temperature. A Ti:sapphire conversion efficiency of 27 % can be extracted from the gradient of the data for the standard mode and a corresponding second harmonic conversion efficiency of 3.9 % for the intra-cavity mode. It should be noted that the results are obtained using a bare cavity with no mode selecting elements therefore the intra-cavity efficiency may be lower than normal due to multiple mode structure. The standard mode utilized a mirror set with 750 nm central wavelength and the intra-cavity mode utilized a mirror set with 850 nm central wavelength.

In the past, the effect of the Ti:sapphire crystal temperature on the output power was an unknown variable, however it had been seen that if the water cooling malfunctioned the power dropped due to thermal effects. Recently, a variable temperature

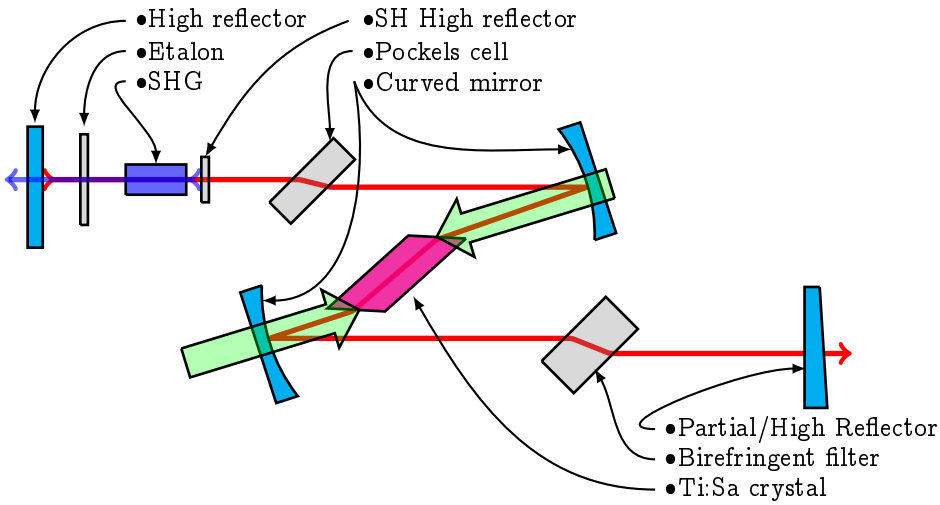

Figure 4.3. Schematic representation of the Ti:sapphire resonator at FURIOS showing the laser operating with intra-cavity second harmonic generation. The Ti:sapphire crystal may be pumped from one or both sides.

chiller for Ti:sapphire cooling was installed which allows the crystal to be cooled to about 14 °C. The data in the upper right plot in Fig. 4.4 shows that the output power keeps rising steadily below 25 °C at a rate of about 20 mW per centigrade, however no large gain in output power is observed. Reducing the crystal temperature reduces thermal lensing effects in the crystal and may, in cases where the output power is limited by thermal effects, increase the output capability of a Ti: sapphire crystal by a factor of 200 at 77 K [53]. The modest temperature dependence of the output power in this case indicates that that the thermal effects are not a limiting factor for the Ti:sapphire output power. Nevertheless, the effect of the crystal temperature on the intra-cavity SH power is more dramatic, with an improvement of ∼100 mW with a reduction of ∼ 5 °C.

In addition to the standard resonators the set-up includes a Ti:sapphire laser whereby the high reflector and the mode selecting elements have been replaced with a grating which allows in principle a tuning of the laser wavelength across the entire Ti:sapphire gain band. The grating-based laser in presented in Article **I**.

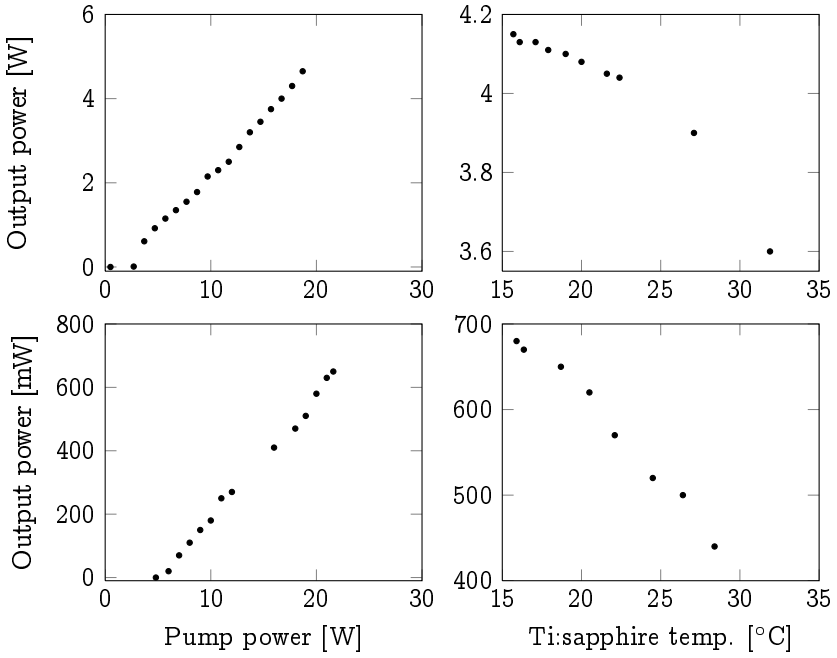

Figure 4.4. Output powers for Ti:sapphire lasers operating in standard mode (upper half) and in intra-cavity mode (lower half) as a function of the pump power (left column) and the crystal temperature (right column). The threshold pump power extracted from the upper left plot is ∼2W.

4.3. Laser ion source design considerations

The FURIOS project was first constructed at the existing IGISOL-3 facility thus the design was limited by the existing physical restrictions. Multiple compromises had to be made with respect to the laser transportation and laser coupling to the gas cell. The laser transport path required several mirrors, many of which were placed at non-optimal angles. In the worst cases, the transport losses for deep UV light exceeded 80 %.

For the operation of an efficient and reliable laser ion source the optimization of the laser transport path is vital [131]. Therefore, during the design of the new IGISOL-4 -facility [132], the laser ion source had a high priority. The flexibility in design allowed the laser laboratory to be placed in an optimal location with respect to the

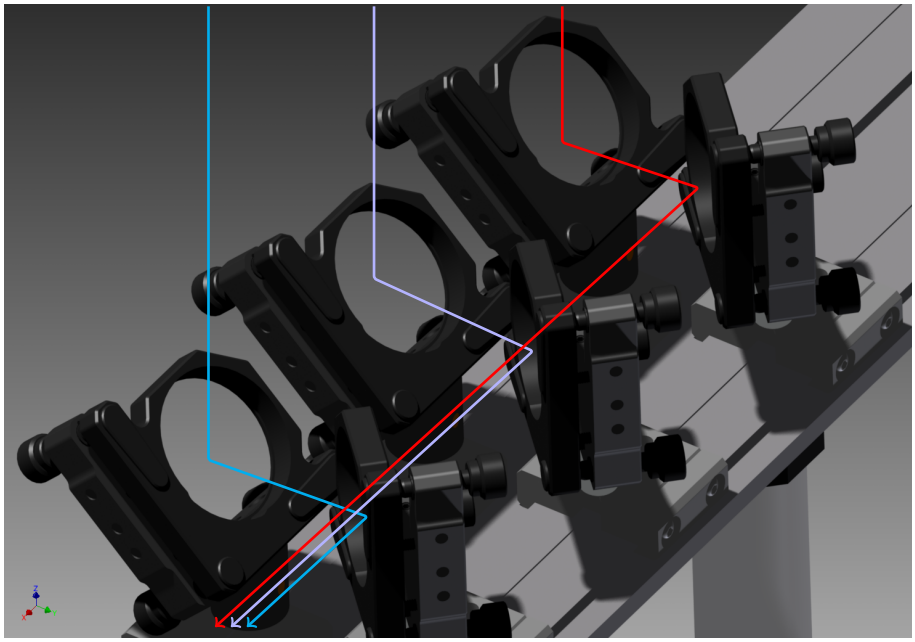

Figure 4.5. CAD design of the laser combining system. Two set-ups have been made to couple the lasers into the IGISOL target chamber from the front and from the back.

target chamber and the IGISOL cave to be constructed in a manner that allowed a simple and optimal positioning of the laser transport mirrors. Furthermore, the laser optical path was designed to allow all beams to be transported separately to the target area where they would be combined and focused into the target chamber. This allows the mirror coatings to be chosen specifically for the wavelength being transported.

The design of the new FURIOS laser ion source station for IGISOL-4 was done using 3D mechanical design program (Autodesk Inventor). Figure B.1 (in Appendix) shows the entire IGISOL-4 upper level as a 3D illustration and Fig. 4.5 presents a typical mirror set-up used to combine the individual lasers and to couple them into the IGISOL target chamber.

4.3.1. Detecting laser ion pulses

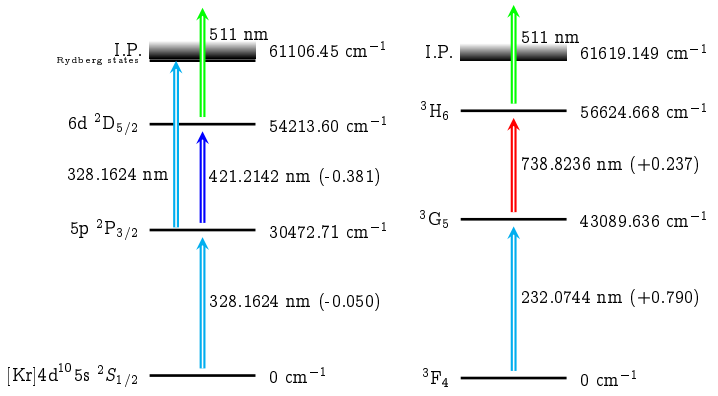

(a) Silver ionization scheme **(b)** Nickel ionization scheme

Figure 4.6. Resonant ionization schemes for silver and nickel. The transition strength is given where known. The non-resonant 511 nm light is produced with a CVL laser. In the case of silver, each of the lasers are able to ionize from the 6d^{2}D$_{5/2}$ state.

The resonant laser ionization process produces short, ~40 ns, ion pulses at a 10 kHz ionization rate. At FURIOS and at IGISOL two types of ion detectors are used, an electron multiplier tube and a micro-channel plate, both of which operate on the principle of secondary electron emission that leads to electron multiplication.

At FURIOS, the off-line calibration and development of laser excitation and ionization schemes have been performed with the Atomic Beam Unit (ABU). A detailed description of the ABU can be found in [133] but the basic operational principle can be summarized as follows: an atomic vapour from a resistively heated oven enters the laser interaction region where the atoms of interest are resonantly excited and ionized in a crossed-beams geometry. An electrostatic lens system extracts the ions and guides them to an Electron Multiplier Tube (EMT) (ETP Electron Multipliers, model 14150H) which outputs a fast pulse for each ion hitting the detector. The signal from the EMT is fed to a fast amplifier unit (ORTEC 820), followed by a coincidence unit triggered by a gate from the Nd:YAG pump laser. Finally, counting only the ions in coincidence with the gate leads to a considerable reduction of background signal produced, for example, by the interference from the Q-switches of the pulsed laser system.

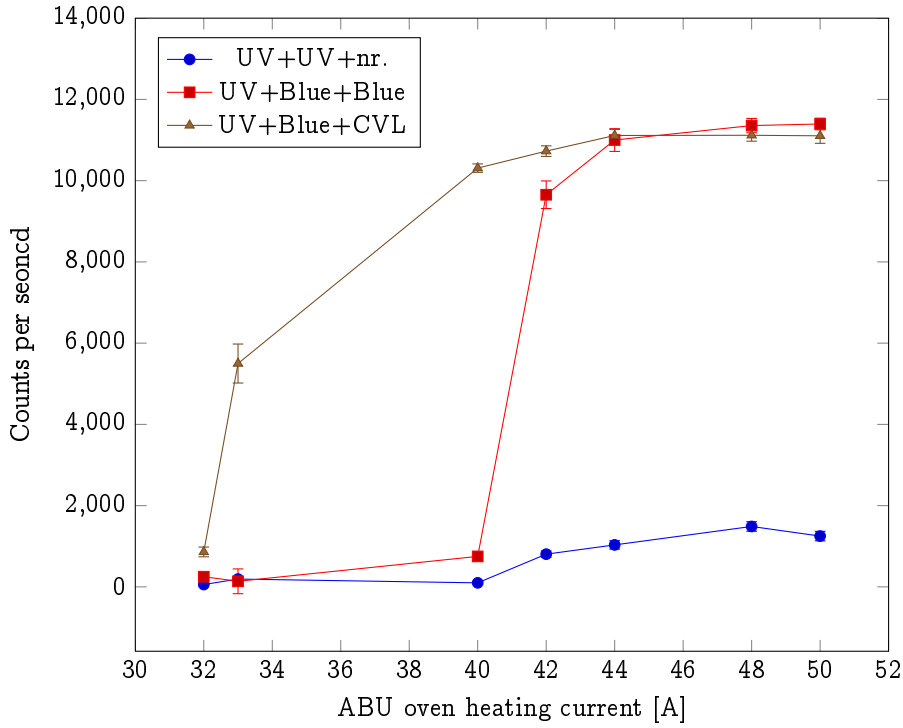

Figure 4.7. Count rate behaviour as a function of oven current for the resonant laser ionization of silver. The contributions of the individual excitation and ionization steps are shown separately. The primary ionization path is displayed in the legend, where UV= 328.1624 nm, Blue=421.2142 nm, CVL= 511 nm and nr. corresponds to a a non-resonant ionization mechanism. The solid lines are to guide the eye.

Several ion counting measurements in the ABU have resulted in the observation of count rate saturation at the laser repetition rate, i.e. 10 kHz. This effect has also been noticed in tests with the hot cavity laser ion source at IGISOL in a perpendicular laser ionization geometry [134], and has been attributed to the ion pulses being counted as a single event. The maximum count rate of the EMT is about 125 MHz due to an 8 ns baseline width of the EMT signal [135]. The lower limit of the ion pulse duration is set by the laser pulse width which is, for the case of the Ti:sapphire lasers, $\sim$ 40 ns, and for the non-resonant ionization with the CVL, $\sim$ 20 ns. Although the ion pulses are created every 10 kHz, the instantaneous count rate can exceed the count rate limit of the EMT if more than a few tens of ions hit the

detector during the pulse duration. In such cases the individual ions are no longer counted separately.

The apparent saturation of the ion count rate limits the ability to extract information from the scans such as transition saturation intensities, broadening of the linewidth and in the worst case scenario, peak centroids due to a flat-top behaviour. The effects of the detector saturation were studied in detail using laser ionization of nickel and silver. The silver ionization is realised with three-step UV-blue-CVL resonant ionization scheme (two resonant excitation steps and a non-resonant ionization step) described in [134]. The scheme allows ionization, albeit inefficiently, using only the first UV transition due to a suitable Rydberg state close to the ionization potential which matches the energy used in the first resonant step [136]. The nickel ionization scheme includes a 232.0744 nm UV transition followed by a resonant 738.832 nm step and finally a CVL-induced non-resonant ionization process. Both schemes are presented in Fig. 4.6.

The effect on the silver ion count rate as a function of ABU oven current is shown in Fig. 4.7, which illustrates separately the contributions from the different possible laser excitation and ionization steps. A rapid increase in count rate is seen as the additional excitation steps are added, leading to saturation at approximately the repetition rate of the laser system. On the other hand Fig. 4.8 shows the count rate behaviour as a function of the laser intensity for a UV+UV+non-resonant ionization scheme. The ionization takes place via Rydberg states close to the ionization potential by a non-resonant mechanism.

The electric field within the ionization region of the ABU is about 25 V/mm. However, the critical field E_c for field ionization can be calculated to be about 52 V/mm using the formula [137] $E_c = 3.21 \cdot 10^8/n^4$[V/cm], where $n = 28$ is the principal quantum number for the state in question. Hence, field ionization can be excluded as an ionization mechanism. The (undetermined) non-resonant ionization mechanism leads to a very large spread (25 μs) in the ion arrival time hence enabling the EMT to count all the ions. A similar situation has been observed in gallium [133] where an $\sim$ 11 μs arrival time spread was observed. In this work, when the ion count rate was increased beyond 10 kHz and the other lasers were introduced, the rate dropped back to the saturation level seen in Fig. 4.7.

In addition to the ion counting mode, the EMT allows the measurement of the anode current after the discrete-dynode stage. Fig. 4.9 illustrates a direct comparison of the anode current with the ion count rate for laser ionization of nickel. Saturation of the count rate is clearly seen, whereas the anode current shows no such effect.

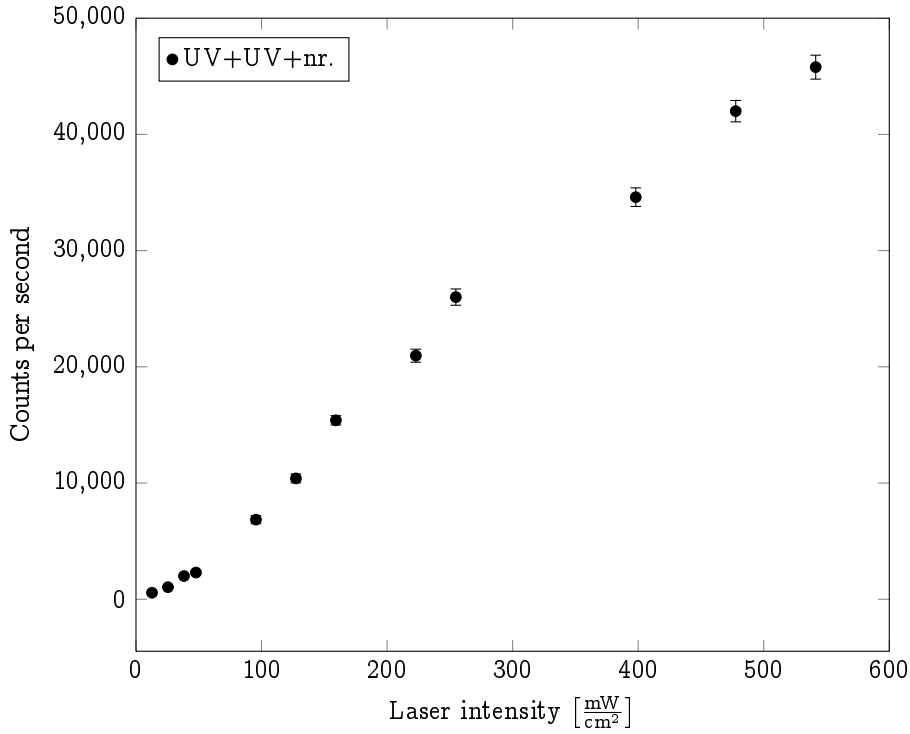

Figure 4.8. Count rate as a function of the UV laser intensity. The ionization takes place via two resonant steps from the silver ground state exciting electrons to a high-lying Rydberg state, which is then non-resonantly ionized. In order to reach the high ion count rates with this ionization scheme, the ABU was heated to much higher temperatures than in the measurements shown in Fig. 4.7.

Further tests in the future will be performed to check the reliability of the current readout method. Finally, we note that laser wavelength scans in the gas cell do not suffer from this effect as the time spread of the ion bunch is inherently relaxed. Meanwhile, for measurements performed in the vacuum environment of the ABU, the ion count rate for laser scans should be kept well below the saturation limit in order to avoid any artificial broadening.

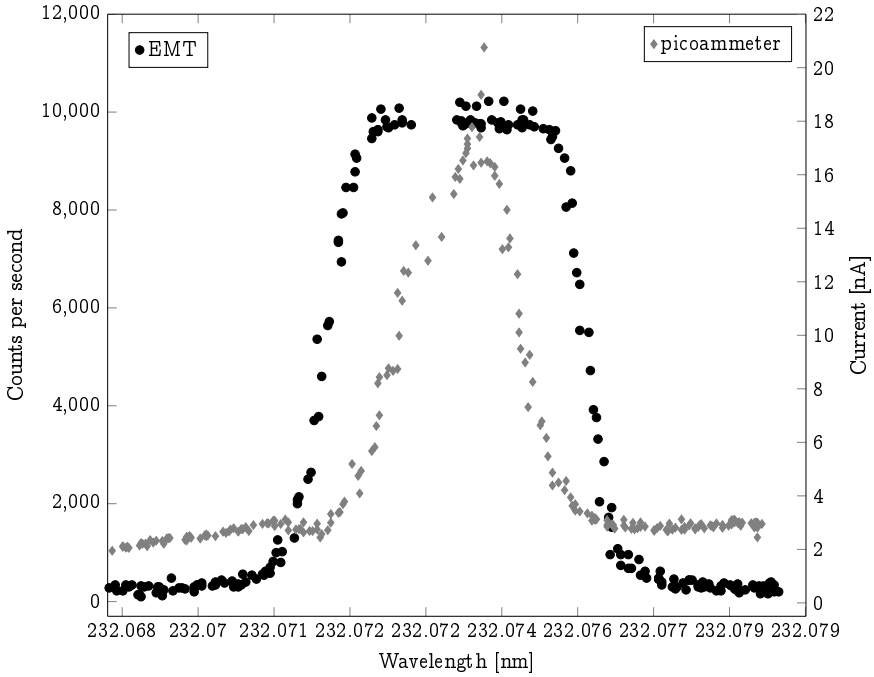

Figure 4.9. A comparison of the first resonant step laser wavelength scans for nickel recorded by ion counting and by measurement of the EMT anode current. The scans were performed in the atomic beam unit.

4.3.2. Wavelength calibration

For precise in-source laser spectroscopic studies the laser wavelength scanning and ion detection must be under reliable control. With the current Ti:sapphire system, high resolution wavelength selection over a scan region is performed by tilting the angle of the etalon using a computer-controlled precision rotation stage (operated by a PI m-232 linear actuator). During the scan, both the motor position and the wavelength readout are recorded along with the ion count rate. The accuracy of the wavemeter is modest, approximately ± 0.0001 nm , while the motor position is known accurately and can be very finely tuned with an actuator step size of 100 nm, less than the sensitivity of the wave meter.

Recording the motor position can be useful for smoothing out the fluctuations or discontinuities sometimes seen in the ion count rate versus wavelength scans. This

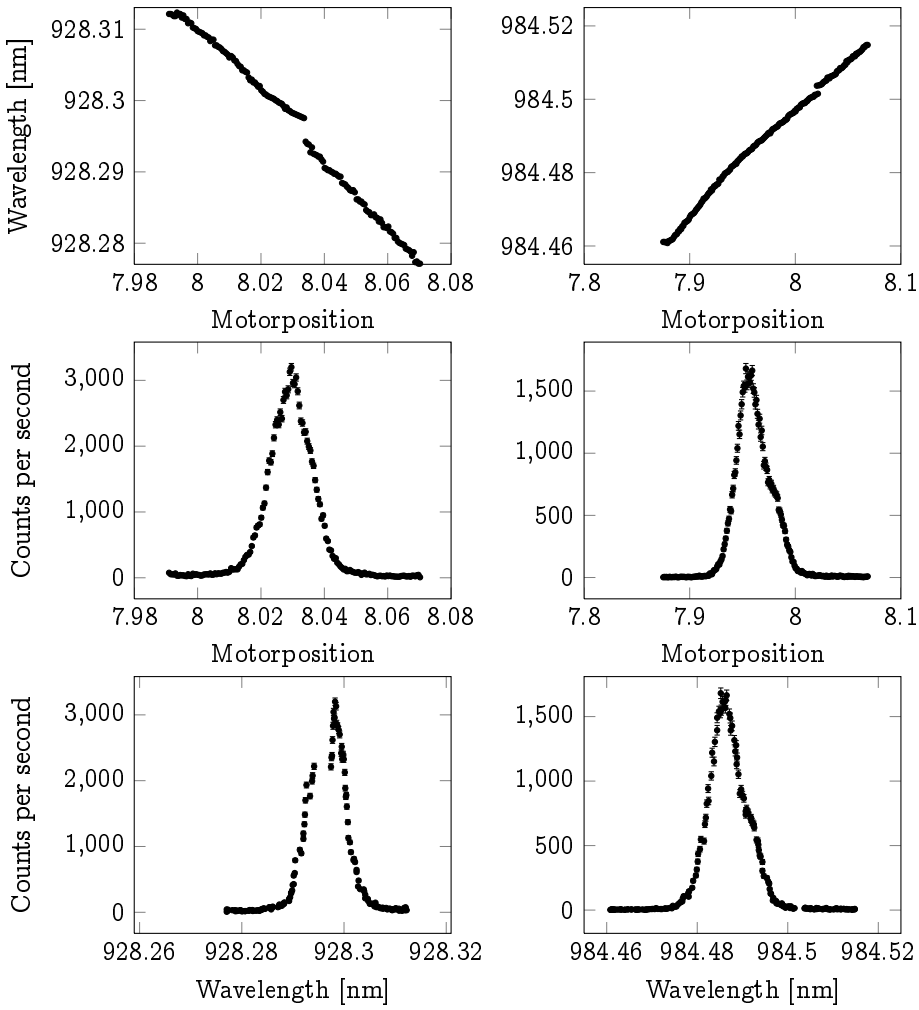

Figure 4.10. Laser scans performed in the ABU on nickel (left panels) and silver (right panels). The top panels illustrate the wavelength versus motor position, whereas the bottom panels show the ion count rate versus motor position and wavelength, respectively. Details of discontinuities in the structure are explained in the text. The fundamental wavelength is shown.

is done in practice by fitting a quadratic polynomial to a motor position versus wavelength dataset, which converts the precise motor position to a wavelength. The

exact cause of the discontinuities is not yet known. In many cases the discontinuity can be shifted to a location where it does not interfere with the data collection. Additionally, preliminary data utilizing the new IGISOL wavelength readout system, presented later, indicates a drastic reduction in the magnitude of the discontinuities in some cases. Other features, for example asymmetries in the resonance structure, may often indicate the presence of other states. Examples of both are presented in Fig. 4.10.

The data on the left panel are from scans performed on the nickel ground state transition at 232.0744 nm whereas the data on the right are from the silver ground state transition at 328.1624 nm. In the count rate versus wavelength spectrum of nickel (bottom left), a large discontinuity is visible at 928.296 nm which is not seen in the count rate versus motor position (centre left). Similarly, a break in the data is seen close to 984.502 nm in the silver count rate versus wavelength data (bottom right) which is not seen in the motor position data (centre right). As the silver ionization scheme utilizes a high-lying Rydberg state, an asymmetry is visible in the silver data both in the motor position as well as the wavelength scan at around 984.49 nm. The separation of the asymmetry peak and the main peak is of the order of 10 GHz, hence it is not caused by the hyperfine structure of silver [138]. Thus this represents the 328.1624 nm first resonant step laser directly populating the Rydberg states around 60945.434 cm^{-1} via the first excited state prior to non-resonant ionization. A more detailed study of this asymmetry would require a laser scan over the Rydberg state using a second laser.

In IGISOL-3 the wavelength readout was realised by using a glass plate to probe $\sim$4 % of the Ti:sapphire output. This secondary beam was further split in order to transport $\sim$96 % to a fast photodiode used to monitor the timing while the remainder was coupled into an optical fibre connected to a wavemeter. Each laser had a similar set of glass plates, and mechanical shutters were used to couple the different lasers to the single fibre.

Although this system worked reasonably well, it was cumbersome to use and prone to accidental misalignment. In order to increase the reliability, a new readout device was developed based on an existing Mainz design. Each laser is coupled into a specific fibre which in turn is connected to a commercial fibre switcher (Sercalo SW1x4-62N-07-17) that enables computer controlled fibre selection. Before reaching the switcher, the optical fibres are split in two using a 50:50 fibre splitter (Sercalo FUSED-12-IRVIS-62.5/125-50/50-FCPC-1-1) which enables parallel access to a convenient laser pulse timing measurement. The general idea of the fibre switching and timing unit for a single Ti:sapphire is presented in Fig. 4.11 and the full schematics can be found

in the Appendix in Fig. B.2 along with a photograph of the unit in Fig. B.3.

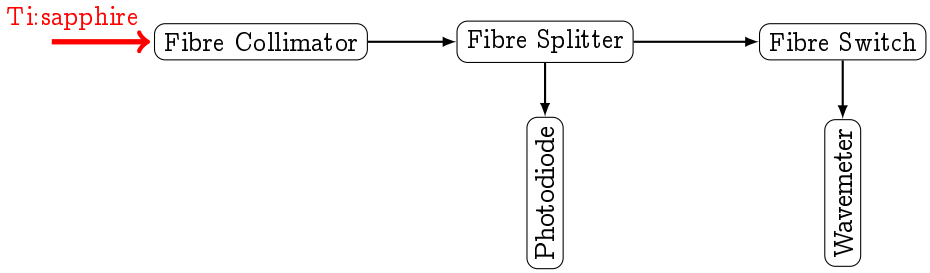

Figure 4.11. General idea for the new wavelength readout

4.4. Shadow gas cell

Though standard ion guides can be utilized for resonance laser ionization under off-line conditions, their performance deteriorates under on-line conditions due to recombination effects [139]. The reason for this was linked to the direct line of sight between the primary beam and the ionization region which allowed laser ions to survive only if they were created near the nozzle region. A solution for the problem was presented by the LISOL group in a novel gas cell design with separated stopping and ionization regions [119] (see Fig. 4.13). These two chambers are connected via a 10 mm channel in such a way that the primary beam has no direct line of sight into the ionization chamber. While the gas cell can be used in a standard ion guide mode, in the primary mode of operation the reaction products are allowed to neutralize and are subsequently resonantly re-ionized in the ionization chamber. The targets in the shadow gas cell are mounted on a inset placed within the stopping chamber typically resulting in a stopping volume of ~ 28 cm^3 while the ionization chamber volume ranges from $\sim$3 to 4 cm^3.

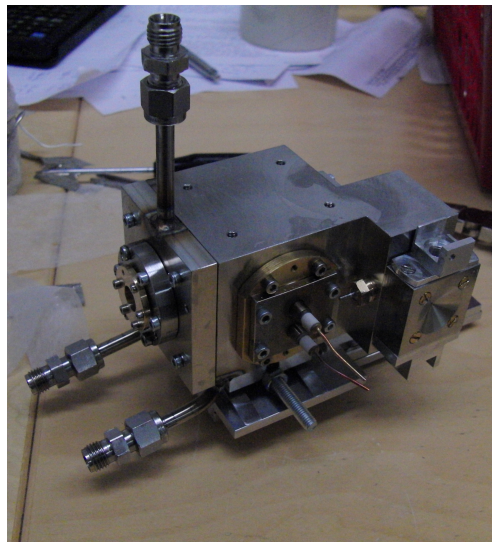

Figure 4.12. A photo of the shadow gas cell.

Besides the ion guide geometry, the so-called shadow gas cell utilises a set of electrodes inside the ionization region. This ion collector is used to suppress the non-neutral fraction in order to improve the selectivity of the resonance ionization pro-

cess. Furthermore, the ionization chamber can be fitted with an additional extension after the ion collector which enables transversal ionization next to the exit nozzle. A similar ion guide has been recently constructed at IGISOL (see Figs. 4.12 and 4.13) based on the LISOL design. The performance of the ion guide has been tested at IGISOL-4 with nickel atoms evaporated from a hot filament, an α -recoil source and in the presence of a 30 MeV $^{4}He^{2+}$ primary beam that was used to simulate on-line conditions.

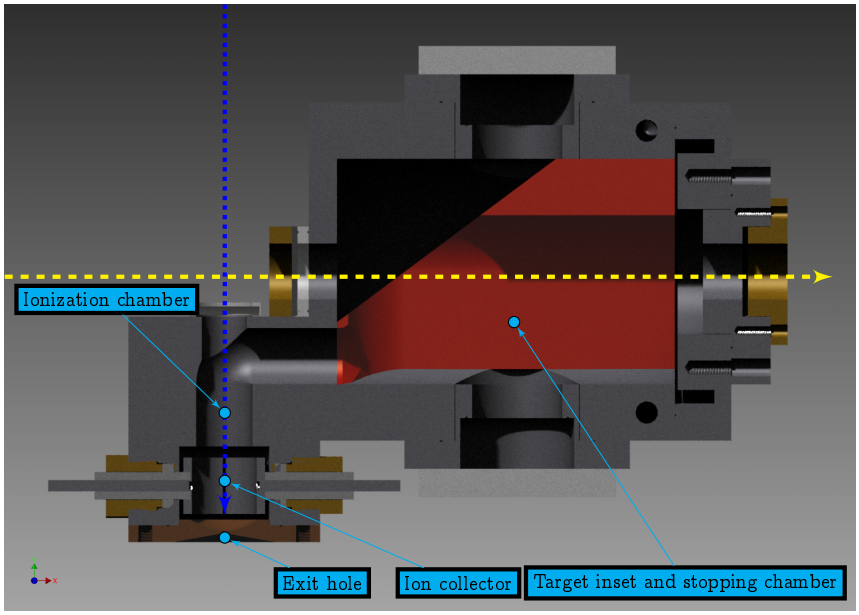

Figure 4.13. A technical view of the gas cell. Laser (blue) enter the shadow gas cell in a longitudinal geometry. The yellow line represents the primary beam axis.

4.4.1. Alpha recoil source

The efficiency of an ion guide is a fundamentally important parameter that is needed in the estimation of the production yield of radioactive isotopes. A standard method of determining ion guide efficiencies at IGISOL under a low plasma density is to use a radioactive ^{223}Ra α -recoil source ($T_{1/2}$=11.4 d). The radioactive decay chain for ^{223}Ra is shown in Fig. 4.14. As ^{223}Ra α-decays, either the daughter ^{219}Rn ($T_{1/2}$ = 3.96 s) or the α -particle recoils from the source. A ^{223}Ra source placed

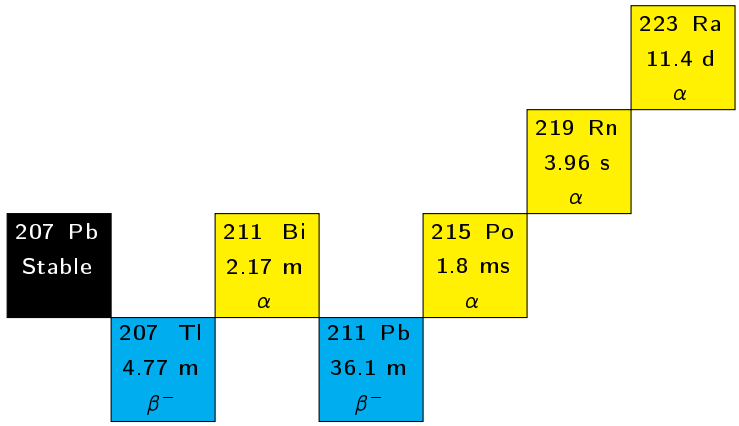

Figure 4.14. The decay chain for ^{223} Ra.

within an ion guide can be used to study the efficiency ϵ_{ig} by comparing the activity of the source ($A_s(^{223}\mathrm{Ra})$) to the extracted daughter activity ($A_s(^{219}\mathrm{Rn})$):

$$\epsilon_{ig} = \frac{A_s(^{219}\mathrm{Rn})}{A_s(^{223}\mathrm{Ra})}. \tag{4.1}$$

The original activity of the source may be calculated as follows:

$$A_s(^{223}\mathrm{Ra}) = \frac{\mathrm{N}\left(^{223}\mathrm{Ra}_\alpha\right)}{\mathrm{b.r.}\left(^{223}\mathrm{Ra}_\alpha\right) \times \Omega \times T}, \tag{4.2}$$

where $\mathrm{N}\left(^{223}\mathrm{Ra}_\alpha\right)$ is the measured number of α -counts, $\mathrm{b.r.}\left(^{223}\mathrm{Ra}_\alpha\right)$ is the branching ratio of the α-channel, T is the measurement time and Ω is the solid angle. The activity $A_s(^{223}\mathrm{Ra})$ corresponds directly to the number of ^{219}Rn recoils $\mathrm{N}(^{219}\mathrm{Rn})$.

Similarly, the activity of the source can be determined using the decay of the daughter,^{219}Rn. By counting the decays ($\mathrm{N}\left(^{219}\mathrm{Rn}_\alpha\right)$) in a channel ($\mathrm{b.r.}\left(^{219}\mathrm{Rn}_\alpha\right)$) and using Eq. 4.2, gives the source activity $A_s(^{219}\mathrm{Rn})$.

The activity of the ^{223}Ra source was measured using a 300 mm^2 silicon detector placed 292 mm from the source (solid angle Ω=$2.80(1) \cdot 10^{-4}$). The source intensity was determined from the Ra_2 peak shown in Fig. 4.16. All peaks in Fig. 4.16 were fitted simultaneously with a function that combines a Gaussian profile with an

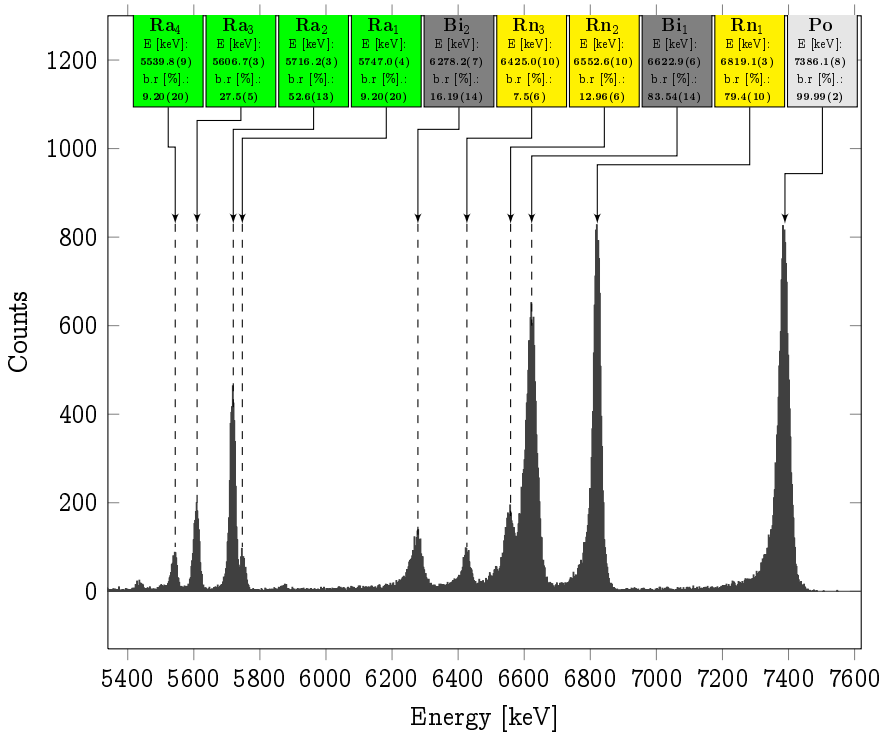

Figure 4.15. The α decay spectrum for the ^{223} Ra decay chain with energies and branching ratios. The spectrum was collected for 3000 s.

exponential term to account for the low energy tail of the peak:

$$f(x) = \begin{cases} I \times e^{\frac{\Delta x}{2}\left(\frac{2(x-x_0)+\Delta x}{s^2}\right)} & : x < x_0 - \Delta x \\ I \times e^{-\frac{1}{2}\cdot\left(\frac{x-x_0}{s}\right)^2} & : x \geqslant x_0 - \Delta x \end{cases}, \tag{4.3}$$

where I is the peak intensity, Δx is the distance between the Gaussian peak maximum x_0 and the boundary of the Gaussian and exponential, and s is the standard deviation of the Gaussian. If one uses a Gaussian function alone to extract the peak intensity, an underestimation of counts at the low energy side would be observed. The general form of such a peak shape function is from Ref. [140] while the explicit equation used in the fitting is from the PhD. thesis of M. Ranjan [141], in which the α -recoil source was used in the determination of the efficiency of a cryogenic gas catcher.

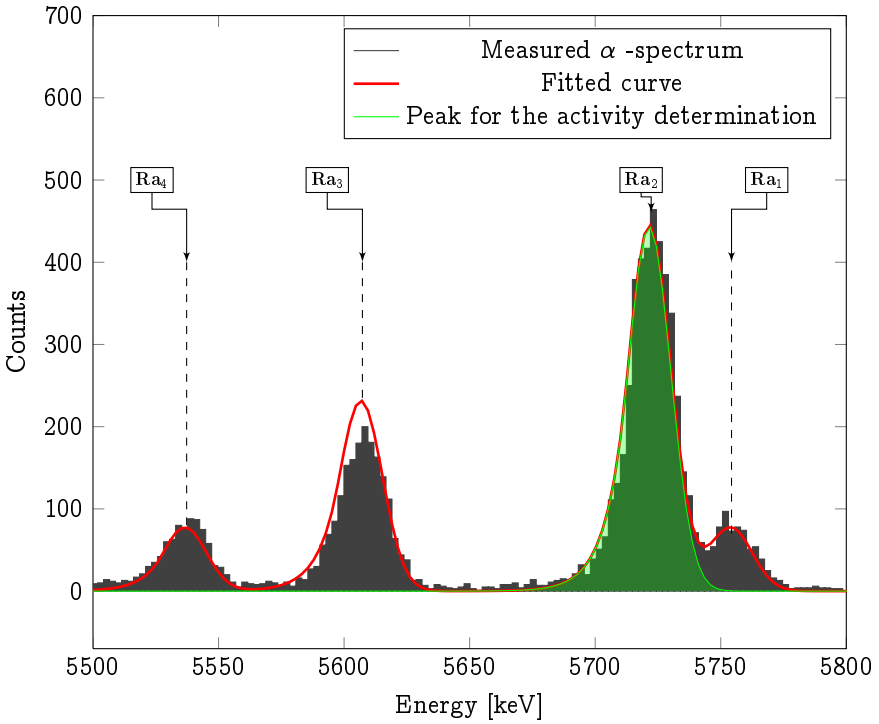

Figure 4.16. The α-decay spectrum for ^{223}Ra. The spectrum was fitted with Eq. 4.3 and the peak used for calibration is shown in green (Ra_2). The notation follows that given in Fig. 4.15.

The peak fitting was done in Mathematica 8.0 [142], where a sum function was created from Eq. 4.3 to account for the four most intense decay channels in the spectrum. The peak intensity I was replaced with $I = b.r \times I'$, to allow the peaks to be fitted with a shared intensity I' multiplied by the branching ratio of the decay channel ($b.r.$). By further assuming that the peak shape parameters Δx and s were identical for α -lines from the decay of the same isotope, the number of fit parameters could be reduced to 7.

Using χ^2 -minimization to fit the sum function to the spectrum allowed the area of the Ra_2 -peak to be determined by numerically integrating Eq. 4.3, hence yielding N $\left(^{223}Ra_\alpha\right)$ needed for the activity determination. Finally, Eq. 4.2 yielded the source

activity as

$$A_s(^{223}\mathrm{Ra}) = \frac{4223.86}{0.526 \times 2.8 \cdot^{-7} \times 3000\ \mathrm{s}} = 9560\ \mathrm{Bq}. \tag{4.4}$$

with an error of about 4.2 %.

Following the activity determination the source was installed into the shadow gas cell and the measurement was repeated utilizing the α-decay of the ^{219}Rn recoils. The recoils were detected after the ions had been extracted from the ion guide, accelerated to 30 keV and implanted directly onto the surface of a silicon detector before the mass separator. Figure 4.17 presents the α -decay spectrum for ^{219}Rn.

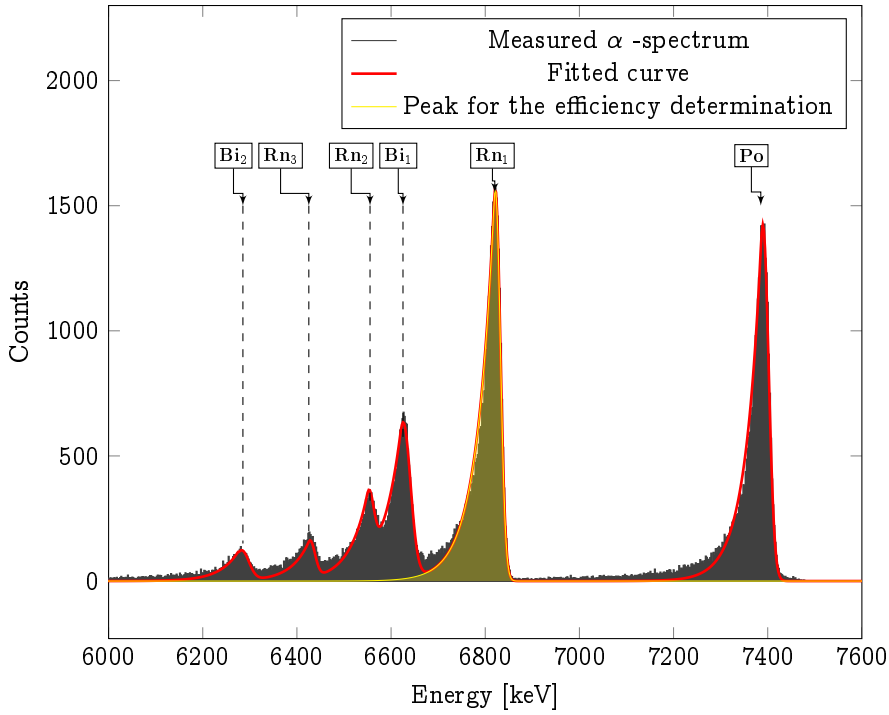

Figure 4.17. An example of an α -decay spectrum for ^{219}Ra measured with the recoil source at position B1 in the shadow gas cell with the target inset (see Fig. 4.18). The peak fit used for the efficiency determination is shown in yellow. The notation of the peak labels follows that given in Fig. 4.15.

As with the activity determination, the spectrum was fitted simultaneously such that peak shape parameters and intensities were shared on an element basis leading

to a total of 15 fit parameters. The integral over the Rn_1 peak then yielded the number of events (N $(^{219}Rn_\alpha)$) in the decay hence enabling the determination of the activity $A_s(^{219}Rn)$ using the known branching ratio of 79.4 %, and a silicon detector acceptance of 0.5. The total efficiency of the ion guide can then be determined with Eq. 4.1.

The efficiency of the ion guide was probed at different source locations, depicted in Fig. 4.18. The ionization chamber of the shadow gas cell was studied in three locations, A1, A2 and A3, along the axis, and the reaction chamber in two locations, B1 and B2, perpendicular to the primary beam axis. Additionally, the efficiency in B2 was measured without the target inset.

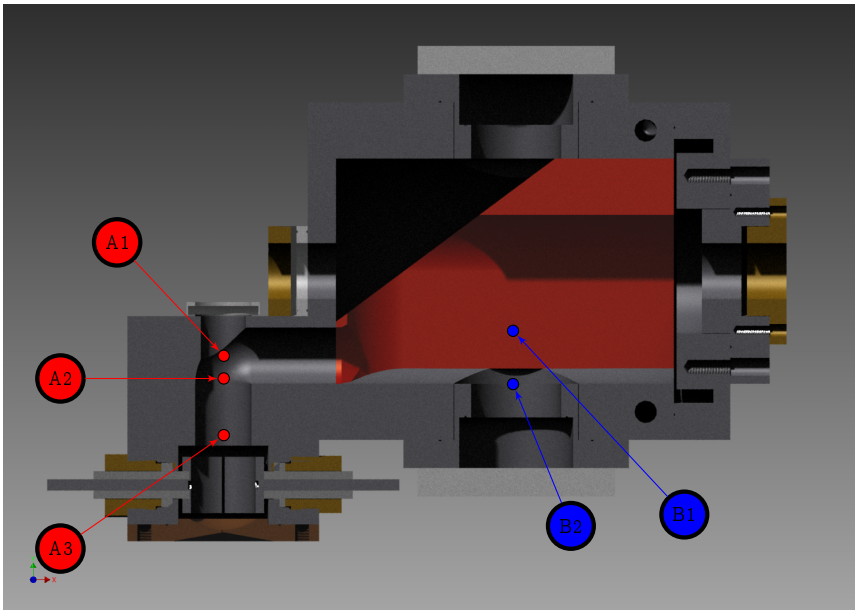

Figure 4.18. The source locations within the ion guide used for the efficiency determination. Distance from the exit hole: A1≅30 mm, A2≅27 mm and A3≅19 mm. Distance from the chamber wall: B1≅10 mm and B≅20 mm.

As seen in Table 4.1, the efficiency of the shadow gas cell depends strongly in which chamber the source was located. The efficiencies in the ionization chamber are between 10 - 20 %, however the transport efficiency from the stopping chamber drops by a factor of approximately ten, as long as the source is far from the chamber wall.

Table 4.1. Transport efficiencies ϵ_{ig} for the shadow gas cell measured in positions depicted in Fig. 4.18.

Source position	ϵ_{ig} [%]
A1	11.4 ± 0.2
A2	16.1 ± 0.3
A3	17.1 ± 0.3
B1	2.3 ± 0.1
B1 [No Inset]	0.9 ±0.03
B2	0.1 ± 0.01

Ions created close to the chamber walls (B2) suffer from a low gas flow velocity and diffusion losses. Another notable difference results from the target inset. With the inset, the efficiency at B1 is 2.3 % but when the inset is removed, the efficiency drops to 0.8 %. A reason for the difference in efficiency with and without the target inset may be found in the gas flow simulations performed by T. Sonoda. Examples of simulations are shown in Fig. 4.19, where a clear region of turbulence is seen in the centre of the stopping chamber without the inset. The reduction in gas flow from this chamber supports the experimental data which shows a drop in the gas cell efficiency.

4.4.2. Pseudo on-line run

The shadow gas cell allows for efficient laser ionization under on-line conditions as has been seen at LISOL. In order to test this at IGISOL, a resistively heated nickel filament was placed within the gas cell to act as a source of nickel atoms. A 30 MeV $^{4}He^{2+}$ primary beam from the K-130 cyclotron passed through the stopping chamber to create a plasma. The gas cell was fitted with a 0.5 mm exit nozzle in order to increase the evacuation time thus to encourage the ions created within the stopping chamber to neutralize. During the optimization of the mass separator while the primary beam was on, it was observed that resonantly ionized nickel was being extracted from the ion guide even when the filament was not heated. This was traced to the nickel windows used in the gas cell. Nickel atoms/ions were ejected from the window by the passage of the primary beam hence effectively creating a quasi-on-line condition. Fig. 4.20 presents laser wavelength scans performed on first excitation transition at 232.0744 nm. The two most abundant isotopes of nickel are shown, ^{58}Ni (74 %) and ^{60}Ni (26 %), following detection of the ions after selection

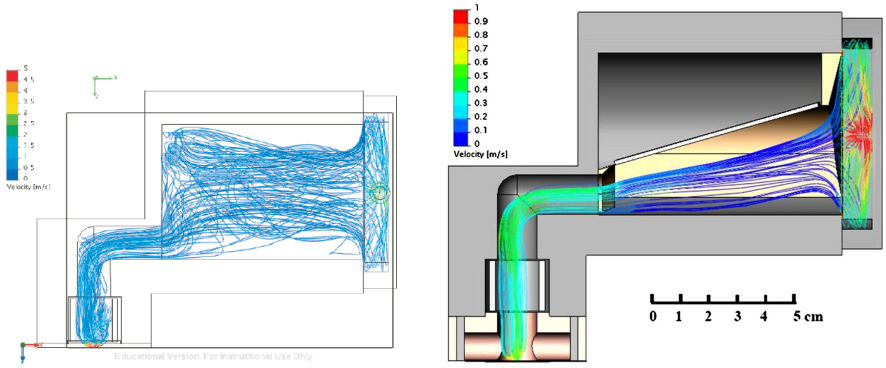

(a) Gas flow within the shadow gas cell without the target inset. Figure courtesy of T. Sonoda.

(b) Gas flow within the shadow gas with a target inset. Figure from Kudryavtsev *et al.* [119].

Figure 4.19. Gas flow within the shadow gas cell with and without the target inset. Though the target inset shown on the rigth is different from that used at IGISOL, the simulations support the experimental results.

with the dipole magnet. This measurement can be considered as a proof of concept for resonance ionization in a gas cell under on-line conditions.

Following continuous heating of the filament, Fig. 4.21a shows the ion signal time profile when laser ionization takes place in helium gas at 180 mbar. The lasers are introduced through the quartz window along the extraction axis of the gas cell. Mechanical shutters (discussed in Ref. [123]) allow the laser radiation to be switched on at t=400 ms and off at t=1000 ms. An exponential growth curve fitted to the $^{58}Ni^{+}$ data results in a value of τ=35.6(1). This characteristic saturation time reflects the combination of the survival time of Ni^{+} against losses due to molecular formation and extraction from the ion guide. Using the conductance of a 0.5 mm exit hole for helium (122 cm^3/s), the saturation time can be converted into an effective volume for laser ionization of $\sim$4.4 cm^3. We note that the volume of the ionization chamber of the shadow gas cell is $\sim$4 cm^3 hence the saturation time is dominated by ion extraction and the effect of molecular formation is negligible. The opposite scenario, when molecular formation dominates, is presented in [123].

Figure 4.21b represents the $^{58}Ni^{+}$ time profile under pseudo on-line condition. The filament was turned off and nickel atoms were knocked from the window by the primary He beam. Additionally, the transversal ionization extension was added to the ion guide in order to increase the ionization volume after the ion collectors. The

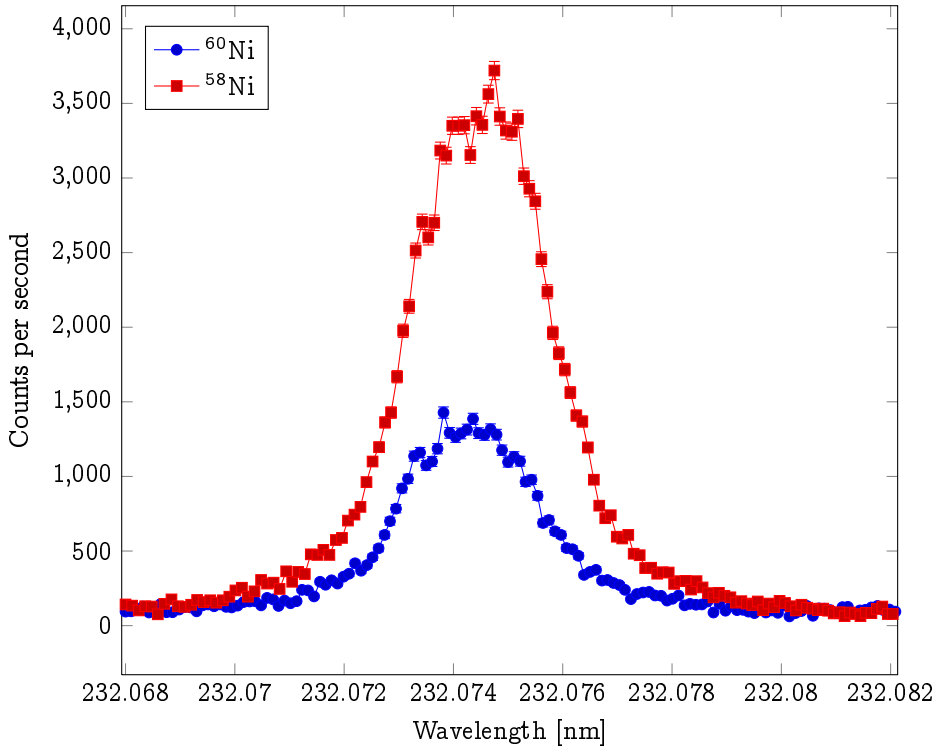

Figure 4.20. Wavelength scans for the ground state transition for ^{58,60}Ni. The nickel atoms were ejected from the gas cell entrance window due to the passage of the $^{4}He^{2+}$ primary beam.

lasers were off and therefore the time profile corresponds to the ions that survive neutralization within the gas cell. The primary beam was turned on at t=200 ms and off at t=1000 ms. There is a delay of ∼16 ms before the first ions exit the gas cell, rising to a peak ∼90 ms after beam has been turned on. The peaks visible in the figure have been discussed extensively in the context of laser ionization studies of yttrium [124] where a different gas cell geometry was used. A complex process of competing ion creation and loss mechanisms, and/or a plasma generated electric field are possible explanations for the features seen in the $^{58}Ni^{+}$ time profile.

An important feature of the dual chamber gas cell is the ion collector. As highlighted earlier, the ability to collect non-neutralised ions that come from the stopping chamber is a useful method to dramatically improve the selectivity. Although the so-called

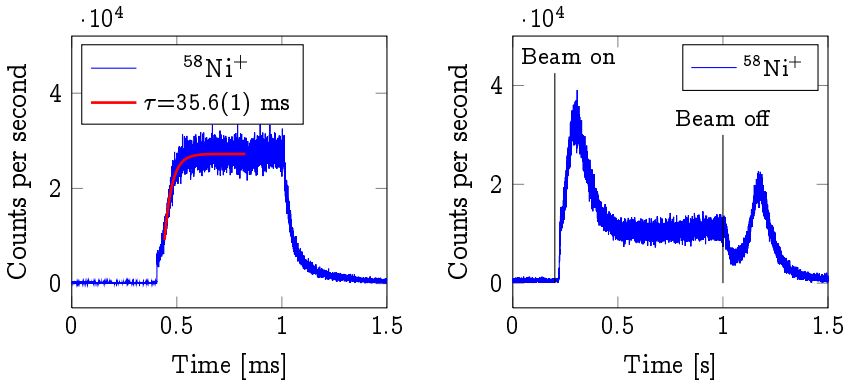

(a) Rise time τ of the laser ion signal from the SGC when pulsing the lasers.

(b) Ion signal under the primary He beam pulsing.

Figure 4.21. Time evolution of the signal extracted from the SGC under laser and primary beam pulsing

LIST approach, discussed in Chapter five, can be used to improve the selectivity, Article **I** illustrates the relatively high ion suppression voltages required. The design of the dual chamber allows the use of electric fields for ion purification in the laser-ionization chamber, and has been successfully demonstrated at LISOL [119].

As seen in Fig. 4.18, the ion collectors sit just behind the exit hole of the ion guide. However, the transversal laser ionization extension may be added such that the electrodes are located further upstream, collecting the ions from the stopping chamber without affecting the laser-produced ions.

The ion collector was first tested in combination with the nickel filament and utilizing the extension. Fig. 4.22 presents the effect of applying bias voltage pulses on the collector in the presence of continuous longitudinal laser ionization of filament produced ions. Voltage pulse of different polarity with equal amplitude was applied to the opposite electrodes. The pulse was applied from t=400 ms to t=1000 ms, and the given percentage illustrates the collected ion fraction with respect to the lasers blocked.

Figure 4.23 presents the effect of the ion collector in the presence of the primary beam $^4He^{2+}$ and the heated nickel filament. The primary beam is turned on at t=100 ms and off at t=700 ms. The lasers are turned on at t=500 ms and off at t=1.2 s. The total cycle time was 1.8 s. The mass separator was tuned to A/q=60 in

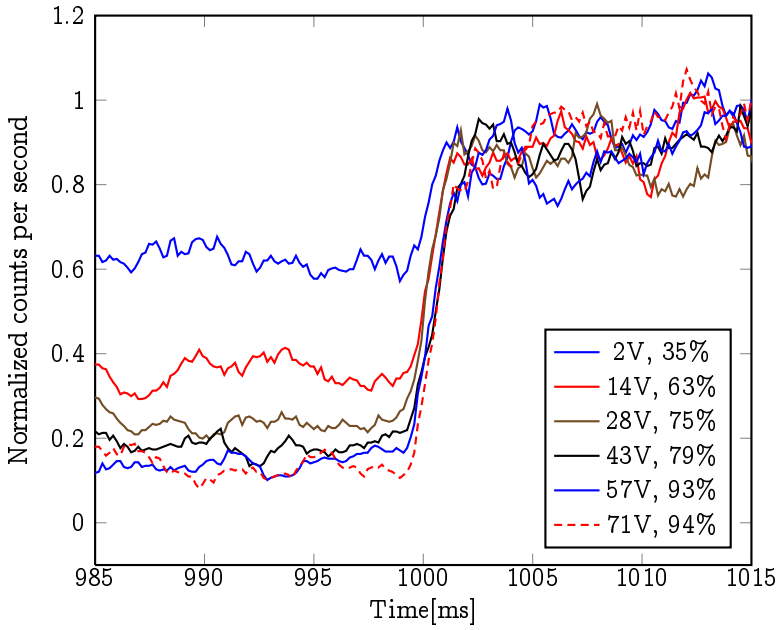

Figure 4.22. The effect of the ion collector voltage on the count rate. The non-zero signal during ion-collector off is due to lasers ionization after the ion collector.

order to select $^{60}Ni^{+}$. The solid blue line illustrates the ion signal with the collector off, the red line with the collector on.

First, it can be seen that the effect of the primary beam without the lasers is rather small (500 counts per second) with a delay of ~25 ms before the first ions reach the exit hole. This background is completely suppressed after the ion collector is turned on. When the lasers are turned on at t=500 ms the $^{60}Ni^{+}$ signal increases rapidly. The effect of the primary beam can be seen more clearly when it is turned off at t=700 ms. The ion count rate slowly reduces from an equilibrium value of 26000 s^{-1} to 21000 s^{-1}, resulting from the removal of a production mechanism for nickel atoms, either from the ejection of the window material or decomposition of molecules. A similar effect has been reported for yttrium in Ref. [124], albeit the time-scales were rather different reflecting the different ion guide geometries used in this work. During the laser on period the ion collector has a limited effect as a considerable nickel fraction is laser ionized in the extension volume downstream from the collector. The shadow gas cell clearly works as intended as the primary

beam is screened from the ionization region of the gas cell.

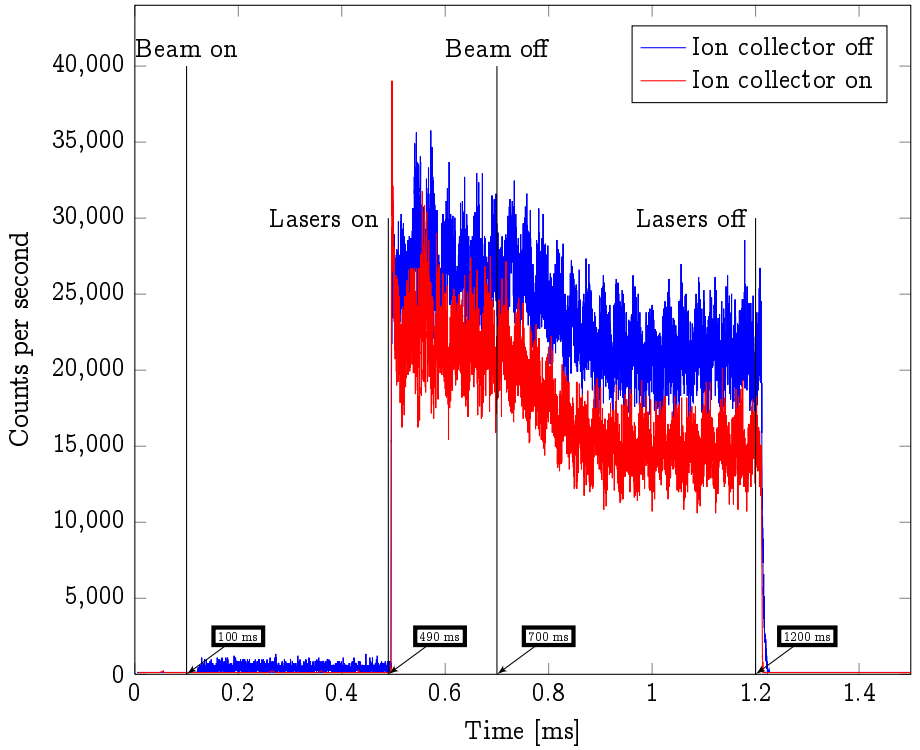

Figure 4.23. Combined beam on-off and laser on-off spectrum for mass separated ^{60}Ni measured in helium buffer gas. The nickel atoms were constantly evaporated from the hot filament. The 30 Hz fluctuation in the spectrum is artificial noise from the electronics.

4.5. Development of analysis software for FURIOS

Reliable data analysis is imperative for the extraction of unambiguous nuclear structure information from experiments. This section briefly introduces a computer program developed for the analysis of optical spectroscopy data, to be used in combination with the future high resolution laser system under development at FURIOS.

The program has been written in C++/C/Qt due the need for fast code, better Qt - C++ integration and tool kit availability. The program utilizes Gnu Scientific

library (GLS) for data fitting and to provide mathematical functions. A small part of the code is presented in Appendix D.1 demonstrating the Lorentzian lineshape fitter. The full code is available at `http://gitorious.org/hfs/hfs` under GNU General Public License (GPL) license.

4.5.1. Hyperfine spectrum analysis

The program has been developed for analysis of hyperfine spectra. It analyzes the data by fitting a calculated spectrum profile to the experimental data using the Levenberg-Marquardt algorithm (LMA). The fit procedure yields the A and B hyperfine factors related to the peak spacing which contain the relevant nuclear structure information. The program can fit standard Gaussian and Lorentzian line shapes as well as an analytical approximation of the Voigt profile [143, 144] presented by Mclean *et al.* [145].

The following describes in simple terms the general procedure for the calculation of the hyperfine spectrum. Firstly, the allowed hyperfine transition frequencies are calculated using [146]:

$$\Delta\nu = A \underbrace{\frac{C}{2}}_{\alpha} + B \underbrace{\frac{(3C(C+1) - 4I(I+1)J(J+1))}{(8I(2I-1)J(2J-1)}}_{\beta} \tag{4.5}$$

in which I is the nuclear spin, J is the spin of the atomic state, A and B are the hyperfine structure parameters and $C = (F(F+1) - I(I+1) - J(J+1))$, where F is the spin of the hyperfine level. Eq. 4.5 is calculated for all allowed F-state transitions which follow the selection rule $\Delta F = 1, 0$ for which $F_{\text{lower}} \neq 0$. The F-states for the lower and upper J-state are calculated as $\mid (J-I) \mid < F < (J+I)$ if the J states fulfil the condition $\Delta J = 0, 1$ and $J_{lower,upper} \neq 0$. Furthermore, the program calculates the relative transition intensities for the allowed transitions. The details of the mathematics involved are presented in Ref. [147].

Figure 4.24 presents the main user interface showing an example of calculated and experimental data for ^{93}Nb ($I = 9/2$) obtained using collinear laser spectroscopy at IGISOL. The spectroscopy was performed on the 290.9 nm 2357 cm^{-1} 5s^{5}F$_1$ $\rightarrow$ 36732 cm^{-1} 5p^{5}F$_1$ line [114]. The table in the bottom displays the individual hyperfine transitions in rows and the columns display the F-spin, and the α and β terms of Eq. 4.5 for both the upper and lower F-state. In addition the transition intensities are calculated both for isotropic fluorescence distribution and at a 90°

angle for each transition. In this example, a Voigt spectral lineshape was used with a Lorentzian width of 20 MHz, a Gaussian width of 20 MHz, an arbitrary intensity of 5000 and an offset of -1020 MHz as the initial values.

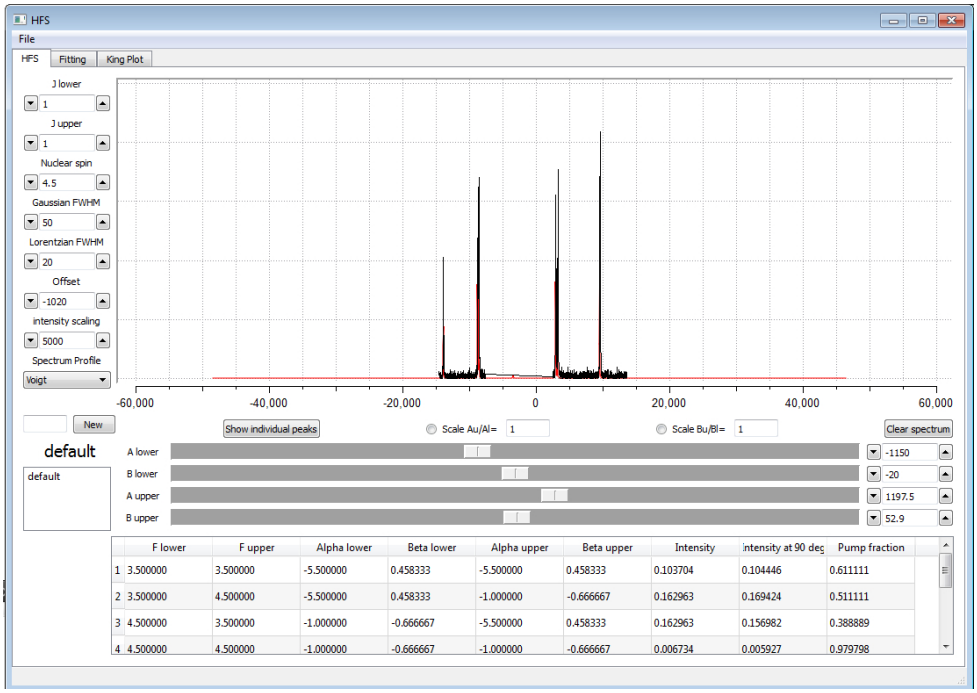

Figure 4.24. The main user interface for the program showing the calculated (red) and measured spectrum (black) for ^{93}Nb. Experimental spectrum courtesy of B. Cheal.

Adjusting the A and B hyperfine parameters to match the experimental spectrum provides the initial values for the minimization routine that uses the LMA. With suitable input values the fitting routine converges to a χ^2 minimum by varying the given parameters, namely A and B for both upper and lower states, the center of gravity $X0$, the y-offset Y, the Lorentzian and Gaussian widths of the line wl and wg, and the intensity. The C++ implementation of the Voigt function is presented in Appendix D.2. Figure 4.25 shows the minimization interface with a fit of experimental data of the ^{93}Nb spectrum. During the minimization procedure all parameters were kept free.

The values for upper level $A_u = 1198.0(1)$ MHz and $B_u = 59.5(4)$ MHz parameters

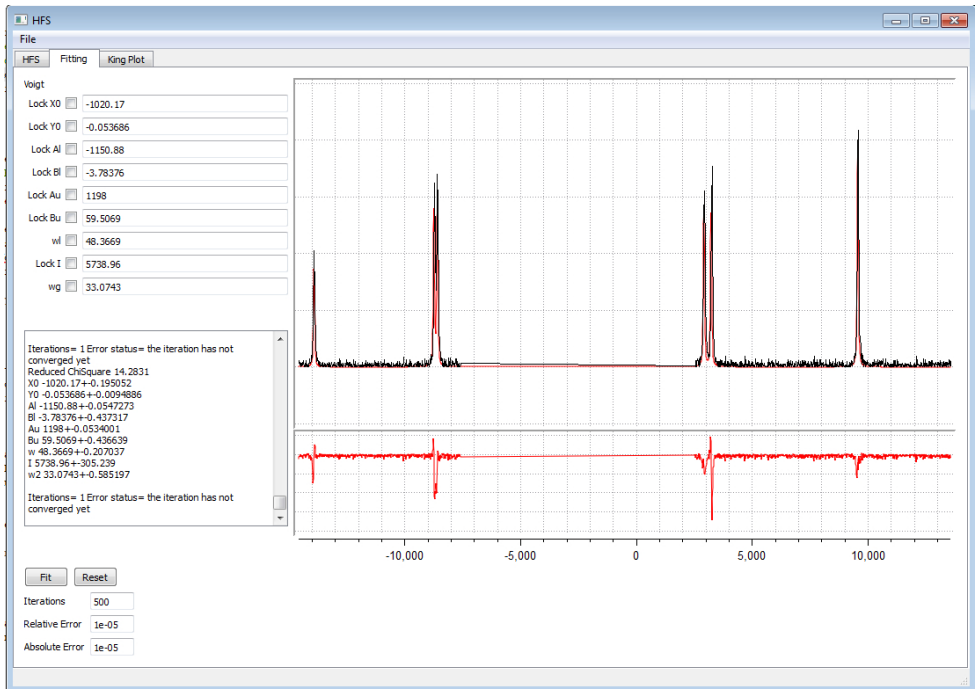

Figure 4.25. The fitting tab of the program showing the experimental data (black) and the resulting fit to the data (red).

can be compared to those of Cheal *et al.* in Ref. [114]. In that work A_u=1197.5(2) MHz and B_u= 52.9(8) MHz. Though the A_u -parameter extracted here is in close agreement, the B_u -parameter differs considerably. The discrepancy may arise from the program being unable to properly account for a split spectrum, or from the fitting procedure in which all the parameters were kept free. In the work of Cheal *et al.* the lower state values were constrained to match the atomic ratios observed in ^{93}Nb. This feature is currently unavailable in the analysis program.

4.5.2. Linear regression

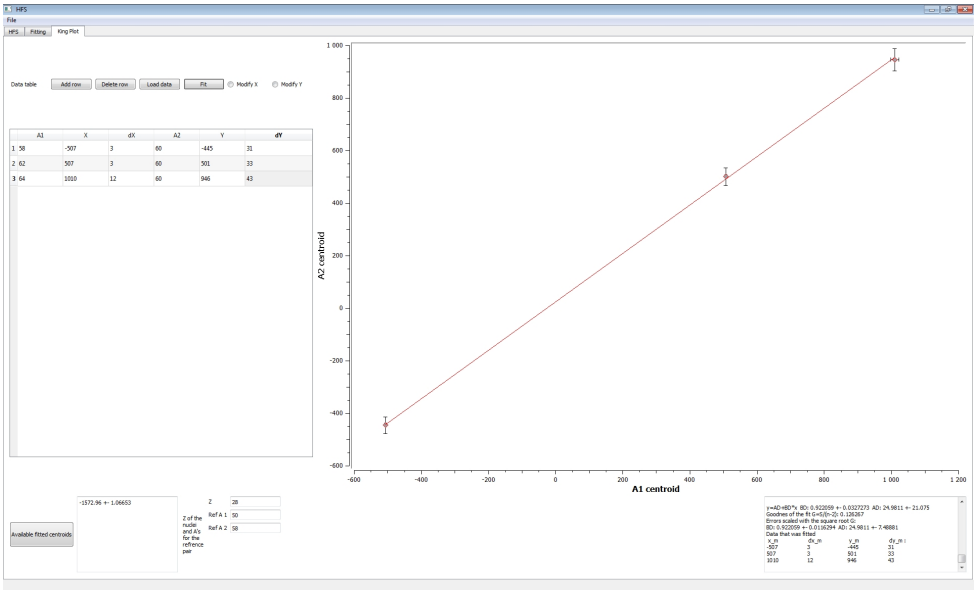

Figure 4.26. The King plot tab of the program displaying the unmodified data from Article **I** and data by Steudel *et al.* [148] plotted and fitted with general Deming regression of an straight line using the York method.

The King plot method [149] is a tool for extracting nuclear information from isotope shift data. The measured isotope shift is a combination of a field shift and a mass shift which are a result of the finite mass and the non-zero volume of the nucleus respectively. If the mass shift is known for one transition, the King plot method can relate it to the mass shift of an other transition. In order to analyze isotope shift data where both variables have associated errors, a standard linear fit is no longer

sufficient to extract reliable data. In order to take into the account errors correctly, a so-called errors in variables method needs to be used. The program utilizes Deming regression and specifically a method by York *et al* for a general-errors-in-variables regression of straight lines [150].

Fig. 4.26 presents the King plot module of the program and the nickel isotope shift data measured at IGISOL (Article **I**) plotted against the data by Steudel [148] obtained from Ni I. The resulting fit parameters are presented in Table 4.2 along with a standard linear regression for comparison. Though the values given by the two fit procedures differ only slightly, the errors utilizing the variables method have been correctly taken into account.

Table 4.2. Comparison between standard linear regression and errors in variables regression.

y=A+B*x			
Errors in variables		Linear regression	
A: 0.922059	±0.0116294	A: 0.91926 ±	0.0119
B: 24.9811	±7.48881	B: 24.51744	±8.50808

5. In-gas-jet laser ionization - the LIST approach

Resonance laser ionization spectroscopy is feasible in a gas cell however the buffer gas in the ion guide can affect the line shapes and transition centroids of atomic transitions via pressure broadening and pressure shift. Such detrimental effects to the spectral resolution limits the successful study of the atomic properties of elements with small hyperfine splitting and/or high sensitivity to atomic collisions. A novel approach to addresses such limitations is in-gas-jet laser ionization.

Recently, a method was proposed which could allow for very high selectivity and beam quality from an hot cavity ion source [151]. The method decouples the diffusion and ionization regions of the source by utilizing a multipole ion trap. The high selectivity is achieved by repelling all non-resonant ions while allowing neutral species into the ionization region. The neutral atoms are resonantly ionized by counter propagating laser beams and subsequently trapped in the potential created by the multipole structure. The method, namely Laser Ion Source Trap (LIST) approach, has since been adapted to ion guides [152–154]. The approach has been demonstrated at both IGISOL [128] and LISOL [154] facilities, however its efficiency requires considerable improvement. This chapter presents development work towards increasing the efficiency of the LIST method via the shaping of a supersonic jet emitted from an ion guide.

An exploratory study of gas jets was made at IGISOL in the 1990's by Rasi *et al.* In that work the gas jets were visualized by exciting metastable states in the buffer gas with electric discharge [155]. In this thesis the visual observation, digital photography and subsequent computer analysis [156] of the afterglow from the relaxation of excited states in argon or helium atoms [157] is used to study the effect of different parameters on the jet shape. Although the method can yield detailed information of gas intensity distribution, it presents only a qualitative picture. For more quantitative information, *Raman* spectroscopy may be used to directly map the temperature and density in supersonic flow [158].

In this work the measurements were performed in a test and development platform, part of which is illustrated in Fig. 5.1. The results have been published in Article **II**, "Gas jet studies towards an optimization of the IGISOL LIST method" [159]. In

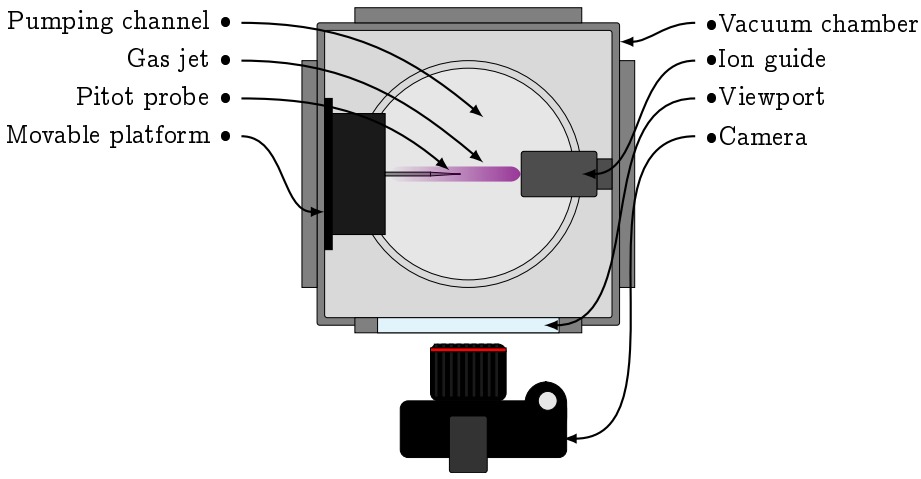

Figure 5.1. Schematic representation of the test set-up for the gas jet development.

the article, gas jets emitted from an ion guide were studied as a function of nozzle type and gas cell-to-background pressure ratio in order to obtain a low divergent, uniform jet over a distance of several cm. For a simple exit hole or converging-diverging nozzle, the jet diameter was found to be insensitive to the nozzle shape and inlet pressure. Sonic jets with a FWHM below 6 mm were achieved with a background pressure larger than 1 mbar in the expansion chamber. The measurements were supported by the detection of radioactive ^{219}Rn recoils from an alpha recoil source mounted within the gas cell. A de Laval nozzle was found to produce a well-collimated supersonic jet at low background pressures with a FWHM of $\sim$ 6 mm over a distance of 14 cm. Direct Pitot probe measurements revealed a non-uniform pressure distribution in the gas jet axis of the Laval nozzle, supporting the visual observations. Additionally, computational fluid dynamics gas flow simulations were initiated to guide the future development of the gas jet nozzles.

The measurements and nozzle development presented in the article and in the following section were motivated by the requirement of a good geometrical overlap between atoms and counter-propagating laser beams in the gas cell-based Laser Ion Source Trap (LIST) project. The requirement arises from the gas jet velocity, laser repetition rate and laser spot size. Assuming a supersonic jet with a velocity of 1000 m/s and a laser repetition rate of 10 kHz, the atoms in the gas jet should travel 10 cm along the laser beam to be able to interact with the lasers at least once. Additionally, the small laser spot area needed to achieve saturation intensity imposes a

limit for the gas jet diameter.

5.1. Development of new nozzles for the LIST method

5.1.1. Carrier gas jet

As Fig. 9 in article **II** shows, the simple exit holes typically used at IGISOL are indistinguishable in terms of the gas jet geometry over a wide range of ion guide to background pressure ratios. Although the exit holes were able to produce small well-collimated gas jets, this only occurred when the background pressure in the vacuum chamber was high. At IGISOL this situation is unacceptable due to the presence of the RF and (DC) electric fields of SPIG which, if operated under high background pressure, would lead to discharging [160]. Additionally, the high pressure load in the target chamber would lead to poor pressure in the extraction region. The resulting energy spread of the IGISOL beam is highly sensitive to the background pressure in which the ions are accelerated.

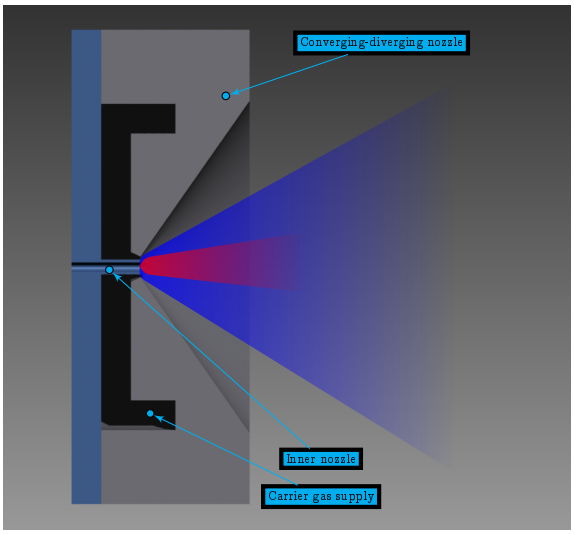

Figure 5.2. The principle of a carrier gas jet. A carrier gas (blue) is emitted from a converging-diverging nozzle. The buffer gas containing the thermalized reaction products (pink) is injected into the supersonic jet via a smaller nozzle within the converging-diverging nozzle.

Therefore, an alternative solution for the gas jet shaping was needed. Initially it was proposed to use a similar nozzle construction that has been investigated as a possible source for gaseous targets in storage rings [161, 162]. In a carrier gas jet nozzle, a simple converging-diverging nozzle with a relatively large throat is fitted with a smaller nozzle in a manner that resembles a common aerospike nozzle [163]. The buffer gas containing the thermalized reaction products is emitted from the the inner nozzle into a supersonic jet formed by the main converging-diverging nozzle. In order to examine the feasibility of such a design a simple test nozzle was constructed seen in Fig. 5.2. Although the nozzle was able to provide rudimentary jet shaping, the background pressure did not improve due to increased gas load from the carrier jet. Furthermore, the achieved shaping was not optimal as seen in Fig. 5.3 hence the concept was discarded. Nevertheless, the carrier gas jet idea is intriguing and may be utilized with the hot cavity catcher described in Chapter 6.

5.1.2. de Laval nozzle

A de Laval nozzle is a converging-diverging nozzle widely used in aerospace applications and in aerodynamic research. It can be used to produce uniform low-divergent flows at pressure ratios far larger than simple converging nozzles. The key to providing a highly uniform, low divergent expansion at low background pressure is to carefully design the contour of the nozzle such that the flow after the exit has a constant Mach number and hence constant density and temperature. The de Laval nozzle achieves this by forcing the gas to expand in a controlled manner, so that upon exiting the nozzle the radial velocity component is minimized. The design of the convergent region is less critical to the performance of the nozzle, although in general the convergent section should have a relatively large radius of curvature near the throat region (five times the throat radius) [164]. However, the shape of the divergent section has to be precisely calculated and manufactured in order to minimize the thickness of the boundary layer [165].

In order to study the concept, a de Laval nozzle was designed with a throat diameter of 1.45 mm so that the flow through the nozzle would be similar to the existing IGISOL designs (see Fig. 5.4). Rather than precisely calculating the nozzle contour, the design presented here was based on existing shapes found in the literature [165,166] with constraints placed by the manufacturing capabilities of the JYFL workshop. The nozzle exit diameter of 6 mm yields an area ratio (exit/throat) of 17.2 which corresponds to a Mach number of $\sim$6.2 and to a pressure ratio of about 0.0014 utilizing Eqs. 2 and 3 in Article **II** . For example, for an ion guide pressure

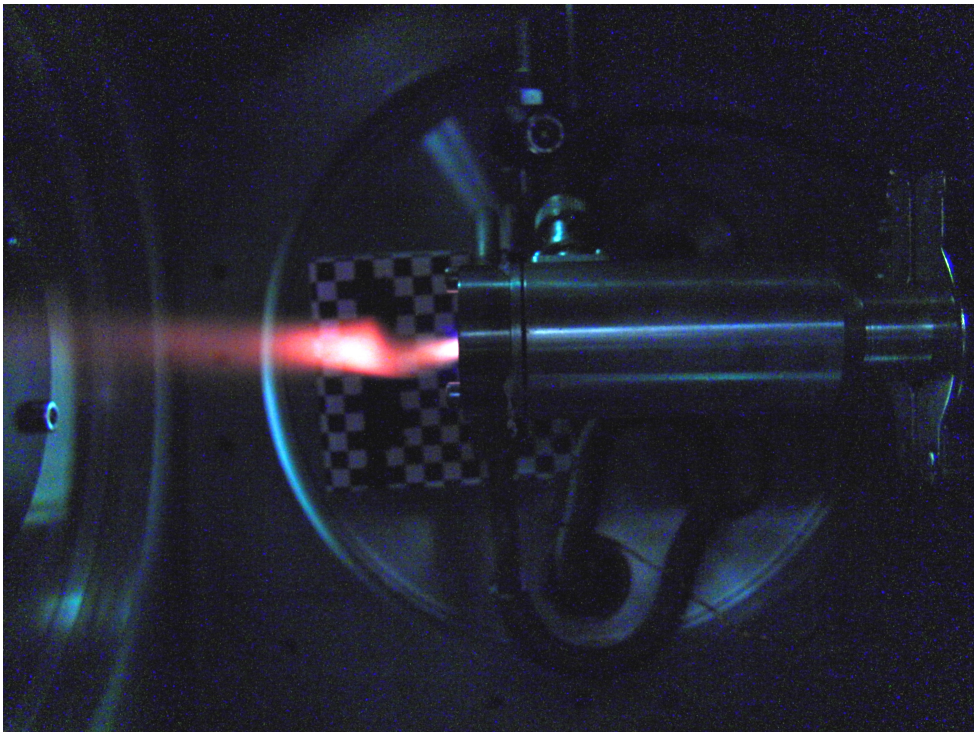

Figure 5.3. An argon jet produced with a helium carrier jet. The shape of the jet was highly dependent on the pressure in both the in guide and in the carrier. The asymmetry in the jet arises from a slight misalignment of the inner nozzle with respect to the converging diverging nozzle.

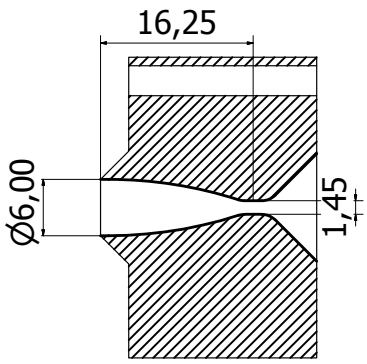

Figure 5.4. A CAD drawing of the de Laval nozzle used for gas jet shaping. Units are in mm.

of 250 mbar the background pressure in the target chamber should be ∼0.35 mbar in order to satisfy the design condition.

The general features of the supersonic jet from a de Laval nozzle were studied by visualizing the jet using discharge excitation as seen in Fig. 13 of Article **II**. Additionally, a Pitot probe was used for a more direct measurement of the jet properties. The Pitot probe is in principle a thin needle with a hole in the tip. The probe measures the total pressure in the jet which is a sum of the static pressure within the expansion vessel and the impact pressure caused by the jet. The impact pressure is extremely sensitive to the Mach number M within the jet. By inserting the probe into the jet, a standing shockwave is induced in the flow. Assuming that the slowing down of the flow downstream from the shock wave is isentropic, the static pressure p_s and impact pressure p_i are linked to the Mach number through the Rayleigh-Pitot relationship presented in Article **II** and in Ref. [167]. Once the Mach number along the jet is known, the pressure in the jet P, the jet velocity V and the jet temperature T can be calculated using equations:

$$\frac{P}{P_{in}} = \left(1 + \frac{\gamma - 1}{2} M^2\right)^{-\gamma/(\gamma-1)} \tag{5.1}$$

$$V^2 = \frac{\gamma - 1}{2} M^2 \left(1 + \frac{\gamma - 1}{2} M^2\right)^{-1} \cdot V_{max}^2 \tag{5.2}$$

$$T = T_{in}(1 + \frac{\gamma - 1}{2} M^2)^{-1}, \tag{5.3}$$

where P_{in} is the static pressure for $M = 0$, in otherwords the ion guide pressure, T_{in} is the ion guide temperature and V_{max} is the thermodynamic limit for the gas velocity at $M = \infty$. Fig. 14 of Article **II** illustrates the impact pressure along the jet axis, whereas Fig. 5.5 in this chapter shows the evolution of the Mach number, velocity, and temperature along the jet axis. The design Mach number for the de Laval nozzle was 6.2 meaning that under optimal pressure regimes the flow after the nozzle would retain this Mach number. However, as can be seen in Fig. 5.5 the measured Mach number ranges from ~4 to ~10 corresponding to the shock features within the jet. This is a clear indication that the pressure ratio between the ion guide and the expansion does not match the nozzle design condition. Additionally, as the nozzle contour was not precisely calculated, effects such a jet detachment could have disturbed the flow. Nevertheless, the bottom row in Fig. 5.5 demonstrates the benefits of such a nozzle. The temperature of the jet is very low, only a few tens of Kelvin, which when combined with the low pressure in the jet, forms a highly attractive environment for laser spectroscopy.

Recently, a second de Laval nozzle was manufactured with an exit diameter of 6 mm and throat diameter of 0.5 mm, leading to an area ratio of 144 and design pressure ratio of $4 \cdot 10^{-5}$. This is two orders of magnitude lower than the pressure ratio of the previous nozzle which means for an ion guide pressure of 300 mbar, the background pressure in the target chamber would only need to be $1 \cdot 10^{-2}$ mbar. These pressure regimes are close to the typical IGISOL operating conditions.

It should be noted that neither this new nozzle nor the one presented in Article **II** have calculated diverging contours. The new de Laval nozzle was built to test whether a small throat could be manufactured. Figure 5.6 presents a photograph of a jet emitted from the nozzle under near optimal operating conditions.

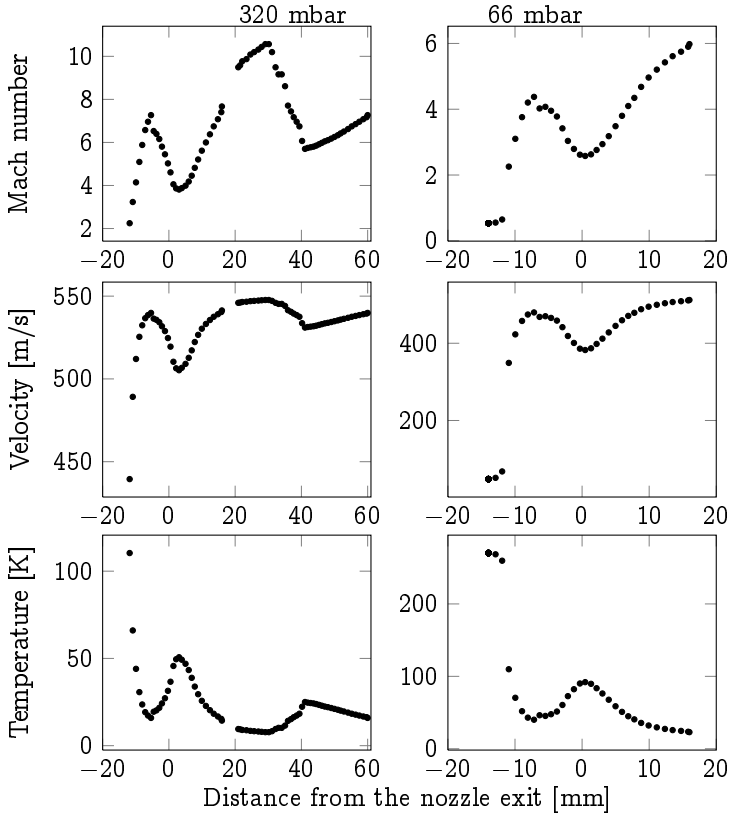

Figure 5.5. Mach number, temperature and velocity calculated for a supersonic argon gas jet using Eqs.5.1, 5.3 and 5.2 for two ion guide pressures, 320 mbar and 66 mbar. The nozzle throat begins at ∼-15 mm in the figure. Note that the x-axis scales of the two pressures are different.

Figure 5.6. A photograph of the slightly underexpanded gas jet of argon emitted from the new de Laval nozzle. Using the 1 cm by 1 cm checker board in the background, the jet length can be estimated to be ∼9 cm with a width of ∼6 mm if one disregards the halo around the shock structure.

6. Hot cavity catcher laser ion source

6.1. Motivation - the production of ^{94}Ag

The radioactive neutron deficient silver isotopes around the $N{=}Z$ region have been of considerable interest for several years. The isotope $N{=}Z$ ^{94}Ag, has been identified as having a spin trap isomer with the highest spin, (21^{+}), ever observed for β-decaying nuclei. The isomer's long half-life of 0.39(4) s [168], high excitation energy [169] and high spin [170] are matched by an unparalleled selection of decay modes including, among others, β decay [170] and one-proton [171] decay. However, the most exotic form of decay that is claimed to exist in ^{94m}Ag(21+) is two-proton emission which, if confirmed, would make this isomer unprecedented in the entire known Segré chart. In general, the two proton emission channel, predicted by Goldansky in 1960 [172], is a very rare decay channel and has so far only been reliably observed either in a few extremely short-lived nuclei: ^{6}Be [173], ^{12}O [174], ^{19}Mg [175] and ^{16}Ne [176] or in isolated cases, namely: ^{45}Fe [177, 178] and ^{54}Zn [179]. A overview of the recent status of two-proton decay is presented in Ref. [180].

Recently, the existence of the two-proton decay mode was questioned [181] due to a lack of states in ^{92}Rh that were used as evidence for the decay. Furthermore, mass measurements of ^{92}Rh and ^{94}Pd, the respective two-proton and β -decay daughters of ^{94}Ag, have been performed which, when combined with the original spectroscopic decay data, lead to a contradiction. The energy of the isomer differs by approximately 1.4 MeV if deduced using the original one-proton compared to the original two-proton decay data [182]. Additionally, an experiment performed at Lawrence Berkeley National Laboratory (LBNL) aiming to confirm the two-proton decay failed to observe the evidence for the decay channel [183]. Lastly, it was proposed by Mukha *et al.* that the unexpectedly large probability for the enhanced two-proton decay could be due to a strongly deformed prolate shape of ^{94}Ag [169]. However, large-scale shell model calculations performed by Kaneko *et al.* [184] do not support such an observation. Only a direct measurement of the nuclear quadrupole moment of the isomer can clarify this discrepancy. All this has led to an intense discussion about the existence of the decay channel [185, 186] and to possible misidentification of such a channel due to the deficiencies of the measurement set-up [187].

To solve the conundrum, direct mass measurements of ^{93}Pd, ^{94}Ag and ^{94m}Ag(21^+) are needed which will allow unambiguous determination of the energy of isomer. In addition to performing high precision mass measurements, in-source resonance ionization spectroscopy will be performed on ^{94}Ag which will provide model-independent information on the change of the mean-square charge radii and, furthermore, by measuring the hyperfine structure of the isomeric states the spectroscopic quadrupole moment and thus the shape of the isomer can be resolved.

6.2. Laser spectroscopy of silver

An efficient laser ionization scheme for silver has been characterized and tested [134]. However, the scheme still has a possible bottleneck which is the final non-resonant transition into the continuum performed with a copper vapour laser (CVL). Near future experiments will look into the possibility to access auto-ionizing states from the second resonant level in the scheme. Most recently, a comparison was performed at IGISOL-4 between CVL, Nd:YAG and a Ti:sapphire operating at $\sim$ 800 nm in order to study the non-resonant ionization efficiency. It was observed that the Ti:sapphire laser was able to provide considerably higher counts rates despite the much lower power compared to the other lasers. It is thought that this may be due to the distance over the ionization potential reached with the different wavelengths

In addition to the interest in the silver nucleus, the silver atom has attracted much attention due to a very narrow $4d^{10}5s^2S_{1/2} \rightarrow 4d^9 5s^2\ ^2D_{5/2}$ transition that could be used as an optical frequency standard [188]. Atomic studies have also yielded a wealth of information on the ground state transitions. For example, the hyperfine splitting in ^{107,109}Ag [189–191] and the isotope shifts [138] for the 328.1624 nm transition utilized in the RIS scheme at IGISOL are described in literature and provide a good reference point for future in-source laser spectroscopy. Figure 6.1 presents the 328.1624 nm ground state transitions from Fig. 4.6a in detail including the hyperfine levels and their splitting for ^{109}Ag.

Resonance laser ionization spectroscopy of silver has been demonstrated at several on-line facilities using both Ti:sapphire and dye lasers. Due to broad hyperfine splitting in silver nuclei with nuclear spins 9/2 or 7/2 [192], it has been possible to resolve the hyperfine structure using broadband Ti:sapphire lasers or dye lasers with hot cavities. Moreover, resonance laser ionization using Ti:sapphire lasers has been demonstrated to be able to to separate nuclear isomers from their ground state as was proved at the TRILIS ion source, TRIUMF, for ^{105,105m}Ag [193]. These

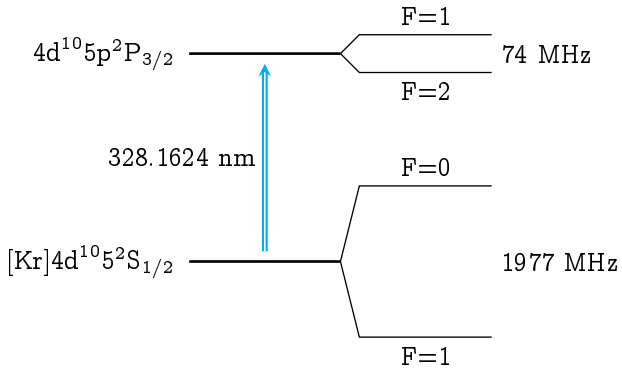

Figure 6.1. Hyperfine levels and their splitting for the $4d^{10}5s^2S_{1/2} \rightarrow 5p^25s^2\ ^2P_{3/2}$ transition used in the silver ionization scheme [138].

achievements demonstrate the potential of the solid state laser -based resonance ionization spectroscopy and the confidence that resonance ionization spectroscopy can be used to extract relevant nuclear data on neutron-deficient silver isotopes in the near future.

6.3. Development of a radioactive beam of ^{94}Ag

There will always be developments which are tailored towards a specific physics goal, and the work in this chapter details the on-going efforts towards the production of the exotic silver isotope $N{=}Z$ ^{94}Ag.

A program has been initiated [134, 194] at IGISOL to selectively and efficiently produce a low-energy ion beam of neutron deficient silver isotopes including ^{94}Ag using heavy-ion fusion-evaporation reactions. To effectively stop the fusion evaporation recoils, two approaches are being investigated. First, the shadow gas cell will be utilized at IGISOL-4 in a manner similar to the work performed at Leuven. Second, a hot cavity catcher device will be utilized. The advantage of the latter method lies in the fast release time of several ms and an extraction efficiency of up to 40 %, achievable with a FEBIAD-type ion source [195].

In this chapter, a catcher design based on thermal ionizer and the FEBIAD Catcher-Ion-Source Systems (CISSs) by R. Kirchner [196] is introduced along with relevant results. Secondly, a derivative of the this catcher is introduced. The inductively

heated hot cavity catcher was designed to replace the complex electron bombardment heating system used in the first hot cavity catcher. Unlike the first catcher device, which was acquired from GSI, Darmstadt, the inductively heated catcher was build in-house in collaboration with the JYFL ECR group.

6.3.1. Catcher design

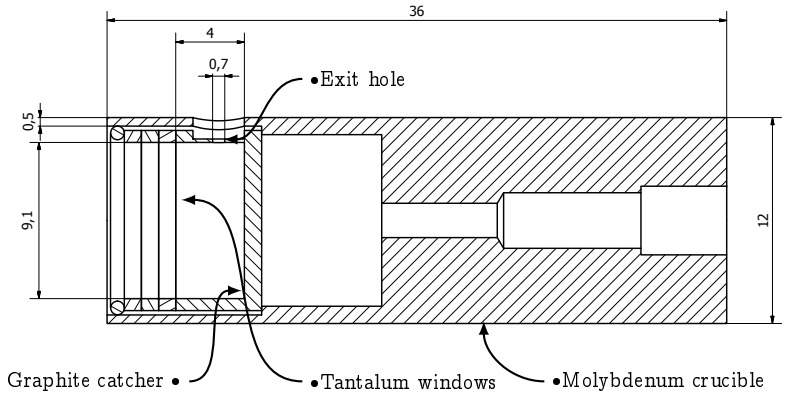

Figure 6.2. A schematic drawing of the crucible of the inductively heated hot cavity catcher. Relevant dimensions are in mm.

Hot cavity catcher structure and material considerations are discussed in detail in articles by R. Kirchner [195, 196]. These articles, along with the existing hot cavity catcher borrowed from GSI, were used as the basis for the design of the inductively heated hot cavity catcher. The general crucible design is presented in Fig. 6.2. Despite the differences in the heating mechanisms, the general idea of the hot cavity catcher is independent of the method of crucible heating(see Fig.6.3).

The first hot cavity catcher iteration and the initial tests for the production of radioactive silver are presented in Article **III** titled "A hot cavity catcher ion source at IGISOL" [134]. The article presents the first resonance ionization of metallic silver at IGISOL utilizing a hot cavity catcher. It was observed that while the mass resolving power of the separator was comparable (~ 470) to SPIG-coupled ion guides, the observed atomic linewidth was greatly Doppler broadened. It was also shown that the laser ionization process can be fully saturated, including the final non-resonant ionization step when a pump laser is used to directly ionize the atoms into the continuum. The maximum temperature achieved with the catcher was about

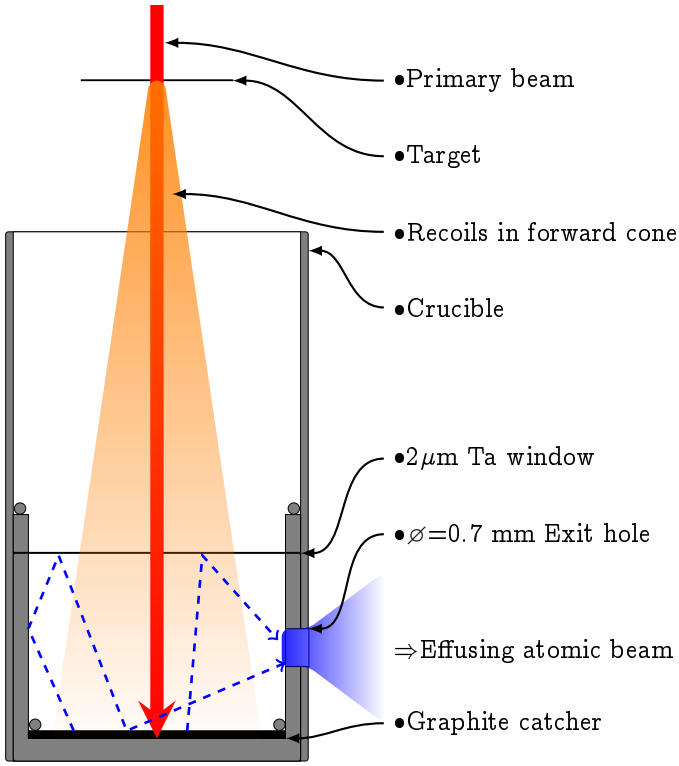

Figure 6.3. The operational principle and important features of the hot cavity catcher used at IGISOL. A primary beam (red) induces fusion-evaporation in the target and the resulting products recoil out towards the catcher (orange). Both the primary beam and the reaction products enter the hot cavity via a thin window and implant into the graphite catcher. Via intense heating, the reaction products diffuse out from the catcher and effuse through the exit hole.

1700 °C. However, the electron bombardment heating mechanism was unstable at high temperatures which led to the catcher melting on multiple occasions. Despite the difficulties concerning the heating system, the work presented in Article **III** demonstrates the feasibility of a hot cavity catcher laser ion source at IGISOL.

6.4. Inductively heated hot cavity catcher

During the testing of the hot cavity catcher discussed in Article **III** it became apparent that an alternative heating mechanism was needed. The electron bombardment heating utilized in the catcher resulted in a usable temperature limit of ~1700°C, above which the temperature became very unstable leading typically to a runaway effect in the bombardment current. Even well below the ~1700°C limit the heating mechanism exhibited unwanted instability.

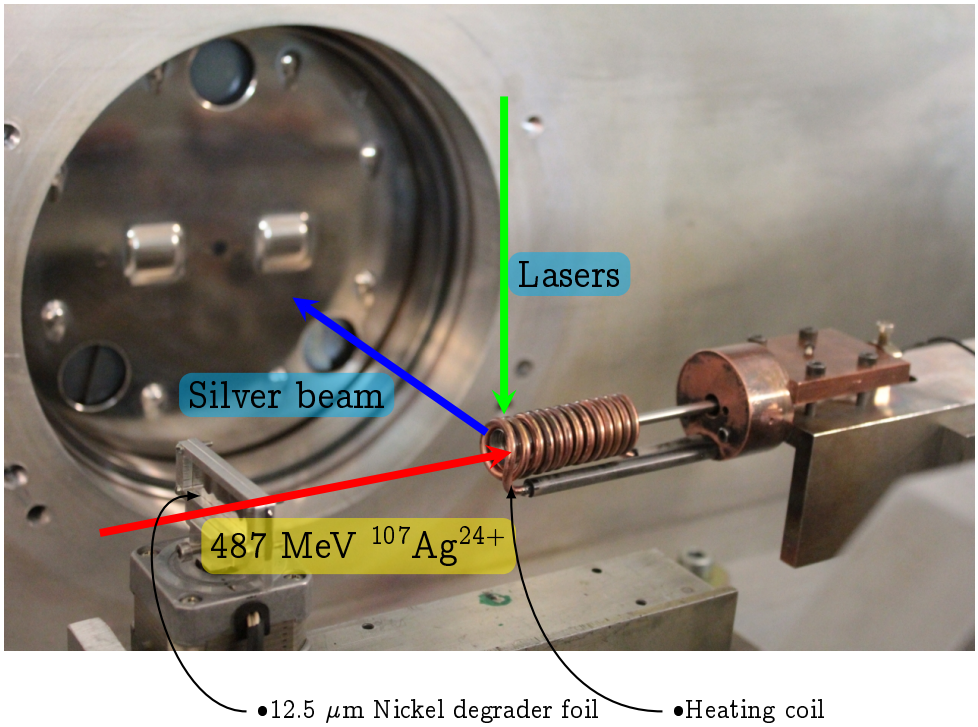

Figure 6.4. Test set-up for the inductively heated hot cavity catcher. The extraction electrode is behind the gate valve seen in the background. During an experiment, the extraction electrode sits ~ 30 mm from the catcher. The hot cavity catcher is located within the heating coil.

In parallel to this work, new ovens are required for the ECR ion source at JYFL, motivated by the request of the user community for the development of new metal-

lic beams of refractory elements such as titanium. In collaboration with the JYFL ECR group, a novel radio frequency inductively -heated hot cavity catcher has recently been developed for the IGISOL facility. The hot cavity catcher test set-up is presented in Fig. 6.4. A cover heat shield, not shown, is added during normal operation. The associated electronics, illustrated in Fig. 6.5, were adapted to fit the existing catcher dimensions and the IGISOL target chamber.

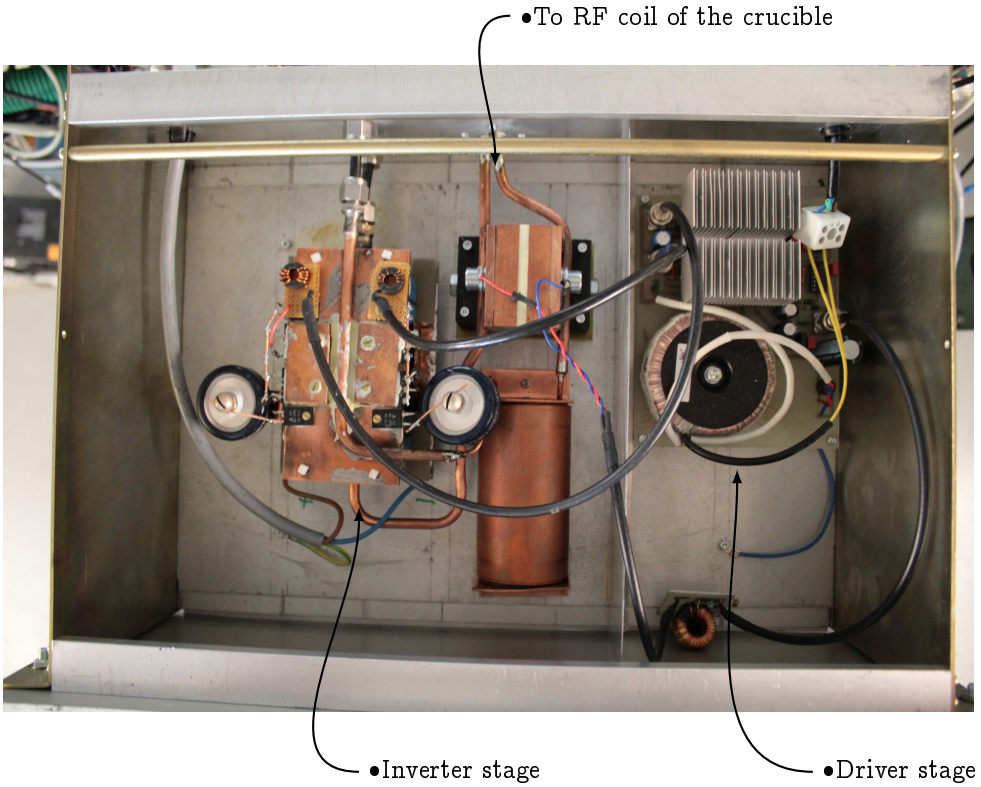

Figure 6.5. A photograph of the RF inductive heating power supply showing the driver and rectifier stages. The supply, including the RF coil, is water cooled.

Article **IV**(Preliminary template) presents the inductively heated hot cavity catcher including the motivation and the principle design for the device. The RF electronics that supply the power for inductive heating are addressed in detail. The main achievement has been an on-line proof of principle test of the hot cavity catcher.

While the previous catcher was commissioned with metallic silver with promising results, the inductively heated source has been commissioned using a stable silver beam from the K-130 cyclotron. A 487 MeV of $^{107}Ag^{21+}$ from the K-130 cyclotron was implanted into the graphite catcher at depths corresponding to the simulated [197] implantation depths of the ^{94}Ag fusion-evaporation products [194]. Following inductive heating to temperatures of typically 1700°C, the implanted silver atoms diffused out from the graphite. Upon effusing from the catcher cavity the silver atoms were resonantly ionized by perpendicular laser beams. The ions were accelerated by the -10 keV extractor field, mass separated and detected in the focal plane using a set of microchannel plates. The silver ions were identified by scanning the first step laser over the resonance. The total evacuation times for different implantation depths and temperatures were measured by pulsing the primary beam and measuring the signal rise time. The evacuation time varied from about 2.5 ms to about 7 ms depending on the catcher temperature and the implantation depth.

The inductively heated hot cavity catcher will be installed at IGISOL-4 in the near future. The aim is first to revisit the tests performed at IGISOL-3 in order to confirm the three main observations: a fast extraction of silver (∼4-5 ms at 1400 °C); poor efficiency due to the resonance ionization geometry; and a strikingly poor mass resolving power of ∼30 for the mass separator. The reason for the latter observation has been traced to the inductive heating RF field using ion-optical simulations. As a solution, a new hot cavity catcher platform has been constructed that enables the use of a transfer tube to shield the silver ions from the RF coils. Furthermore, the IGISOL-4 frontend has been designed to allow a counter-propagating resonance ionization geometry to be utilized. This will greatly increased the ionization efficiency. Combining these future developments with the fast release time of silver, the inductively heated hot cavity catcher will be ready for the on-line production of neutron deficient silver isotopes in the near future.

7. Summary and outlook

This Ph.D. thesis includes a variety of development and experimental projects which can be generally grouped under three subjects: FURIOS improvements, LIST optimization and the development of the hot cavity catcher laser ion source.

The FURIOS facility at IGISOL-3 suffered heavily from a poor laser transport path and inconvenient coupling into the IGISOL ion guides which at worst led to ∼80% losses in laser intensity. Additionally, the LIST method was very inefficient due to an inaccessible window in the separator magnet needed for the counter-propagating ionization geometry. Due to these deficiencies operating the laser ion source under on-line conditions for the production and study of radioactive nuclei would have been impractical. In order to overcome the restrictions of IGISOL-3, the laser ion source facility was completely redesigned during preparation for the move to the IGISOL-4 facility. This allowed the laser transport paths to be optimized along with the coupling into the IGISOL target chamber.

Developments in the laser technology have led to a considerable increase in the available laser power. At IGISOL-3 the fundamental output power from the Ti:sapphire lasers was of the order of 3 to 4 W. Work in this thesis has led to an improvement of the power up to ∼6 W. A dramatic, factor of ∼7, increase in second harmonic power has been a direct result from the development of intra-cavity second harmonic generation. These improvements, coupled with the optimized laser transport path, will enable the FURIOS laser ion source to become a key part of the IGISOL-4 facility for the efficient and selective production of low energy radioactive ion beams.

The studies performed in the thesis have led to improvements in the ion detection and wavelength monitoring, hence to a better understanding of systematic uncertainties for in-source spectroscopy. The FURIOS laser system has demonstrated sensitivity to the isotope shift in stable nickel, although with large uncertainties due to the broad laser linewidth. The development of an injection-locked Ti:sapphire laser with a linewidth of ∼20 MHz is underway which will enable high resolution in-source spectroscopy at IGISOL. In anticipation of this narrow linewidth capability, a hyperfine spectrum analysis software program has been written.

Resonance laser ionization in a gas cell at IGISOL-3 has suffered from primary

beam-induced recombination effects which limits the accessible neutral fraction under on-line conditions. The problem was recently solved by the LISOL group in Louvain-la-Neuve, Belgium, by partitioning the ion guide into separate stopping and ionization chambers. A similar shadow gas cell has been constructed at IGISOL and commissioned successfully under pseudo-on-line conditions. Laser ionization of nickel has been performed on atoms created from the knockout of window material during the passing of a primary $^{4}He^{2+}$ beam. This is an important milestone towards the on-line laser ion source operation at IGISOL. Furthermore, the efficiency of the shadow gas cell has been determined using ^{219}Rn recoils. Efficiencies of ∼2 % were obtained from the stopping chamber, ∼11 to 17 % from the ionization chamber.

The application of the laser ion source trap (LIST) method is currently limited due to a poor efficiency resulting from a small geometrical overlap of the laser beam and gas jet. This thesis has studied methods of gas jet shaping, successfully being realized using a de Laval nozzle. This type of nozzle utilizes a shaped contour to produced a narrow (⌀∼6 mm) collimated gas jet visibly exceeding 14 cm. The jet structure was studied via computer analysis of photographs of fluorescence emitted during the de-excitation of excited states in argon populated via electric discharge. The reliability of the visualization method is supported by the detection of radioactive ^{219}Rn recoils within the jet and computational fluid dynamic simulations.

The supersonic jet produced by the de Laval nozzle is a highly attractive environment for laser spectroscopy. Direct Pitot probe measurements have demonstrated very low, 10 -50 K, temperatures within the jet in addition to a very low pressure. These jet characteristics greatly reduce the effect of the environmental broadening on the atomic lines compared to in-source spectroscopy.

In-jet spectroscopy of nickel has been performed with a standard exit hole. A clear shift of the transition centroid was observed corresponding to a jet velocity of ∼1128 m/s. Additionally, the lower temperature and pressure within the jet reduced the observed linewidth by ∼ 400 MHz, which is dominated by the laser linewidth.

The hot cavity catcher laser ion source is a completely new type recoil stopper at IGISOL, motivated by the wish to produce a beam of $N{=}Z$ ^{94}Ag. Initially, a hot cavity catcher based on FEBIAD and thermal ionizer designs was acquired from GSI and adapted for use at IGISOL. The catcher was demonstrated under off-line conditions by evaporating and resonantly ionizing metallic silver.

The electron bombardment mechanism allowed the first hot cavity catcher to reach temperatures up to 1700 °C however, the stability deteriorated leading to melting of the catcher. This motivated the development of an inductive heating system

in collaboration with the JYFL ECR group. The RF inductively heated hot cavity catcher exceeded temperatures of 2000 °C and is able to maintain high temperatures for extended periods. Commissioning was demonstrated in an experiment which involved the implantation of a 487 MeV beam of $^{107}Ag^{+21}$. The extraction time for the implanted silver ions was less than 10 ms for catcher temperatures less than 1200 °C.

Two limitations were found during the on-line commissioning of the inductively heated hot cavity catcher laser ion source. Firstly, the laser ion source efficiency is limited due to the perpendicular ionization geometry available at IGISOL-3. Secondly, adjacent pulses of laser produced ions experienced a different potential due to the oscillating RF phase, resulting in an increase in the energy spread and beam emittance. This was observed in measurements of the mass resolving power and has been supported with simulations.

The hot cavity catcher platform has been recently redesigned to be used at IGISOL-4 to overcome the limitations. Upgrades include the access to efficient counter-propagating laser ionization geometry, and shielding of the ionization region from the RF coils. The catcher will be installed at IGISOL-4 in the near future with the first goal to confirm the results obtained at IGISOL-3.

List of publications

* M. Reponen, T. Kessler, I.D. Moore, S. Rothe and J. Äystö,
A Hot Cavity Laser Ion Source at IGISOL
Eur. Phys. J. A 42 3 (2009) 509-515

* M. Reponen, I.D. Moore, I. Pohjalainen, T. Kessler, P. Karvonen, J. Kurpeta, B. Marsh, S. Piszczek, V. Sonnenschein, J. Äystö,
Gas jet studies towards an optimization of the IGISOL LIST method
Nucl. Instr. in Phys. Res. A 635 1 (2011) 24-24

* M. Reponen, I. D. Moore, T. Kessler, I. Pohjalainen, S. Rothe and V. Sonnenschein
Laser developments and resonance ionization spectroscopy at IGISOL
Eur. Phys. J. A. 48 (2012) 45

- A. Kankainen, Yu. N. Novikov, M. Oinonen, L. Batist , V.-V. Elomaa, T. Eronen, J. Hakala, A. Jokinen, P. Karvonen, M. Reponen, J. Rissanen, A. Saastamoinen, G. Vorobjev, C. Weber and J. Äystö.
Isomer and decay studies for the rp process at IGISOL
Eur. Phys. J. A 48 (2012) 49

- C. Rodriguez Triguero, A.M. Bruce, T. Eronen, I.D. Moore, M. Bowry, A.M. Denis Bacelar, A.Y. Deo, V-V. Elomaa, D. Gorelov, J. Hakala, A. Jokinen, A. Kankainen, P. Karvonen, V.S. Kolhinen, J. Kurpeta, T. Malkiewicz, P.J.R Mason, H. Penttilä, M. Reponen, S. Rinta-Antila, A. Saastamoinen, G. Simpson and J. Äystö.
Trap-assisted separation of nuclear states for gamma-ray spectroscopy: the example of ^{100}Nb
J. Phys. G. 39 (2012) 015101

- M. B. Gómez-Hornillos, J. Rissanen, J. L. Taín, A. Algora, D. Cano-Ott, J. Agramunt, V. Gorlychev, R. Caballero, T. Martinéz, L. Achouri, J. Äystö, G. Cortés, V-V. Elomaa, T. Eronen, A. García, J. Hakala, A. Jokinen, P.

Karvonen, V. S. Kolhinen, I. D. Moore, M. Parlog, H. Penttilä, Z. Podolyak, C. Pretel, M. Reponen, V. Sonnenschein and E. Valencia
First Measurements with the BEta deLayEd Neutron Detector (BELEN-20) at JYFLTRAP
Journal of Physics: Conference Series 321, 5 (2011) 052008

- J. Hakala, R. Rodriguez-Guzman, V.-V. Elomaa, T. Eronen, A. Jokinen, V.S. Kolhinen, I. D. Moore, H. Penttilä , M. Reponen, J. Rissanen, A. Saastamoinen, and J. Äystö
Precision mass measurements of neutron-rich Y, Nb, Mo, Tc, Ru, Rh, and Pd isotopes
Eur. Phys. J. A 47, 129 (2011).

- H. Penttilä, T. Eronen, J. Hakala, A. Jokinen, A. Kankainen, P. Karvonen, V. S. Kolhinen, I.D. Moore, J. Rissanen, M. Reponen, A. Saastamoinen, V. Sonnenschein, and J. Äystö
The possibilities of the extended IGISOL facility at JYFL
J. Korean Phys.Soc. 59 (2011) 1589 - 1592.

- S. Raeder, V. Sonnenschein, T. Gottwald, I. D. Moore, M.Reponen, S. Rothe, N. Trautmann and K. Wendt
Resonance ionization spectroscopy of thorium isotopes - towards a laser spectroscopic identification of the low-lying 7.6 eV isomer of ^{229}Th
J. Phys. B: At. Mol. Opt. Phys. 44 (2011) 165005.

- O.S. Kirsebom, S. Hyldegaard, M. Alcorta, M.J.G. Borge, J. Büscher, T. Eronen, S. Fox, B. R. Fulton, H.O.U. Fynbo, H. Hultgren, A. Jokinen, B. Jonson, A. Kankainen, P. Karvonen, T. Kessler, A. Laird, M. Madurga, I. Moore, G. Nyman, H. Penttilä, S. Rahaman, M. Reponen, K. Riisager, T. Roger, J. Ronkainen, A. Saastamoinen, O. Tengblad, J. Äystö
Precise and accurate determination of the ^{8}B decay spectrum
Phys. Rev. C 83, 065802 (2011).

- T. Eronen, D. Gorelov, J. Hakala, J. C. Hardy, A. Jokinen, A. Kankainen, V.S.Kolhinen, I. D. Moore, H. Penttilä, M. Reponen, J. Rissanen, A. Saastamoinen, J. Aystö
Q_{EC} values of the Superallowed beta-Emitters ^{10}C, ^{34}Ar, ^{38}Ca and ^{46}V
Phys. Rev. C 83, 055501 (2011).

- J. Rissanen, J. Kurpeta, V.-V. Elomaa, T. Eronen, J. Hakala, A. Jokinen, I. D. Moore, P. Karvonen, A. Pochocki, L. Próchniak, H. Penttilä, S. Rahaman,

M. Reponen, A. Saastamoinen, J. Szerypo, W. Urban, C. Weber, J. Äystö
Decay study of ^{114}Tc with a Penning trap
Phys. Rev. C 83, 011301(R) (2011)

- A. Kankainen, T. Eronen, D. Gorelov, J. Hakala, A. Jokinen, V.S. Kolhinen, M. Reponen, J. Rissanen, A. Saastamoinen,V. Sonnenschein, J. Äystö
High-precision mass measurement of ^{31}S with the double Penning trap JYFLTRAP improves the mass value for ^{32}Cl
Phys. Rev. C 82, 052501 (2010)

- A. Kankainen, V.-V. Elomaa, T. Eronen, D. Gorelov, J. Hakala, A. Jokinen, T. Kessler, V.S. Kolhinen, I.D. Moore, S. Rahaman, M. Reponen, J. Rissanen, A. Saastamoinen, C. Weber, J. Äystö
Mass measurements in the vicinity of the doubly-magic waiting point ^{56}Ni
Phys. Rev. C 82, 034311 (2010)

- F.C. Charlwood, K. Baczynska, J. Billowes, P. Campbell, B. Cheal, T. Eronen, D.H. Forest, T. Kessler, I.D. Moore, R. Powis, M. Reponen, M. Rüffer, G. Tungate, J. Äystö
Status of the LASER-IGISOL collaboration at the University of Jyväskylä
Hyp. Int. 196 143-150 (2010)

- T. Eronen, V.-V. Elomaa, J. Hakala, J. C. Hardy, A. Jokinen, I. D. Moore, M. Reponen, J. Rissanen, A. Saastamoinen, C. Weber, J. Äystö
QEC Values of the superallowed β emitters ^{34}Cl and ^{38}Km
Phys. Rev. Lett. 103, 252501 (2009).

- T. Kurtukian Nieto, J. Souin, T. Eronen, L. Audirac, J. Äystö, B. Blank, V.-V. Elomaa, J. Giovinazzo, U. Hager, J. Hakala, A. Jokinen, A. Kankainen, P. Karvonen, T. Kessler, I.D. Moore, H. Penttilä, S. Rahaman, M. Reponen, S. Rinta-Antila, J. Rissanen, A. Saastamoinen, T. Sonoda, C. Weber
Half-life, branching-ratio, and Q-value measurement for the superallowed $0+ \rightarrow 0+$ $\beta+$ emitter ^{42}Ti
Phys. Rev. C 80, 035502 (2009)

- B. Cheal, K. Baczynska, J. Billowes, P. Campbell, F. C. Charlwood, T. Eronen, D. H. Forest, A. Jokinen, T. Kessler, I. D. Moore, M. Reponen, S. Rothe, M. Rüffer, A. Saastamoinen, G. Tungate, J. Äystö
Laser Spectroscopy of Niobium Fission Fragments: First Use of Optical Pumping in an Ion Beam Cooler Buncher
Phys. Rev. Lett. 102, 222501 (2009).

- T. Enqvist, V. Föhr, J. Joutsenvaara, P. Keränen, P. Kuusiniemi, H. Laitala, M. Lehtola, A. Mattila, J. Narkilahti, S. Nurmenniemi, J. Peltoniemi, H. Remes, T. Räihä, C. Shen, M. Reponen, J. Sarkamo, M. Vaittinen, Z. Zhang, T. Jämsén, L. Ding, Q. Zhu, M. Roos, I. Dzaparova, S. Karpov, A. Kurenya, V. Petkov, A. Yanin, H. Fynbo
  EMMA -a new underground cosmic-ray experiment
  Physics of Atomic Nuclei, 70(1), 166-169 (2206).

* Significant contribution

A. Elements ionized with resonant Ti:sapphire schemes

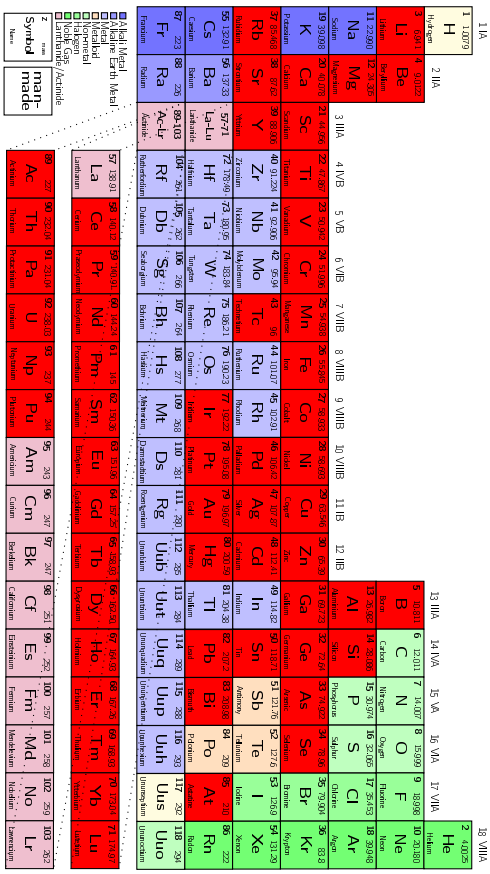

Figure A.1. Periodic table of elements presenting the elements with a Ti:sapphire - compatible ionization scheme (red). Data from the RILIS database [198], "Status Report on EURONS Project-No. 506065 JRA-08 LASER " and from Ref's. [199] and [200]

B. Laser facility design drawings

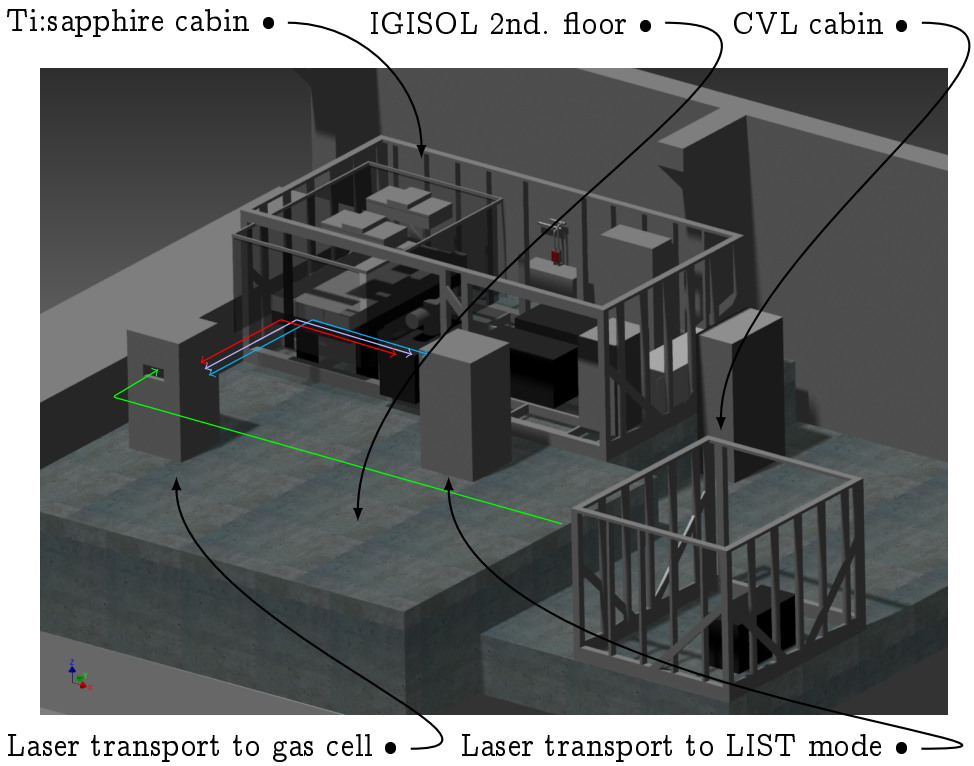

Figure B.1. CAD design of the new FURIOS station at IGISOL 4. The coloured arrows indicate the paths for the lasers. The concrete blocks are radiation shielding requirements.

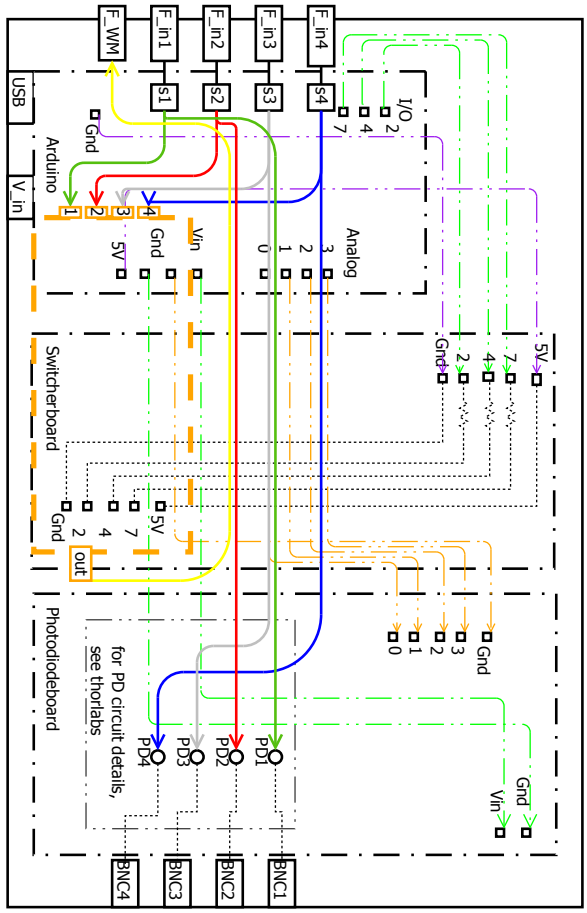

Figure B.2. The electrical schematics of the fiber switcher and timing unit.

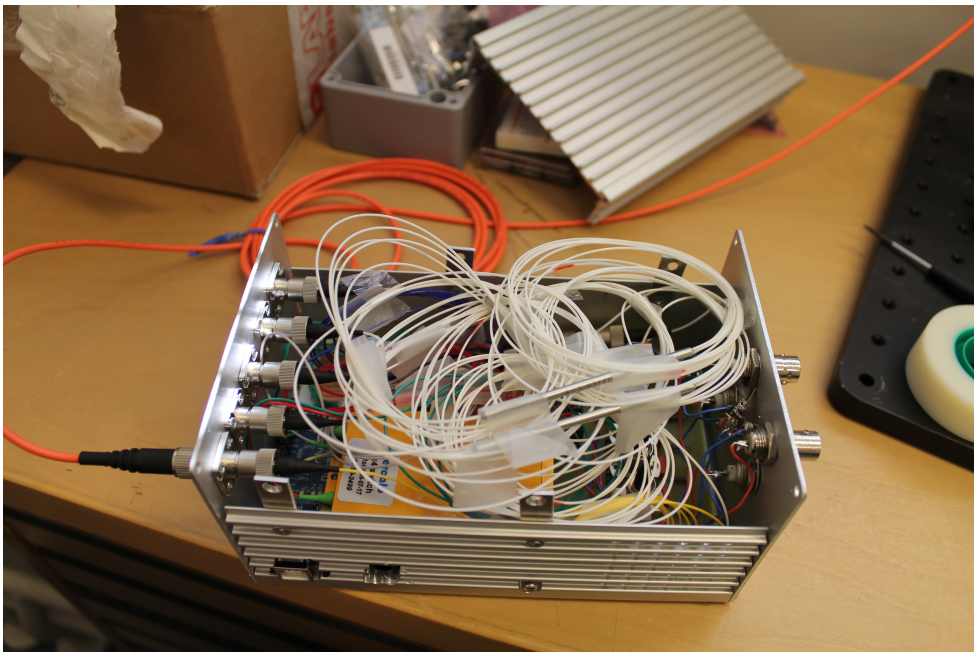

Figure B.3. A photo of the new fibre switcher.

C. Hot cavity catcher

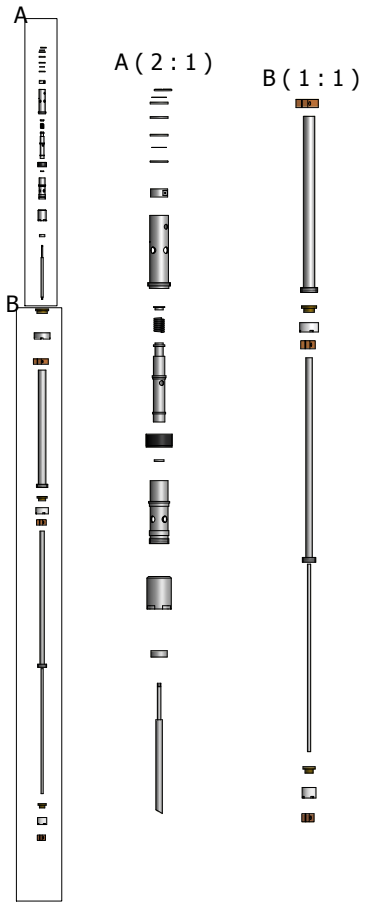

Figure C.1. All the parts in the hot cavity catcher based on the thermal ionizer design.

D. Hyperfine structure and isotope shift analysis code

D.1. Lorentzian fitter

```
//Function that set-ups a fitter to fit
//a multipeak function of  Lorentzian
//line shape to a given dataset.
//The fitter needs to be given the number of
//data points n,   and a struct constantData
//that contains among others the number of peaks
// and all the other constant data
//needed to calculate the spectrum profile
//The solver that calculates the fitfunction utilizes
// Gnu Scientific Librarys Levenberg-Marquardt
// minimisation routine. The routine needs
// a function to calculate the profile f,
// the derivatives of the profile against all
// the fit parameters f.df and
// a function f.fdf. that calls both of these functions.
// Due to GSL being a c-based library, the functions
// f, df and fdf cannot be directly called from C++
// class but they need a wrapper function.

void lorentzianFitter::setSolver(){
    //the number of variables in a lorentzian multipeak
    // fitting is.
    // This does not depend on the number of peaks as all
    // the fit parameters apply for each peak
    // and some of the constants, namely Ic the alphas
    // and the betas, are different for each peak.
    // In the future versions, the number of fit
    // may vary if the fitting conditions are loosened
```

```
    p=8;
    //number of datapoints
    n =constantData.n;
    //setup a covariant matrix for the results according to
    //the number of variables
    covar = gsl_matrix_alloc (p, p);
    //setup the fitfunction
    //set the function that calculates the lorentzian profile
    f.f = &lorentzianFitFunctions_calllorentzian_f;
    //set the function which calculates the derivatives
    f.df = &lorentzianFitFunctions_calllorentzian_fd;
    //set a function to call the lorentzian function
    // + its derivatives
    f.fdf = &lorentzianFitFunctions_calllorentzian_fdf;
    //set the number of datapoints to the fitter
    f.n = n;
    //set the number of parameters to be fitted
    f.p = p;
    //set the struct constant data as the container for
    // the constants and other data
    f.params = &constantData;

    //setup the solver
    //set the initial values and the number of fit parameters
    // into and GSL type array
    x = gsl_vector_view_array (initialValues, p);
    //set the solver alogrithm to Levenberg-Marquardt
    T = gsl_multifit_fdfsolver_lmsder;
    //allocate the solver according to the parameters
    s = gsl_multifit_fdfsolver_alloc (T, n, p);
    /set the solver allocation, the functions, and the
    // initial values to the solver
    gsl_multifit_fdfsolver_set (s, &f, &x.vector);  /

}
//Function to iterate the solver. It needs to know the
//maximum number of iterations and the relative and
//absolute errors to work. Moreover the solver s needs
```

```
//to be allocated and set-up before this function runs.
void lorentzianFitter::iterateSolver(){
    iter=0;
    //iterate while the iteration converges,
    //and the maximum number of iterations
    //"iterations" is not reached or until the relative
    //and the absolute errors ,epsabs, epsrel  are
    //reached.
    returnSolverState(iter, s);
    do{
        iter++;
                //Check fitter status for the iterations
        status = gsl_multifit_fdfsolver_iterate (s);
        if (status){
            break;
        }
        //Check status for convergence
        status =
        gsl_multifit_test_delta (s->dx, s->x,epsabs, epsrel);
    }
    //Evaluate status to see if need to continiue
    while (status == GSL_CONTINUE &&iter < iterations);
    //Fill the covariant matrix J with the fit results
    gsl_multifit_covar (s->J, 0, covar);
    //Call an another member function that
    // outputs the results
    returnSolverState(iter, s);
}
```

D.2. Voigt fit function

```
//The function calculates the center of gravity X0
//double xcz_fVal= x-offset, double Al_fVal= lower A,
// double Bl_fVal=lowerB,
//double Au_fVal=upper A, double Bu_fVal=upper B,
//double all_fVal= lower alpha (constant),
// double bel_fVal=lower beta (constant),
```

```
//double alu_fVal= upper alpha (constant),
//double beu_fVal= upper beta (constant)
double voigtFitFunctions::hfsCenterOfGravity(double xcz_fVal,
double Al_fVal, double Bl_fVal, double Au_fVal, double Bu_fVal,
double all_fVal, double bel_fVal, double alu_fVal, double beu_fVal){
        double cent=xcz_fVal+alu_fVal*Au_fVal+beu_fVal*Bu_fVal-
        all_fVal*Al_fVal-bel_fVal*Bl_fVal;
        return cent;
}

//The function calculates a point in  a Voigt profile for a
// single peak
//double lorentzianAmplitude= amplitude of the peak,
//double peakPosition = peak centroid,
//double lorentzianFWHM=wl, double gaussianFWHM=wg,
//double x= the point wheret the function is evaluated,
//double yOffset=Y
double voigtFitFunctions::voigtFunction(double lorentzianAmplitude,
double peakPosition, double lorentzianFWHM, double gaussianFWHM,
double x, double yOffset){
    int i;
    double A[4],B[4],C[4],D[4],V=0;
    double t=sqrt(M_LN2);
    static double sqrtln2=sqrt(M_LN2);
    static double sqrtpi=sqrt(M_PI);
    double X=(x-peakPosition)*2*sqrtln2/gaussianFWHM;
    double Y=lorentzianFWHM*sqrtln2/gaussianFWHM;
    A[0]=-1.2150; B[0]= 1.2359;
    A[1]=-1.3509; B[1]= 0.3786;
    A[2]=-1.2150; B[2]=-1.2359;
    A[3]=-1.3509; B[3]=-0.3786;
    C[0]=-0.3085; D[0]= 0.0210;
    C[1]= 0.5906; D[1]=-1.1858;
    C[2]=-0.3085; D[2]=-0.0210;
    C[3]= 0.5906; D[3]= 1.1858;
    for(i=0;i <= 3;i++){
        V+=(C[i]*(Y-A[i])+D[i]*(X-B[i]))/
        (pow((Y-A[i]),2)+pow((X-B[i]),2));
```

```
    }
    return (yOffset+(lorentzianFWHM*lorentzianAmplitude*
    sqrtpi*sqrtln2/gaussianFWHM)*V);

}
```

Bibliography

[1] J. Erler, N. Birge, M. Kortelainen, *et al.*, Nature (2012), URL http://www.nature.com/nature/journal/v486/n7404/full/nature11188.html

[2] M. Huyse, in J. Al-Khalili, E. Roeckl, eds., *The Euroschool Lectures on Physics with Exotic Beams, Vol. I*, vol. 651 of *Lecture Notes in Physics*, 1–32 (Springer Berlin / Heidelberg, 2004), URL http://dx.doi.org/10.1007/978-3-540-44490-9_1

[3] R. V. Ambartzumian, V. S. Letokhov, Applied Optics **11**, 2, 354 (1972), URL http://ao.osa.org/abstract.cfm?URI=ao-11-2-354

[4] N. Lecesne, Review of Scientific Instruments **83**, 2, 02A916 (2012), URL http://link.aip.org/link/?RSI/83/02A916/1

[5] H. J. Kluge, F. Ames, W. Ruster, *et al.*, TRIUMF Proceedings TRI-85-1 (1985)

[6] S. Andreev, V. Mishin, V. Letokhov, Optics Communications **57**, 5, 317 (1986), URL http://www.sciencedirect.com/science/article/pii/003040188690266X

[7] V. Mishin, V. Fedoseyev, H.-J. Kluge, *et al.*, Nuclear Instruments and Methods in Physics Research Section B: Beam Interactions with Materials and Atoms **73**, 4, 550 (1993), URL http://www.sciencedirect.com/science/article/pii/0168583X9395839W

[8] S. Rothe, B. A. Marsh, C. Mattolat, *et al.*, Journal of Physics: Conference Series **312**, 5, 052020 (2011), URL http://stacks.iop.org/1742-6596/312/i=5/a=052020

[9] V. N. Fedosseev, L.-E. Berg, D. V. Fedorov, *et al.*, Review of Scientific Instruments **83**, 2, 02A903 (2012), URL http://link.aip.org/link/?RSI/83/02A903/1

[10] J. Lassen, P. Bricault, M. Dombsky, *et al.*, Hyperfine Interactions **162**,

69 (2005), 10.1007/s10751-005-9212-2, URL http://dx.doi.org/10.1007/s10751-005-9212-2

[11] N. Lecesne, R. Alvès-Condé, E. Coterreau, *et al.*, Review of Scientific Instruments **81**, 2, 02A910 (pages 3) (2010), URL http://link.aip.org/link/?RSI/81/02A910/1

[12] A. E. Barzakh, D. V. Fedorov, V. S. Ivanov, *et al.*, Review of Scientific Instruments **83**, 2, 02B306 (2012), URL http://link.aip.org/link/?RSI/83/02B306/1

[13] Y. Liu, T. Gottwald, C. C. Havener, *et al.*, Review of Scientific Instruments **83**, 2, 02A904 (2012), URL http://link.aip.org/link/?RSI/83/02A904/1

[14] *The TANDEM-ALTO facility*, URL http://ipnweb.in2p3.fr/tandem-alto/index_E.html

[15] D. Scarpa, J. Vasquez, A. Tomaselli, *et al.*, Review of Scientific Instruments **83**, 2, 02B317 (2012), URL http://link.aip.org/link/?RSI/83/02B317/1

[16] E. Kugler, Hyperfine Interactions **129**, 23 (2000), 10.1023/A:1012603025802, URL http://dx.doi.org/10.1023/A:1012603025802

[17] B. Marsh, L.-E. Berg, D. Fedorov, *et al.*, Hyperfine Interactions **196**, 129 (2010), 10.1007/s10751-010-0168-5, URL http://dx.doi.org/10.1007/s10751-010-0168-5

[18] V. Fedosseev, L.-E. Berg, N. Lebas, *et al.*, Nuclear Instruments and Methods in Physics Research Section B: Beam Interactions with Materials and Atoms **266**, 19-20, 4378 (2008), URL http://www.sciencedirect.com/science/article/pii/S0168583X08007398

[19] P. Bricault, The European Physical Journal - Special Topics **150**, 227 (2007), 10.1140/epjst/e2007-00310-9, URL http://dx.doi.org/10.1140/epjst/e2007-00310-9

[20] K. Rykaczewski, J. C. Batchelder, C. R. Bingham, *et al.*, Acta Physica Polonica B **30**, 565 (1999), URL http://adsabs.harvard.edu/abs/1999AcPPB..30..565R

[21] L. Vermeeren, N. Bijnens, M. Huyse, *et al.*, Physical Review Letters **73**, 1935 (1994), URL http://link.aps.org/doi/10.1103/PhysRevLett.73.1935

[22] P. Van Duppen, B. Bruyneel, M. Huyse, *et al.*, Hyperfine Interactions **127**,

401 (2000), 10.1023/A:1012657431795, URL http://dx.doi.org/10.1023/A:1012657431795

[23] M. Wada, A. Takamine, T. Sonoda, *et al.*, Hyperfine Interactions **196**, 43 (2010), 10.1007/s10751-010-0162-y, URL http://dx.doi.org/10.1007/s10751-010-0162-y

[24] A. Einstein, Z. Phys **18**, 63 (1917)

[25] T. H. Maiman, Nature **187**, 493 (1960)

[26] W. T. Silfvast, G. R. Fowles, B. D. Hopkins, Applied Physics Letters **8**, 12, 318 (1966), URL http://link.aip.org/link/?APL/8/318/1

[27] F. P. Schäfer, W. Schmidt, J. Volze, Applied Physics Letters **9**, 8, 306 (1966), URL http://link.aip.org/link/?APL/9/306/1

[28] R. N. Hall, G. E. Fenner, J. D. Kingsley, *et al.*, Physical Review Letters **9**, 366 (1962), URL http://link.aps.org/doi/10.1103/PhysRevLett.9.366

[29] J. V. V. Kasper, G. C. Pimentel, Physical Review Letters **14**, 352 (1965), URL http://link.aps.org/doi/10.1103/PhysRevLett.14.352

[30] J. M. J. Madey, Journal of Applied Physics **42**, 5, 1906 (1971), URL http://link.aip.org/link/?JAP/42/1906/1

[31] O. Svelto, *Principles of Lasers* (Springer, 1998)

[32] W. Demtröder, *Laser Spectroscopy - Basic Concepts and Instrumentation* (Springer-Verlag Berlin Heidelberg, 2003)

[33] W. T. Silfvast, *Laser Fundamentals* (Cambridge University Press, 1996)

[34] J. E. Geusic, H. M. Marcos, L. G. V. Uitert, Applied Physics Letters **4**, 10, 182 (1964), URL http://link.aip.org/link/?APL/4/182/1

[35] P. F. Moulton, Journal of the Optical Society of America B **3**, 1, 125 (1986), URL http://josab.osa.org/abstract.cfm?URI=josab-3-1-125

[36] D. Findlay, R. Clay, Physics Letters **20**, 3, 277 (1966), URL http://www.sciencedirect.com/science/article/pii/0031916366903635

[37] W. W. Rigrod, Journal of Applied Physics **36**, 8, 2487 (1965), URL http://link.aip.org/link/?JAP/36/2487/1

[38] W. G. Wagner, B. A. Lengyel, Journal of Applied Physics **34**, 7, 2040 (1963), URL http://link.aip.org/link/?JAP/34/2040/1

[39] Origin (OriginLab, Northampton, MA)

[40] P. A. Franken, A. E. Hill, C. W. Peters, *et al.*, Physical Review Letters **7**, 118 (1961), URL http://link.aps.org/doi/10.1103/PhysRevLett.7.118

[41] E. Roeckl, A. Blazhev, K. Burkard, *et al.*, Nuclear Instruments and Methods in Physics Research Section B: Beam Interactions with Materials and Atoms **204**, 0, 53 (2003), URL http://www.sciencedirect.com/science/article/pii/S0168583X02018906

[42] P. Van Duppen, in J. Al-Khalili, E. Roeckl, eds., *The Euroschool Lectures on Physics with Exotic Beams, Vol. II*, vol. 700 of *Lecture Notes in Physics*, 37–77 (Springer Berlin / Heidelberg, 2006), URL http://dx.doi.org/10.1007/3-540-33787-3_2

[43] R. Kirchner, Nuclear Instruments and Methods in Physics Research Section B: Beam Interactions with Materials and Atoms **26**, 1-3, 204 (1987), URL http://www.sciencedirect.com/science/article/pii/0168583X87907518

[44] P. Van Duppen, A. Andreyev, J. Äystö, *et al.*, Nuclear Instruments and Methods in Physics Research Section B: Beam Interactions with Materials and Atoms **134**, 2, 267 (1998), URL http://www.sciencedirect.com/science/article/pii/S0168583X98007332

[45] L. Penescu, R. Catherall, J. Lettry, *et al.*, Review of Scientific Instruments **81**, 2, 02A906 (pages 4) (2010), URL http://link.aip.org/link/?RSI/81/02A906/1

[46] F. Schwellnus, K. Blaum, C. Geppert, *et al.*, Nuclear Instruments and Methods in Physics Research Section B: Beam Interactions with Materials and Atoms **266**, 19?20, 4383 (2008), URL http://www.sciencedirect.com/science/article/pii/S0168583X08007404

[47] Y. Kudryavtsev, M. Facina, M. Huyse, *et al.*, Nuclear Instruments and Methods in Physics Research Section B: Beam Interactions with Materials and Atoms **204**, 0, 336 (2003), URL http://www.sciencedirect.com/science/article/pii/S0168583X02019468

[48] R. Ferrer-García, V. T. Sonnenschein, B. Bastin, *et al.*, Nuclear Instruments

and Methods in Physics Research Section B: Beam Interactions with Materials and Atoms (2012), to be published

[49] T. Kessler, H. Tomita, C. Mattolat, *et al.*, Laser Physics **18**, 842 (2008), 10.1134/S1054660X08070074, URL http://dx.doi.org/10.1134/S1054660X08070074

[50] R. Neugart, G. Neyens, in J. Al-Khalili, E. Roeckl, eds., *The Euroschool Lectures on Physics with Exotic Beams, Vol. II*, vol. 700 of *Lecture Notes in Physics*, 135–189 (Springer Berlin / Heidelberg, 2006), 10.1007/3-540-33787-34, URL http://dx.doi.org/10.1007/3-540-33787-34

[51] I. Stefanescu, G. Georgiev, F. Ames, *et al.*, Phys. Rev. Lett. **98**, 122701 (2007), URL http://link.aps.org/doi/10.1103/PhysRevLett.98.122701

[52] P. Vingerhoets, K. T. Flanagan, M. Avgoulea, *et al.*, Phys. Rev. C **82**, 064311 (2010), URL http://link.aps.org/doi/10.1103/PhysRevC.82.064311

[53] P. Schulz, S. Henion, Quantum Electronics, IEEE Journal of **27**, 4, 1039 (1991)

[54] J. Billowes, Nuclear Physics A **752**, 0, 309 (2005), URL http://www.sciencedirect.com/science/article/pii/S037594740500182X

[55] B. Cheal, K. T. Flanagan, Journal of Physics G: Nuclear and Particle Physics **37**, 11, 113101 (2010), URL http://stacks.iop.org/0954-3899/37/i=11/a=113101

[56] Peter, Dendooven, Nuclear Instruments and Methods in Physics Research Section B: Beam Interactions with Materials and Atoms **126**, 1-4, 182 (1997), URL http://www.sciencedirect.com/science/article/pii/S0168583X96010105

[57] J. Äystö, Nuclear Physics A **693**, 1-2, 477 (2001), URL http://www.sciencedirect.com/science/article/pii/S037594740100923X

[58] R. MacFarlane, R. Gough, N. Oakey, *et al.*, Nuclear Instruments and Methods **73**, 3, 285 (1969), URL http://www.sciencedirect.com/science/article/pii/0029554X69903991

[59] A. Ghiorso, J. M. Nitschke, J. R. Alonso, *et al.*, Physical Review Letters **33**, 1490 (1974), URL http://link.aps.org/doi/10.1103/PhysRevLett.33.1490

[60] D. Moltz, J. Wouters, J. Äystö, *et al.*, Nuclear Instruments and Meth-

ods **172**, 3, 519 (1980), URL http://www.sciencedirect.com/science/article/pii/0029554X80903432

[61] J. Ärje, J. Äystö, H. Hyvönen, *et al.*, Physical Review Letters **54**, 99 (1985), URL http://link.aps.org/doi/10.1103/PhysRevLett.54.99

[62] V. Korobov, A. Yelkhovsky, Physical Review Letters **87**, 193003 (2001), URL http://link.aps.org/doi/10.1103/PhysRevLett.87.193003

[63] P. Karvonen, I. D. Moore, T. Sonoda, *et al.*, Nuclear Instruments and Methods in Physics Research Section B: Beam Interactions with Materials and Atoms **266**, 4794 (2008), URL http://www.sciencedirect.com/science/article/pii/S0168583X08009191

[64] A. Nieminen, J. Huikari, A. Jokinen, *et al.*, Hyperfine Interactions **127**, 507 (2000), 10.1023/A:1012694407204, URL http://dx.doi.org/10.1023/A:1012694407204

[65] A. Nieminen, P. Campbell, J. Billowes, *et al.*, Physical Review Letters **88**, 094801 (2002), URL http://link.aps.org/doi/10.1103/PhysRevLett.88.094801

[66] K. Morita, T. Inamura, T. Nomura, *et al.*, Nuclear Instruments and Methods in Physics Research Section B: Beam Interactions with Materials and Atoms **26**, 1-3, 406 (1987), URL http://www.sciencedirect.com/science/article/pii/0168583X87907865

[67] M. Yoshii, H. Hama, K. Taguchi, *et al.*, Nuclear Instruments and Methods in Physics Research Section B: Beam Interactions with Materials and Atoms **26**, 1-3, 410 (1987), URL http://www.sciencedirect.com/science/article/pii/0168583X87907877

[68] A. Wojtasiewicz, G. Canchel, A. Emsallem, *et al.*, Nuclear Physics A **746**, 0, 663 (2004), URL http://www.sciencedirect.com/science/article/pii/S0375947404009972

[69] M. Huyse, K. Deneffe, J. Gentens, *et al.*, Nuclear Instruments and Methods in Physics Research Section B: Beam Interactions with Materials and Atoms **26**, 1-3, 105 (1987), URL http://www.sciencedirect.com/science/article/pii/0168583X87907385

[70] M. Huyse, P. Dendooven, K. Deneffe, Nuclear Instruments and Methods in Physics Research Section B: Beam Interactions with Materials and Atoms

31, 3, 483 (1988), URL http://www.sciencedirect.com/science/article/pii/0168583X88903503

[71] J. Ärje, J. Äystö, H. Hyvönen, *et al.*, Nuclear Instruments and Methods in Physics Research Section A: Accelerators, Spectrometers, Detectors and Associated Equipment **247**, 3, 431 (1986), URL http://www.sciencedirect.com/science/article/pii/0168900286904043

[72] J. Ärje, J. Äystö, P. Taskinen, *et al.*, Nuclear Instruments and Methods in Physics Research Section B: Beam Interactions with Materials and Atoms **26**, 1-3, 384 (1987), URL http://www.sciencedirect.com/science/article/pii/0168583X8790783X

[73] H. Penttilä, Hyperfine Interactions 1–12 (2012), 10.1007/s10751-012-0607-6, URL http://dx.doi.org/10.1007/s10751-012-0607-6

[74] L. S. Brown, G. Gabrielse, Reviews of Modern Physics **58**, 233 (1986), URL http://link.aps.org/doi/10.1103/RevModPhys.58.233

[75] H. Dehmelt, Reviews of Modern Physics **62**, 525 (1990), URL http://link.aps.org/doi/10.1103/RevModPhys.62.525

[76] G. Bollen, R. B. Moore, G. Savard, *et al.*, Journal of Applied Physics **68**, 9, 4355 (1990), URL http://link.aip.org/link/?JAP/68/4355/1

[77] G. Bollen, H.-J. Kluge, M. König, *et al.*, Physical Review C **46**, R2140 (1992), URL http://link.aps.org/doi/10.1103/PhysRevC.46.R2140

[78] M. Block, C. Bachelet, G. Bollen, *et al.*, Physical Review Letters **100**, 132501 (2008), URL http://link.aps.org/doi/10.1103/PhysRevLett.100.132501

[79] H. Schnatz, G. Bollen, P. Dabkiewicz, *et al.*, Nuclear Instruments and Methods in Physics Research Section A: Accelerators, Spectrometers, Detectors and Associated Equipment **251**, 1, 17 (1986), URL http://www.sciencedirect.com/science/article/pii/0168900286911459

[80] G. Bollen, P. Dabkiewicz, P. Egelhof, *et al.*, Hyperfine Interactions **38**, 793 (1987), 10.1007/BF02394875, URL http://dx.doi.org/10.1007/BF02394875

[81] J. Dilling, D. Ackermann, J. Bernard, *et al.*, Hyperfine Interactions **127**, 491 (2000), 10.1023/A:1012638322226, URL http://dx.doi.org/10.1023/A:1012638322226

[82] J. Dilling, P. Bricault, M. Smith, *et al.*, Nuclear Instruments and Methods in Physics Research Section B: Beam Interactions with Materials and Atoms **204**, 0, 492 (2003), URL http://www.sciencedirect.com/science/article/pii/S0168583X02021183

[83] G. Savard, R. Barber, C. Boudreau, *et al.*, Hyperfine Interactions **132**, 221 (2001), 10.1023/A:1011986930931, URL http://dx.doi.org/10.1023/A:1011986930931

[84] S. Schwarz, C. Bachelet, M. Block, *et al.*, Hyperfine Interactions **173**, 113 (2006), 10.1007/s10751-007-9549-9, URL http://dx.doi.org/10.1007/s10751-007-9549-9

[85] V. Kolhinen, S. Kopecky, T. Eronen, *et al.*, Nuclear Instruments and Methods in Physics Research Section A: Accelerators, Spectrometers, Detectors and Associated Equipment **528**, 3, 776 (2004), URL http://www.sciencedirect.com/science/article/pii/S0168900204009854

[86] T. Eronen, V. Kolhinen, V. Elomaa, *et al.*, The European Physical Journal A - Hadrons and Nuclei **48**, 1 (2012), 10.1140/epja/i2012-12046-1, URL http://dx.doi.org/10.1140/epja/i2012-12046-1

[87] Klaus, Blaum, Physics Reports **425**, 1, 1 (2006), URL http://www.sciencedirect.com/science/article/pii/S0370157305004643

[88] T. Eronen, *High Precision Q_{EC} Values Measurements of Superallowed* 0^+ *->*0^+ *Beta Decays With JYFLTRAP*, Ph.D. thesis, University of Jyväskylä (2008)

[89] G. Savard, S. Becker, G. Bollen, *et al.*, Physics Letters A **158**, 5, 247 (1991), URL http://www.sciencedirect.com/science/article/pii/0375960191910082

[90] T. Eronen, V.-V. Elomaa, U. Hager, *et al.*, Nuclear Instruments and Methods in Physics Research Section B: Beam Interactions with Materials and Atoms **266**, 19-20, 4527 (2008), URL http://www.sciencedirect.com/science/article/pii/S0168583X08007696

[91] M. Konig, G. Bollen, H.-J. Kluge, *et al.*, International Journal of Mass Spectrometry and Ion Processes **142**, 2-2, 95 (1995), URL http://www.sciencedirect.com/science/article/pii/016811769504146C

[92] J. Hakala, S. Rahaman, V.-V. Elomaa, *et al.*, Physical Review Letters **101**,

052502 (2008), URL http://link.aps.org/doi/10.1103/PhysRevLett.101.052502

[93] J. C. Hardy, I. S. Towner, Physical Review C **79**, 055502 (2009), URL http://link.aps.org/doi/10.1103/PhysRevC.79.055502

[94] M. Kobayashi, T. Maskawa, Progress of Theoretical Physics **49**, 2, 652 (1973), URL http://ptp.ipap.jp/link?PTP/49/652/

[95] T. Eronen, V. Elomaa, U. Hager, *et al.*, Physical Review Letters **97**, 232501 (2006), URL http://link.aps.org/doi/10.1103/PhysRevLett.97.232501

[96] T. Eronen, V.-V. Elomaa, U. Hager, *et al.*, Physical Review Letters **100**, 132502 (2008), URL http://link.aps.org/doi/10.1103/PhysRevLett.100.132502

[97] K. Perajarvi, T. Eronen, V.-V. Elomaa, *et al.*, Applied Radiation and Isotopes **68**, 3, 450 (2010), URL http://www.sciencedirect.com/science/article/pii/S0969804309007878

[98] H.-J. Kluge, W. Nörtershäuser, Spectrochimica Acta Part B: Atomic Spectroscopy **58**, 6, 1031 (2003), URL http://www.sciencedirect.com/science/article/pii/S0584854703000636

[99] W. H. Wing, G. A. Ruff, W. E. Lamb, *et al.*, Physical Review Letters **36**, 1488 (1976), URL http://link.aps.org/doi/10.1103/PhysRevLett.36.1488

[100] S.L., Kaufman, Optics Communications **17**, 3, 309 (1976), URL http://www.sciencedirect.com/science/article/pii/0030401876902674

[101] K. R. Anton, S. L. Kaufman, W. Klempt, *et al.*, Physical Review Letters **40**, 642 (1978), URL http://link.aps.org/doi/10.1103/PhysRevLett.40.642

[102] R. Neugart, The European Physical Journal A - Hadrons and Nuclei **15**, 35 (2002), 10.1140/epja/i2001-10220-2, URL http://dx.doi.org/10.1140/epja/i2001-10220-2

[103] A. Villari, Nuclear Physics A **693**, 1-2, 465 (2001), URL http://www.sciencedirect.com/science/article/pii/S0375947401011071

[104] E. Mané, J. Behr, J. Billowes, *et al.*, Hyperfine Interactions **199**, 357 (2011), 10.1007/s10751-011-0331-7, URL http://dx.doi.org/10.1007/s10751-011-0331-7

[105] M. Koizumi, T. Inamura, K. Morita, *et al.*, Hyperfine Interactions

74, 181 (1992), 10.1007/BF02398628, URL http://dx.doi.org/10.1007/BF02398628

[106] J. Billowes, P. Campbell, E. Cochrane, *et al.*, Nuclear Instruments and Methods in Physics Research Section B: Beam Interactions with Materials and Atoms **126**, 1-4, 416 (1997), international Conference on Electromagnetic Isotope Separators and Techniques Related to Their Applications, URL http://www.sciencedirect.com/science/article/pii/S0168583X97011580

[107] J. L. Cooke, J. Billowes, P. Campbell, *et al.*, Journal of Physics G: Nuclear and Particle Physics **23**, 11, L97 (1997), URL http://stacks.iop.org/0954-3899/23/i=11/a=002

[108] J. M. G. Levins, D. M. Benton, J. Billowes, *et al.*, Physical Review Letters **82**, 2476 (1999), URL http://link.aps.org/doi/10.1103/PhysRevLett.82.2476

[109] P. Campbell, D. M. Benton, J. Billowes, *et al.*, AIP Conference Proceedings **455**, 1, 72 (1998), URL http://link.aip.org/link/?APC/455/72/1

[110] P. Campbell, A. Nieminen, J. Billowes, *et al.*, The European Physical Journal A - Hadrons and Nuclei **15**, 45 (2002), 10.1140/epja/i2001-10223-y, URL http://dx.doi.org/10.1140/epja/i2001-10223-y

[111] P. Campbell, H. L. Thayer, J. Billowes, *et al.*, Physical Review Letters **89**, 082501 (2002), URL http://link.aps.org/doi/10.1103/PhysRevLett.89.082501

[112] B. Cheal, M. Gardner, M. Avgoulea, *et al.*, Physics Letters B **645**, 2-3, 133 (2007), URL http://www.sciencedirect.com/science/article/pii/S037026930601608X

[113] F. Charlwood, K. Baczynska, J. Billowes, *et al.*, Physics Letters B **674**, 1, 23 (2009), URL http://www.sciencedirect.com/science/article/pii/S0370269309002470

[114] B. Cheal, K. Baczynska, J. Billowes, *et al.*, Physical Review Letters **102**, 222501 (2009), URL http://link.aps.org/doi/10.1103/PhysRevLett.102.222501

[115] K. Baczynska, J. Billowes, P. Campbell, *et al.*, Journal of Physics G: Nuclear and Particle Physics **37**, 10, 105103 (2010), URL http://stacks.iop.org/0954-3899/37/i=10/a=105103

[116] F. Charlwood, J. Billowes, P. Campbell, *et al.*, Physics Letters B **690**, 4, 346 (2010), URL http://www.sciencedirect.com/science/article/pii/S0370269310006520

[117] F. Charlwood, K. Baczynska, J. Billowes, *et al.*, Hyperfine Interactions **196**, 143 (2010), 10.1007/s10751-009-0153-z, URL http://dx.doi.org/10.1007/s10751-009-0153-z

[118] B. Cheal, K. Baczynska, J. Billowes, *et al.*, Hyperfine Interactions **181**, 107 (2008), 10.1007/s10751-008-9629-5, URL http://dx.doi.org/10.1007/s10751-008-9629-5

[119] Y. Kudryavtsev, T. E. Cocolios, J. Gentens, *et al.*, Nuclear Instruments and Methods in Physics Research Section B: Beam Interactions with Materials and Atoms **267**, 17, 2908 (2009), URL http://www.sciencedirect.com/science/article/pii/S0168583X09006788

[120] I. D. Moore, A. Nieminen, J. Billowes, *et al.*, Journal of Physics G: Nuclear and Particle Physics **31**, 10, S1499 (2005), URL http://stacks.iop.org/0954-3899/31/i=10/a=020

[121] T. Kessler, T. Eronen, C. Mattolat, *et al.*, Hyperfine Interactions **171**, 121 (2006), 10.1007/s10751-006-9496-x, URL http://dx.doi.org/10.1007/s10751-006-9496-x

[122] I. D. Moore, T. Kessler, J. Äystö, *et al.*, Hyperfine Interactions **171**, 135 (2006), 10.1007/s10751-006-9494-z, URL http://dx.doi.org/10.1007/s10751-006-9494-z

[123] T. Kessler, I. D. Moore, Y. Kudryavtsev, *et al.*, Nuclear Instruments and Methods in Physics Research Section B: Beam Interactions with Materials and Atoms **266**, 4, 681 (2008), URL http://www.sciencedirect.com/science/article/pii/S0168583X07018290

[124] I. D. Moore, T. Kessler, T. Sonoda, *et al.*, Nuclear Instruments and Methods in Physics Research Section B: Beam Interactions with Materials and Atoms **268**, 6, 657 (2010), URL http://www.sciencedirect.com/science/article/pii/S0168583X09013159

[125] T. E. Cocolios, A. N. Andreyev, B. Bastin, *et al.*, Physical Review Letters **103**, 102501 (2009), URL http://link.aps.org/doi/10.1103/PhysRevLett.103.102501

[126] S. Raeder, V. Sonnenschein, T. Gottwald, *et al.*, Journal of Physics B: Atomic, Molecular and Optical Physics **44**, 16, 165005 (2011), URL http://stacks.iop.org/0953-4075/44/i=16/a=165005

[127] V. Sonnenschein, S. Raeder, A. Hakimi, *et al.*, Journal of Physics B: Atomic, Molecular and Optical Physics **45**, 16, 165005 (2012), URL http://stacks.iop.org/0953-4075/45/i=16/a=165005

[128] M. Reponen, I. D. Moore., T. Kessler, *et al.*, The European Physical Journal A - Hadrons and Nuclei **48**, 1 (2012), 10.1140/epja/i2012-12045-2, URL http://dx.doi.org/10.1140/epja/i2012-12045-2

[129] C. Rauth, C. Geppert, R. Horn, *et al.*, Nuclear Instruments and Methods in Physics Research Section B: Beam Interactions with Materials and Atoms **215**, 1-2, 268 (2004), URL http://www.sciencedirect.com/science/article/pii/S0168583X03019384

[130] R. Horn, *Aufbau eines Systems gepulster, abstimmbarer Festörpelaser zum Einzats in der Resonanzionisations-Massenspektrometrie*, Ph.D. thesis, Johannes Gutenberg University Mainz (2003)

[131] J. Lassen, P. Bricault, M. Dombsky, *et al.*, AIP Conference Proceedings **1099**, 1, 769 (2009), URL http://link.aip.org/link/?APC/1099/769/1

[132] H. Penttila, T. Eronen, J. Hakala, *et al.*, vol. 59, 1589 (J. Korean Phys.Soc, 2011), proceedings of International Conference on Nuclear Data Science and Technology 2010, ND2010, URL http://www.kps.or.kr/jkps/abstract_view.asp?articleuid=E08874DC-EBEA-4346-A564-FCDD7A024EA7

[133] T. Kessler, *Development and application of laser technologies at radioactive ion beam facilities*, Ph.D. thesis, University of Jyväskylä (2008)

[134] M. Reponen, T. Kessler, I. D. Moore, *et al.*, The European Physical Journal A - Hadrons and Nuclei **42**, 509 (2009), 10.1140/epja/i2009-10830-6, URL http://dx.doi.org/10.1140/epja/i2009-10830-6

[135] D. Stresau, K. L. Hunter, *Extending the limits for linear ion counting*, http://www.sge.com/root/pdfs_local/technical_articles/TA-0109-A.pdf, look-up date: 21.01.2011, SGE company website

[136] W. Berthold, A. Wucher, Physical Review B **56**, 4251 (1997), URL http://link.aps.org/doi/10.1103/PhysRevB.56.4251

[137] J. Meyer, R. Reininger, Physical Review A **47**, R3491 (1993), URL http://link.aps.org/doi/10.1103/PhysRevA.47.R3491

[138] G. Uhlenberg, J. Dirscherl, H. Walther, Physical Review A **62**, 063404 (2000), URL http://link.aps.org/doi/10.1103/PhysRevA.62.063404

[139] I. ?D. Moore, Nuclear Instruments and Methods in Physics Research Section B: Beam Interactions with Materials and Atoms **266**, 19-20, 4434 (2008), URL http://www.sciencedirect.com/science/article/pii/S0168583X08007520

[140] J. Routti, S. Prussin, Nuclear Instruments and Methods **72**, 2, 125 (1969), URL http://www.sciencedirect.com/science/article/pii/0029554X69901487

[141] M. Ranjan, *Design and Characterization of a Cryogenic Stopping Cell for Radioactive Ions*, Ph.D. thesis, University of Groningen (2012)

[142] Wolfram Research, Inc., Mathematica, Version 8.0, Champaign, IL (2011).

[143] J. Humlicek, Journal of Quantitative Spectroscopy and Radiative Transfer **27**, 4, 437 (1982), URL http://www.sciencedirect.com/science/article/pii/0022407382900784

[144] B. Armstrong, Journal of Quantitative Spectroscopy and Radiative Transfer **7**, 1, 61 (1967), URL http://www.sciencedirect.com/science/article/pii/002240736790057X

[145] A. McLean, C. Mitchell, D. Swanston, Journal of Electron Spectroscopy and Related Phenomena **69**, 2, 125 (1994), URL http://www.sciencedirect.com/science/article/pii/0368204894021897

[146] E. Otten, in D. Bromley, ed., *treatise on Heavy-Ion Science*, vol. 8, 517–638 (Plenum, New York, 1989)

[147] D. Brink, G. Satchler, *Angular momentum* (Oxford Scientific Publications, 2002)

[148] A. Steudel, U. Triebe, D. Wendlandt, Zeitschrift für Physik A Hadrons and Nuclei **296**, 189 (1980), 10.1007/BF01415832, URL http://dx.doi.org/10.1007/BF01415832

[149] W. King, *Isotope shifts in atomic spectra* (Plenum, New York, 1984)

[150] D. York, N. M. Evensen, M. L. Martínez, *et al.*, American Journal of Physics **72**, 3, 367 (2004), URL http://link.aip.org/link/?AJP/72/367/1

[151] K. Blaum, C. Geppert, H.-J. Kluge, *et al.*, Nuclear Instruments and Methods in Physics Research Section B: Beam Interactions with Materials and Atoms **204**, 0, 331 (2003), 14th International Conference on Electromagnetic Isotope Separators and Techniques Related to their Applications, URL http://www.sciencedirect.com/science/article/pii/S0168583X02019420

[152] I. D. Moore, J. Billowes, P. Campbell, *et al.*, AIP Conference Proceedings **831**, 1, 511 (2006), URL http://link.aip.org/link/?APC/831/511/1

[153] P. Karvonen, T. Sonoda, I. D. Moore, *et al.*, The European Physical Journal - Special Topics **150**, 283 (2007), 10.1140/epjst/e2007-00325-2, URL http://dx.doi.org/10.1140/epjst/e2007-00325-2

[154] T. Sonoda, T. E. Cocolios, J. Gentens, *et al.*, Nuclear Instruments and Methods in Physics Research Section B: Beam Interactions with Materials and Atoms **267**, 17, 2918 (2009), URL http://www.sciencedirect.com/science/article/pii/S0168583X09007812

[155] J. D. Craggs, J. M. Meek, Proceedings of the Royal Society of London. Series A. Mathematical and Physical Sciences **186**, 1005, 241 (1946), http://rspa.royalsocietypublishing.org/content/186/1005/241.full.pdf+html, URL http://rspa.royalsocietypublishing.org/content/186/1005/241.abstract

[156] I. Pohjalainen, *Experimental gas jet studies for the IGISOL LIST method and simulation modeling*, Master's thesis, University of Jyväskylä (2010)

[157] J. Arthur L. Schmeltekopf, H. P. Broida, The Journal of Chemical Physics **39**, 5, 1261 (1963), URL http://link.aip.org/link/?JCP/39/1261/1

[158] G. Tejeda, B. Maté, J. M. Fernández-Sánchez, *et al.*, Physical Review Letters **76**, 34 (1996), URL http://link.aps.org/doi/10.1103/PhysRevLett.76.34

[159] M. Reponen, I. D. Moore, I. Pohjalainen, *et al.*, Nuclear Instruments and Methods in Physics Research Section A: Accelerators, Spectrometers, Detectors and Associated Equipment **635**, 1, 24 (2011), URL http://www.sciencedirect.com/science/article/pii/S0168900211002117

[160] P. Karvonen, *Fission yield studies with SPIG-equipped IGISOL: A*

novel method for nuclear data measurements, Ph.D. thesis, University of Jyväskylä (2010)

[161] H. D. Varentsov, V.L., Nuclear Instruments and Methods in Physics Research Section A: Accelerators, Spectrometers, Detectors and Associated Equipment **317**, 1-2, 1 (1992), cited By (since 1996) 7, URL http://www.scopus.com/inward/record.url?eid=2-s2.0-0002261824&partnerID=40&md5=696c094e933e923dfb4050fd72c14bf7

[162] V. Varentsov, A. Ignatiev, Nuclear Instruments and Methods in Physics Research Section A: Accelerators, Spectrometers, Detectors and Associated Equipment **413**, 2-3, 447 (1998), URL http://www.sciencedirect.com/science/article/pii/S0168900298003544

[163] R. O'leary, J. Beck, http://www.pwrengineering.com/articles/nozzledesign.htm

[164] D. B. Atkinson, M. A. Smith, Review of Scientific Instruments **66**, 9, 4434 (1995), URL http://link.aip.org/link/?RSI/66/4434/1

[165] V. A. Soukhanovskii, H. W. Kugel, R. Kaita, *et al.*, Review of Scientific Instruments **75**, 10, 4320 (2004), URL http://link.aip.org/link/?RSI/75/4320/1

[166] G. Dupeyrat, J. B. Marquette, B. R. Rowe, Physics of Fluids **28**, 5, 1273 (1985), URL http://link.aip.org/link/?PFL/28/1273/1

[167] I. R. Sims, J.-L. Queffelec, A. Defrance, *et al.*, The Journal of Chemical Physics **100**, 6, 4229 (1994), URL http://link.aip.org/link/?JCP/100/4229/1

[168] I. Mukha, L. Batist, E. Roeckl, *et al.*, Physical Review C **70**, 044311 (2004), URL http://link.aps.org/doi/10.1103/PhysRevC.70.044311

[169] I. Mukha, E. Roeckl, L. Batist, *et al.*, Nature **439**, 298 (2006), URL http://www.nature.com/nature/journal/v439/n7074/full/nature04453.html

[170] C. Plettner, H. Grawe, I. Mukha, *et al.*, Nuclear Physics A **733**, 1-2, 20 (2004), URL http://www.sciencedirect.com/science/article/pii/S0375947403019778

[171] I. Mukha, E. Roeckl, J. Döring, *et al.*, Physical Review Letters **95**, 022501 (2005), URL http://link.aps.org/doi/10.1103/PhysRevLett.95.022501

[172] V. Goldansky, Nuclear Physics **19**, 0, 482 (1960), URL http://www.sciencedirect.com/science/article/pii/0029558260902583

[173] D. F. Geesaman, R. L. McGrath, P. M. S. Lesser, *et al.*, Physical Review C **15**, 1835 (1977), URL http://link.aps.org/doi/10.1103/PhysRevC.15.1835

[174] R. A. Kryger, A. Azhari, M. Hellström, *et al.*, Physical Review Letters **74**, 860 (1995), URL http://link.aps.org/doi/10.1103/PhysRevLett.74.860

[175] I. Mukha, K. Sümmerer, L. Acosta, *et al.*, Physical Review Letters **99**, 182501 (2007), URL http://link.aps.org/doi/10.1103/PhysRevLett.99.182501

[176] I. Mukha, L. Grigorenko, K. Sümmerer, *et al.*, Physical Review C **77**, 061303 (2008), URL http://link.aps.org/doi/10.1103/PhysRevC.77.061303

[177] J. Giovinazzo, B. Blank, M. Chartier, *et al.*, Physical Review Letters **89**, 102501 (2002), URL http://link.aps.org/doi/10.1103/PhysRevLett.89.102501

[178] M. Pfützner, E. Badura, C. Bingham, *et al.*, The European Physical Journal A - Hadrons and Nuclei **14**, 279 (2002), 10.1140/epja/i2002-10033-9, URL http://dx.doi.org/10.1140/epja/i2002-10033-9

[179] B. Blank, A. Bey, G. Canchel, *et al.*, Physical Review Letters **94**, 232501 (2005), URL http://link.aps.org/doi/10.1103/PhysRevLett.94.232501

[180] B. Blank, M. Płoszajczak, Reports on Progress in Physics **71**, 4, 046301 (2008), URL http://stacks.iop.org/0034-4885/71/i=4/a=046301

[181] O. L. Pechenaya, C. J. Chiara, D. G. Sarantites, *et al.*, Physical Review C **76**, 011304 (2007), URL http://link.aps.org/doi/10.1103/PhysRevC.76.011304

[182] A. Kankainen, V.-V. Elomaa, L. Batist, *et al.*, Physical Review Letters **101**, 142503 (2008), URL http://link.aps.org/doi/10.1103/PhysRevLett.101.142503

[183] J. Cerny, D. M. Moltz, D. W. Lee, *et al.*, Physical Review Letters **103**, 152502 (2009), URL http://link.aps.org/doi/10.1103/PhysRevLett.103.152502

[184] K. Kaneko, Y. Sun, M. Hasegawa, *et al.*, Physical Review C **77**, 064304 (2008), URL http://link.aps.org/doi/10.1103/PhysRevC.77.064304

[185] I. Mukha, H. Grawe, E. Roeckl, *et al.*, Physical Review C **78**, 039803 (2008), URL http://link.aps.org/doi/10.1103/PhysRevC.78.039803

[186] O. L. Pechenaya, D. G. Sarantites, W. Reviol, *et al.*, Physical Review C

78, 039804 (2008), URL http://link.aps.org/doi/10.1103/PhysRevC.78.039804

[187] D. G. Jenkins, Physical Review C **80**, 054303 (2009), URL http://link.aps.org/doi/10.1103/PhysRevC.80.054303

[188] T. Badr, M. D. Plimmer, P. Juncar, *et al.*, Physical Review A **74**, 062509 (2006), URL http://link.aps.org/doi/10.1103/PhysRevA.74.062509

[189] G. Wessel, H. Lew, Physical Review **92**, 641 (1953), URL http://link.aps.org/doi/10.1103/PhysRev.92.641

[190] H. Dahmen, S. Penselin, Zeitschrift für Physik A Hadrons and Nuclei **200**, 456 (1967), 10.1007/BF01326186, URL http://dx.doi.org/10.1007/BF01326186

[191] J. Carlsson, P. Jönsson, L. Sturesson, Zeitschrift für Physik D Atoms, Molecules and Clusters **16**, 87 (1990), 10.1007/BF01679568, URL http://dx.doi.org/10.1007/BF01679568

[192] B. Marsh, *In-Source Laser Resonance Ionization at ISOL Facilities*, Ph.D. thesis, University of Manchester (2006)

[193] C. Geppert, Nuclear Instruments and Methods in Physics Research Section B: Beam Interactions with Materials and Atoms **266**, 19-20, 4354 (2008), URL http://www.sciencedirect.com/science/article/pii/S0168583X08007350

[194] T. Kessler, I. Moore, H. Penttilä, *et al.*, Nuclear Instruments and Methods in Physics Research Section B: Beam Interactions with Materials and Atoms **266**, 19-20, 4420 (2008), URL http://www.sciencedirect.com/science/article/pii/S0168583X08007490

[195] R. Kirchner, Nuclear Instruments and Methods in Physics Research Section B: Beam Interactions with Materials and Atoms **70**, 1-4, 186 (1992), URL http://www.sciencedirect.com/science/article/pii/0168583X9295930P

[196] R. Kirchner, E. Roeckl, Nuclear Instruments and Methods **127**, 2, 307 (1975), URL http://www.sciencedirect.com/science/article/pii/0029554X75905042

[197] SRIM, James F. Ziegler, Ziegler@SRIM.org

[198] S. Rothe, *Rilis database*, http://riliselements.web.cern.ch/riliselements/index.php (2010), look-up date: 21.01.2011

[199] S. Rothe, *et al.*, *First ionization potential of astatine measured by laser spectroscopy*, in preparation (2012)

[200] J. Roßnagel, S. Raeder, A. Hakimi, *et al.*, Physical Review A **85**, 012525 (2012), URL http://link.aps.org/doi/10.1103/PhysRevA.85.012525